ABSTRACT

Title of Dissertation: PARAMETRIC DESIGN AND EXPERIMENTAL VALIDATION OF CONJUGATE STRESS SENSORS FOR STRUCTURAL HEALTH MONITORING

Jonathan Kordell

Dissertation directed by: Prof. Abhijit Dasgupta

Prof. Miao Yu

Department of Mechanical Engineering

In this dissertation, conjugate stress (CS) sensing is advanced through a parametric evaluation of a surface-mounted design and through experimental validation in monotonic and cyclic tensile tests. The CS sensing concept uses a pair of sensors of significantly different mechanical stiffness for direct query of the instantaneous local stress-strain relationship in the host structure, thus offering measurement of important health indicators such as stiffness (modulus), yield strength, strain hardening, and cyclic hysteresis. In this study, surface-mounted CS sensor designs are parametrically evaluated with finite element modeling, with respect to the sensors' location, thickness, and modulus and the external loading state. An analytic pin-force model is developed to infer the host structure's stress-strain state, based on the strain outputs of the CS sensor-pair. Two CS sensor designs are fabricated – one employs resistive foil strain gauges and the second employs fiber optic sensors – and paired with the pin-force model for experimental demonstration of the measurement of: (i) stress-strain history of three different isotropic metal bars (aluminum, copper, and steel) as they experience monotonic tensile loads well into plasticity

and (ii) stress-strain hysteresis of a steel bar as it is subject to cyclic tensile fatigue. In the cyclic tests, two machine learning algorithms – anomaly detection and neural net classification – are used in conjunction with the estimated host stiffness from the CS sensor and pin force model to predict the onset of damage in the steel beams.

PARAMETRIC DESIGN AND EXPERIMENTAL VALIDATION OF CONJUGATE STRESS SENSORS FOR STRUCTURAL HEALTH MONITORING

by

Jonathan Kordell

Dissertation submitted to the Faculty of the Graduate School of the
University of Maryland, College Park, in partial fulfillment
of the requirements for the degree of
Doctor of Philosophy
2021

Advisory Committee:
Prof. Abhijit Dasgupta, Co-Chair
Prof. Miao Yu, Co-Chair
Prof. Amr Baz
Prof. Hugh Bruck
Prof. Inderjit Chopra, Dean's Representative
Prof. Bongtae Han

Table of Contents

1. Introduction

Reliability is the ability of a product to properly function within specified performance limits for a specified period of time under specified life cycle application conditions. Providing a continuous measure of a structure's reliability throughout its life is the goal of structural health monitoring (SHM). And while a structure's reliability is primarily a function of its initial design and expected life-cycle usage profile; abnormal usage, environmental effects, and other accidental abuse events make continuous monitoring attractive to assure safe and reliable operation. Moreover, real-time, in-situ health monitoring can increase consumer confidence, improve logistics, and decrease costs associated with scheduled maintenance plans.

Monitoring a structure's state of health requires continuous acquisition of appropriate sensor data, signal processing and transmitting techniques, and insightful data analytics. All three fields are the focus of ongoing research by industry and academia. Sensors are constantly being fabricated or redesigned for improved miniaturization, cost, ease-of-integration, power draw, accuracy, mobility, and reliability. MEMs, piezoelectrics, fiber optics, and virtual sensors are all sensor types being explored. Signal processing and transmitting improvements seek to reduce noise and advance the safety of sending large amounts of sensitive data from the sensor location to a processing location. Data analytics in the form of physics of failure, machine learning, or a hybrid approach are constantly being updated to produce better remaining useful life estimates. Even digital twins are becoming prevalent in industry, taking the sensor data and producing real time models to predict continued product performance.

This study focuses on improvement in the sensor category. Specifically, conjugate stress (CS) sensing is investigated because it is not only sensitive to macroscale damages, like cracks, but also sensitive to microstructural damages by tracking damage precursors. CS sensing uses the strains measured from two collocated extensometers of drastically different stiffness to measure the instantaneous stress-strain state in the host, enabling the monitoring of damage precursors like stiffness degradation [1]. Damage precursors are changes in microstructure that result in a corresponding trackable macroscale property change. In industries with strict performance requirements, such as military applications, zero damage or "fatigue-free" platforms are becoming increasingly sought after. Such a system must notify the user of incipient damage before visible failure mechanisms, like cracks, occur by tracking damage precursors. Material stiffness is a good candidate for a damage precursor in plastic deformation, fatigue, and corrosive damage mechanisms. In this study, a CS sensor is fabricated to measure stiffness changes, identifying damage before visible indicators are present.

1.1. Problem Statement

Civil structures, transportation vehicles, and consumer devices can all show degraded performance due to fatigue or corrosion. Real time prognostics of such structures can save costs, increase consumer confidence, and improve safety. In more critical missions, real time feedback can let the user quickly correct for small damages that may have bigger impacts later in the product's life. Therefore, a damage detection system capable of real time, in-situ measurement of such structures and able to provide feedback of damage before visible damage occurs is of great interest.

In the failure mechanisms of concern, i.e. plastic deformations, fatigue, and corrosion, stiffness degradation is a known precursor to macroscale damage, like cracking. In past studies [1] [2] [3], an embedded CS sensor has been developed to track instantaneous host stiffness and strain energy density. The past studies produced analytic and numeric models to support the embedded conjugate stress sensor design and asses its sensitivity to changes in host stiffness. The sensor design was modified to surface-mounted configuration for experimental validation [1]. The surface-mounted CS sensor was verified with simple elastic modulus measurement of three materials (acrylic, FR4, and aluminum) as well as nondimensionalized stiffness measurement of aluminum in a monotonic quasistatic tensile test. Although the conjugate stress sensor has demonstrated potential for SHM, its experimental applications have been limited. In contrast, there have been several parametric design studies, generating more questions with each analysis about the CS sensor architecture.

In this study, we aim to numerically address some of the design questions left unanswered by the previous studies about CS sensor architecture. Then, we aim to push the experimental applications of the conjugate stress sensor from pristine elastic modulus measurement to continuous measurement of a deteriorating modulus due to plasticity, fatigue, and corrosion. A new fiber-optic version of the CS sensor is developed in this study, as a replacement to the resistive copper foil CS sensor elements used previously. Fiber optics were chosen to help future work bring the conjugate stress sensor off the lab

bench and into industry as they offer many benefits, including electromagnetic immunity, resistance to corrosion, far field sensing, and a more compatible embedded geometry.

In detail, this study will: (1) provide a parametric evaluation of the design of surface-mounted CS sensors under different external load states by quantifying its sensitivity with respect to its individual sensors' location, thickness, and modulus; (2) fabricate CS sensors with fiber optic and resistive copper foil sensing elements to measure the full stress-strain history of three metals – aluminum, copper, and steel – as they experience a continuously decreasing tangent modulus under elastic-plastic loading; and (3) use the fabricated CS sensors to monitor progressive modulus degradation due to cyclic tensile fatigue. The above tasks are enabled by models that capture the mechanics of the CS sensor concept. Three modeling methods are explored – a simple analytic pin force model, a more general (but simplified) variational model, and a fully detailed finite element model. As the finite element model proved most accurate, it was chosen for performing the parametric design analysis in Task (1) above. The pin-force model was chosen for the experimental analyses in Tasks (2) and (3) since it is the least computationally expensive of the three. In this way, the study is bookended, providing the most accurate parametric design finite element analysis while demonstrating that the CS sensor still has good accuracy with the real-time use of the rapid analytic model. Future work is aimed at improving the variational model, as it may provide an optimal compromise between accuracy and computational expense.

1.2. Literature Review

Sensor technology for SHM is an increasingly large field of study. Inspection techniques are quite common in industry, including nondestructive inspection techniques like acoustic emission, ultrasonic, thermal or infrared imaging, magnetic flux, electromagnetic, etc. However, these techniques require the structure to be removed from service or for technicians to be sent out to the structure to perform the inspection. To remove these costs, the current thrust of industry and academia is for real-time inspection of structures using in-situ sensors.

Many types of sensors have been employed for real-time, in-situ inspection. Canary sensors, named after the canaries placed in mines to warn of bad air, have been proposed [4] [5] [6]. Resistive gauges have been used to monitor neutral axis shifts in brides and woven metal fabrics [7] [8]; however they can show reduced sensitivity compared to the other sensing methods discussed later and the electrical loss along the wires makes resistive sensors ineffective for far field applications [2] [9]. Piezoelectric sensors are an encouraging option for sensing as they can also be used as active inputs and control devices. Active piezoelectric sensors have been used to detect cracks in metal and composite sheets, as well as impact events and the resulting damage accumulation [10] [11] [12] [13] [14] [15] [16]. Passively recording acoustic emissions, piezoelectric sensors have been used extensively to estimate the current state of health of the structure [17] [18] [19] [20] [21]. Though piezoelectric sensors have many benefits for SHM, they have some drawbacks as well. For example, piezoelectric sensors display significant drift

under static loads and thus are not suitable for static and quasistatic loading environments [22]. Also, they are sensitive to harsh environmental factors such as temperature fluctuations, electromagnetic interference, and chemical presence making stable measurement difficult [23]. Magnetostrictive sensors behave similarly to piezoelectric sensors and have been used in ultrasonic scanning and open voltage scanning [24] [25]. However, they have similar drawbacks to piezoelectric sensors.

Fiber optic sensors are an attractive sensing option due to some of the unique benefits they offer, including light weight, low power consumption, high accuracy, embeddable geometry, resistance to harsh chemical environment, electromagnetic immunity, multiplexing capabilities, and low loss of signal for far field applications. There are several choices of sensing mechanism when using optical fibers and coupled with the variety in structural design of the sensor, fiber optic sensors comprise a diverse field [23]. Three notable fiber optic sensors for SHM are distributed sensors [26] [27] [28] [29] [30], Fabry-Perot interferometers (FPIs), and fiber Bragg gratings (FBGs). Some detailed discussion will be made of FPIs and FBGs as they are employed in this study.

Fabry-Perot interferometers are typically made of two reflecting, parallel partial mirrors. Conventionally, coherent light input to the system reflects off the first partial mirror and then the second partial beam creating multi-beam interference. The reflected light intensity is a function of phase, which can then be used as a measure of displacement between the two mirrors. Conversely, low coherence light can be input to the system. When the optical path length between the two mirrors is similar to the coherence length

of the light, two beam interference occurs. From two beam interference, the exact optical path length can be determined from the wavelengths of light corresponding to peaks in the reflected intensity spectrum. Fabry-Perot interferometers of similar optical path lengths can be integrated in series to decrease sensitivity to wavelength fluctuation. Because tracking peaks in an intensity spectrum is time consuming, this technique is primarily used for quasi-static or static measurements. For dynamic measurement, a low coherence Fabry-Perot interferometer can be placed in series with a high finesse Fabry-Perot interferometer to isolate certain wavelengths of light. When the isolated wavelengths correspond to quadrature points in the two-beam interference spectrum, the intensity can be approximated as a linear function of phase and thus optical path length. This Fabry-Perot interferometer setup is particularly suited for dynamic measurements because the only recorded value is intensity; however, the measurement range is limited to the quadrature region of the spectrum. Therefore, only small displacements can be measured with high confidence. A wide range of structural designs for optical fiber Fabry-Perot interferometers have been reported in literature [31] [32] [33]. Optical fiber Fabry-Perot interferometers have been implemented in composites to measure residual stresses during the curing process [34]. They have also been implemented in composites to measure damage after impact events and acoustic emissions during fatigue [35] [36] [37].

Fiber Bragg grating sensors use a periodic change of the reflective index within an optical fiber to reflect a narrow bandwidth of light called the Bragg wavelength. When stressed, the periodicity inside the optical fiber changes causing a shift in the Bragg wavelength.

Therefore, by tracking the Bragg wavelength, the strain of the structure can be measured. FBGs have been used extensively for strain monitoring in a range of applications. Crack detection in stainless steel has been achieved using a hybrid PZT-FBG ultrasonic sensor [11]. Impact localization in composite laminates using multiple embedded FBGs has been performed [38]. FBGs have been used for ultrasonic damage detection in carbon fiber reinforced polymers [39]. In fatigue loading, embedded FBGs have been used to track strain and temperature variations before fracture occurs [40] [41] [42].

Although the current applications of real-time sensing is extensive, most are limited to detecting macroscale damage. The benefit of SHM is to reduce the risks and costs associated with late-life cycle maintenance and repairs, i.e. to improve logistic planning. In Figure 1-1, the farther left the damage detection limit is located, the greater logistic benefits one realizes. Therefore, the current PHM techniques which rely on capturing macroscale damage, like crack formation and crack growth, provide only a small repair window for maintenance unsuited for high reliability applications. For example, in metals under fatigue, visually noticeable cracks may only form when over 75% of life has already been consumed [43]. Therefore, sensing technology should shift focus to capturing microscale damage. When microscale damage is accurately tracked, repair logistics can be better organized to save costs, safer “fatigue-free” structures can be realized, and real-time feedback in resilient structures can allow the system to adjust performance and therefore extend its lifetime. These benefits are all tied to shifting the detection limit in Figure 1-1 to the left; instead of measuring macroscale damage, we aim to measure microscale damage.

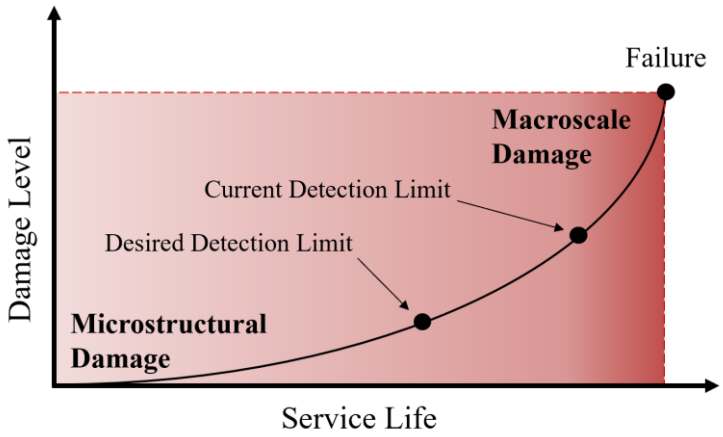

Figure 1-1.By shifting the damage detection limit into the microscale regime, PHM benefits are greatly increased.

Tracking the exact microscale damage in real-time and in-situ is impractical. As a work around, we track damage precursors. A damage precursor is defined as any observable degradation of the material microstructural morphology and resulting change in the physical properties of a structure prior to any detectable macroscale damage [44]. For example, cold rolled AISI 1095 steel experiencing a sinusoidal loading of no more than 600ue showed substantial grain reorientation after only 75k cycles, which corresponded to a 25% drop in elastic modulus [45]. Accordingly, the degradation of elastic modulus can be considered a damage precursor to fatigue. Dislocation motion, slip band formation, and reorientation of grains are more examples of microstructural evolutions that influence the macroscale properties [46] [47] [45].

Damage precursors can be tracked with a variety of methods including microscopy, digital image correlation (DIC) [48], ultrasound [12] [43] [49], and nonlinear vibration [44] [50] each showcasing their own unique advantages. However, these techniques often require large data acquisition systems or active inputs to detect damage, which can be challenging to implement in-situ and in real time. Also, it must be noted that structural

damage is not the only cause of characteristic variations – environmental and operational changes may vary such that they completely mask structural damage [51]. To accommodate these concerns, we chose to pursue a lightweight, small size, passive sensor which can decouple environmental and operational changes from changes in a material's stiffness, a known damage precursor.

We chose to monitor the stiffness of materials because it is known to degrade with damage accumulation, either due to plastic deformations, fatigue, or corrosion. When metals experience plasticity, the instantaneous modulus is known to drop severely. Further, even the elastic modulus can change after plastic deformations. For example, when true strain exceeded 0.1 in DC05 and HSLA steel, a drop in elastic modulus greater than 20% was observed. The decrease in modulus versus plastic strains was most severe at early plastic deformations and tapered off as the plastic deformations became more severe, indicating good sensitivity to small scale damage, but maybe poor long term monitoring performance [52].

In a fatiguing specimen, stiffness degradation has direct correspondence to damage progression under repetitive loading [12] [53] [54]. Cold rolled AISI 1095 steel showed a 25% reduction in modulus after 75k harmonic cycles of excitation within the elastic limit of the material. The reduction in modulus then increased to more than 50% after 225k cycles due to grain fragmentation and realignment [45]. Similarly in composites, stiffness is known to degrade as damage is accumulated due to microcracking or delamination of the plies.

In corrosive environments, elastic modulus has proven to degrade with corrosion time. In one study, dog bones were cut from a seawater exposed steel box girder and mechanically tested in monotonic uniaxial tensile tests. It was found that the modulus of the steel decreased with increased corrosion, albeit with a weak linear correlation [55]. After severe corrosion, however, the reduction in modulus was measured to be greater than 50% [56]. The reduction in modulus can be attributed mainly to pitting on the surface. Just as microcracking in composites results in overall stiffness degradation, it is proposed that pitting has a similar effect. Pitting leads to local plastic zones in the structure, which should be captured by a stiffness sensor [57] [29]. In aluminum 7050, the elastic modulus dropped by more than 10% when the material was exposed to a corrosive environment according to specification ASTM G34-01 for 6 hours and again showed a linear regression with exposure time [58].

As further evidence of stiffness being a known damage indicator, many models are available that project the loss in life as a function of reduced stiffness [59] [60] [61]. In [62], stiffness reduction was shown to have a linear relationship with crack area, leading to a constant energy release rate. Similarly, the shear lag model for composites damaged by transverse matrix cracking under monotonic loading has been studied by numerous investigators [63]. Statistical models of stiffness degradation are also available [64]. However, these may be unsuited for categorizing damage precursors as they rely on macroscale damage.

Many sensors are available to measure stiffness. One such sensor can measure stiffness degradation in composites with a nominal stiffness of 35 GPa using a piezospectroscopic coating and traditional DIC techniques. However, the error with the measurement system was almost 10 GPa so it was only suitable for critical damage detection [48]. In another study, a unique smart material was developed to aid in tracking its own stiffness. Mechanochromic fibers were woven into a composite such that as the composite was stressed the material changed color. With a strain sensor attached to the material and an optical device to record color, the current stress-strain, and thus stiffness, state of the host material could be determined [65]. In another study, a sensor probe was developed to track muscle stiffness. The probe included an oscillating arm that, when in contact with a soft material, changed its resonant frequency. By measuring the frequency shift, the modulus of the soft material can be determined [66]. Another sensor for measuring stiffness equated changes in the neutral axis of the structure to a local loss of stiffness [7]. Though these sensors have benefits, they also have limitations such as necessary DIC, reduced material properties, active input, and further study to reveal stiffness from the neutral axis damage index, respectively.

The next stiff sensor reported in literature is the dual-stiffness sensor. A dual stiffness sensor uses a pair of passive sensors with different resistances to deflection to independently measure strain in the host under a loading event. Then the strain measured by the sensor with higher resistance provides a pseudo stress value and the sensor with lower resistance a pseudo strain value. This concept is explained with the help of Figure 1-2.

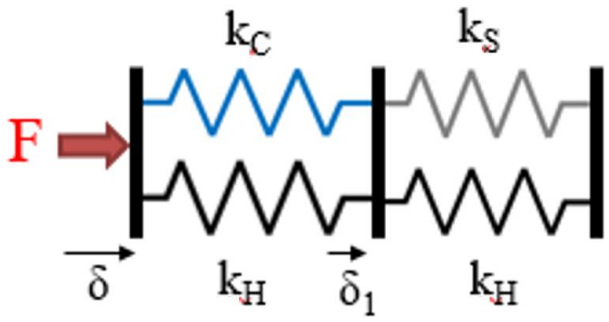

Figure 1-2. Simple 1D pin force model demonstrating conjugate stress sensing principle.

In the model shown in Figure 1-2, each sensor is represented as an independent spring in parallel with the host, with each section subject to the same force. The stiff and compliant sensor stiffnesses are denoted k_S and k_C, respectively, the host stiffness is denoted k_H, the far field load is denoted F, and the deflection of each section is δ and δ_1, respectively. Because force in series is constant, we can derive

$$F = (k_c + k_H)(\delta - \delta_1) = (k_s + k_H)(\delta_1). \quad \textit{Equation 1}$$

If the length of each spring is assumed equal for all springs, and if we know k_S and k_C, then the host stiffness, k_H, can be calculated as

$$k_H = \frac{k_c\varepsilon_c - k_s\varepsilon_s}{\varepsilon_s - \varepsilon_c}. \quad \textit{Equation 2}$$

Some examples of this in literature include a study where two 'springs' (microelectromechanical system capacitance sensors) of different stiffness are collocated and pressed into a surface so that both springs deform. From recording the deformation of each spring, the surface modulus can be calculated. The resolution of the sensor was 0.1 MPa over a range of 0.7-1.2 MPa [67]. In a similar study, a mechanical grasper was fabricated with a Plexiglas and a foam capacitive tip such that the Plexiglas and foam deformed when in contact with an object. By measuring the charge in each capacitor, the

stiffness of the object is calculated. The sensor was limited to 0.1-1 N of force and the accuracy was around 20% [68]. Another study used two pressure sensors of different areas to determine the stiffness of the host, in this case a muscle. The maximum force measured was approximately 16 N [69]. Another study used a piezoelectric capacitance sensor with a fiber optical intensity sensor to measure stiffness. The maximum force measured by the PZT was 2.5 N. The stiffness measurement had an error of approximately 20% [70]. Yet another study fabricated a finger mounted probe which has a compliant layer mounted on its surface. Then when pressed against a sample surface, the ratio of deformation in its own compliant layer to the deformation in the sample is used to estimate stiffness. Again the stiffness error was 20% [71].

This simple dual-stiffness sensor concept was expanded on by Majed et al via the conjugate stress (CS) sensor. CS sensing is a method for measuring host elastic modulus and strain energy density from two embedded, collocated sensors of different stiffnesses. The approach for solving the elastic state of the host structure is based on Eshelby's equivalent inclusion method. Eshelby solved for a unique solution of the elastic problem of an isotropic ellipsoidal heterogeneity embedded within an infinite isotropic elastic solid [72]. In conjugate stress sensing, the two sensors are idealized as embedded, ellipsoidal heterogeneities in the host structure and the strains recorded by each sensor are equal to the fictitious eigenstrain in Eshelby's method. Two sensors are used so that the measure of host modulus is independent of far field loading. In addition to the known strains of each sensor, the host modulus and far field strain are a function of each sensor's modulus and Eshelby's tensor [2]. One study in literature has used Eshelby's method for

stiffness prediction of fabricated composites, but not for damage accumulation as a function of host stiffness [73].

Two prior studies have analytically and numerically modeled such a CS sensor to determine the sensor properties that give the best sensitivity as well as the expected performance in measuring host stiffness. The first study analytically showed that as the compliant sensor became less stiff than the host structure and as the stiff sensor became stiffer than the host structure, the sensitivity of the conjugate stress sensor improved. The same study also showed that as the aspect ratio of the ellipsoid increased such that each inclusion resulted in higher strains the sensitivity improved. One concern with this result is that the higher strains in each inclusion mean stress concentrations are present at those locations leading to a loss of life in the structure [2]. The second study numerically solved for the sensitivity of surface-mounted conjugate stress sensors with different shapes (circular or square) and different bond layers. It was found that the bond layer thickness needs to be 0.2 times the sensor thickness in order for accurate modulus prediction. The study also investigated the effect of distance from the damage site on the conjugate sensor response. Damage was introduced as an embedded stiff inclusion and was only detected at a distance less than twice the length of the sensor from its midpoint. Lastly, changes in measured stiffness due to macroscale damage in the form of cracks was numerically modeled. The sensor showed limited response to very small crack depths, showed a large response to cracks of medium depth, and then saturated as the crack depth increased further [3].

The same two prior studies experimentally verified their findings with a surface-mounted conjugate stress sensor fabricated from resistive copper foil gauges. One gauge was stiffened by fixing it steel shim and the other was fixed directly to the host surface. In the first study, the modulus of acrylic, FR4, and aluminum (3, 24, and 76 GPa, respectively) were measured and showed reasonable agreement with the predicted sensor output from finite element analysis. A conjugate stress sensor was also fabricated using a PZT patch as the stiff gauge and in a single experiment measured the stiffness of FR4 with good agreement to finite element analysis [2]. In a subsequent study, another resistive copper foil gauge conjugate stress sensor (different architecture) was used to measure material stiffness as aluminum entered plasticity in a monotonic uniaxial tensile test. At the start of plasticity, the measured stiffness decreased drastically [3]. However, only a nondimensionalized measure of stiffness was generated by the CS sensor.

1.3. Research Gaps and Objectives

Currently, the majority of real-time SHM techniques rely on detecting macroscale damages, which do not facilitate the optimal logistics nor the saftest structures. Alternatively, sensors capable of tracking microscale damages are bulky, require an active input, or are susceptible to false positives due to changes in the external load state. A sensor that can measure microscale damages via the degradation of mechanical properties, such as stiffness, yield strength, strain hardening, and cyclic hysteresis in real-time would be of great importance in the health monitoring of these structures.

One stiffness sensor that has shown promise (passive, sensitive, small, and in-situ) but has limited published experimental results is a conjugate stress (CS) sensor. In addition to the limited quasistatic tensile experiments, the modeling of the sensor has varied widely. Different constructions and architectures have been studied independently and not compared to each other. Also, all previously reported CS sensors have been developed with a specific loading environment in mind and have not been tested over a range of stress states.

In Chapter 2 of this study, the design parameters of the CS sensor are systematically explored. The location of the individual CS sensing elements is parametrically varied to create guidelines for optimal implementation. Then, the performance of the CS sensor over a range of stress states is documented. Next, the CS sensor's thickness and modulus are parametrically varied to create guidelines for optimal sensor design for a host structure of known geometry and material properties.

In Chapter 3 of this study, two analytical models of the CS sensor are developed – an analytic pin force model and a simplified variational model. These models are intended to reduce the time and computational burden of reconstructing a FEM for every application. These models show much promise in estimating the host modulus with sufficient accuracy from the strains measured by the CS sensor. The analytic pin force model is the least computationally expensive and was used in this study to infer the stress-strain state of the host from the experimentally measured CS sensor strains.

In Chapter 4, the CS sensor experimentally demonstrates its the capability to detect a reduced modulus in a range of damaging environments. First, measuring instantaneous tangent modulus reduction during quasistatic tensile plasticity is demonstrated. Then, measuring modulus reduction due to fatigue is examined. In experiments, two types of sensor elements are used: (i) commercial resistive copper foil strain gauges; and (ii) specially developed fiber optic FPIs and FBGs. Fiber optic sensors were chosen as they offer many benefits once the sensor is taken from the benchtop to industry: lightweight, EMI immunity, corrosion resistant. Also, the fibers have similar geometry to fibers used in composite materials, making the sensors more easily embeddable if that is the future direction of this sensing technology.

2. Finite Element Parametric Evaluation

The first goal of this study is to provide a parametric evaluation of a surface-mounted CS sensor to better understand the consequences of the design options and to develop generic guidelines on best design options for different application scenarios. In detail, this section will provide a numeric parametric evaluation of the surface-mounted CS sensor's sensitivity with respect to its individual sensors' locations and the external load state. Then the sensitivity will be studied when the individual sensors' thicknesses and stiffnesses are parametrically varied.

It should be noted here that the rest of this chapter uses CS ratio as the reported output from the CS sensor. The CS ratio refers to the ratio of stiff sensor strain to compliant

sensor strain and is monotonically related to the stiffness of the host material. When the host geometric properties remain constant, then the CS ratio is monotonically related to the modulus of the host material. Both finite element models and analytical models have been proven to accurately convert the CS ratio to host stress-strain relation and thus host modulus [1] [74] [75]; however, the aim of this section is to analyze the CS sensor sensitivity's to changes in host stiffness, so the final conversion step is not included and the percent change in CS ratio is reported as a pseudo sensitivity.

2.1. Sensitivity versus Sensor Location

The finite element model used to parametrically vary the sensor location was constructed from brick elements in Abaqus shown in Figure 2-1. The host structure is modeled as an infinitely large plate compared to the CS sensor; to ensure this criterion is met, the host structure dimensions were increased until no change in the CS sensor response was seen. Similarly, mesh size was decreased until the FEM output saturated. A local damage is introduced to the host as a through thickness square section with a fifty percent reduction in nominal host modulus. In Figure 2-1, the undamaged host section is red, the damaged host section is white, the compliant sensor is green, and the stiff sensor is blue. The external excitation is an x-axis pressure applied at one the end of the host and fully constrained motion at the other. Two sizes of damage are inspected: damage with a) the same footprint as the CS sensor and b) twice the footprint as the CS sensor. Figure 2-1 shows damage twice the size of the CS sensor. Also, two sensor architectures are explored – one where the individual sensors are located on opposite sides of the host structure and one where the individual sensors are located on the same side of the host

structure. The compared output between all CS sensor locations is the percent change in CS ratio between pristine and damage states.

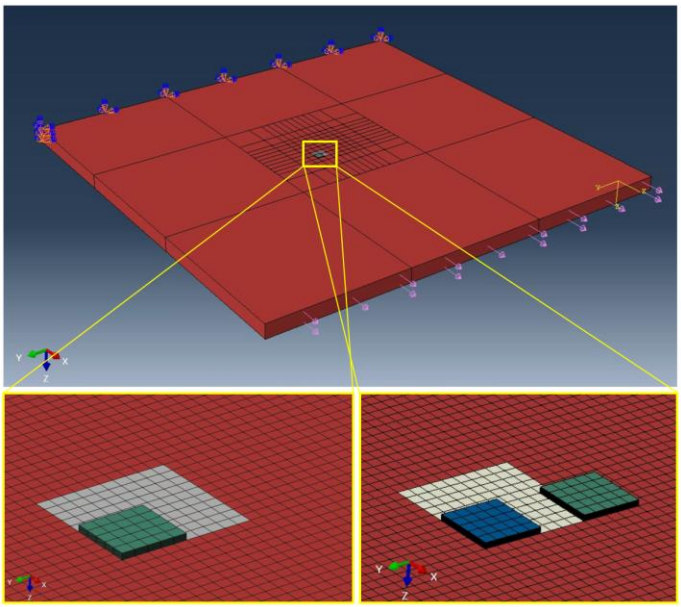

Figure 2-1. Finite element model used for varying sensor location and damage size.

In the first set of simulations, the same sided architecture was studied. The individual stiff and compliant sensor pads were spread from each other as damage was maintained locally at the stiff sensor location as shown in the inset images in Figure 2-2. The darker shaded background in Figure 2-2 indicates the whole CS sensor partially overlaps the damaged region and the white background indicates no overlap. The original modulus of the host structure was also varied and is displayed as differently colored lines. The results show that the percent change in CS ratio in the same sided architecture can have a nonmonotonic relationship depending on the location of sensors with respect to the damage location.

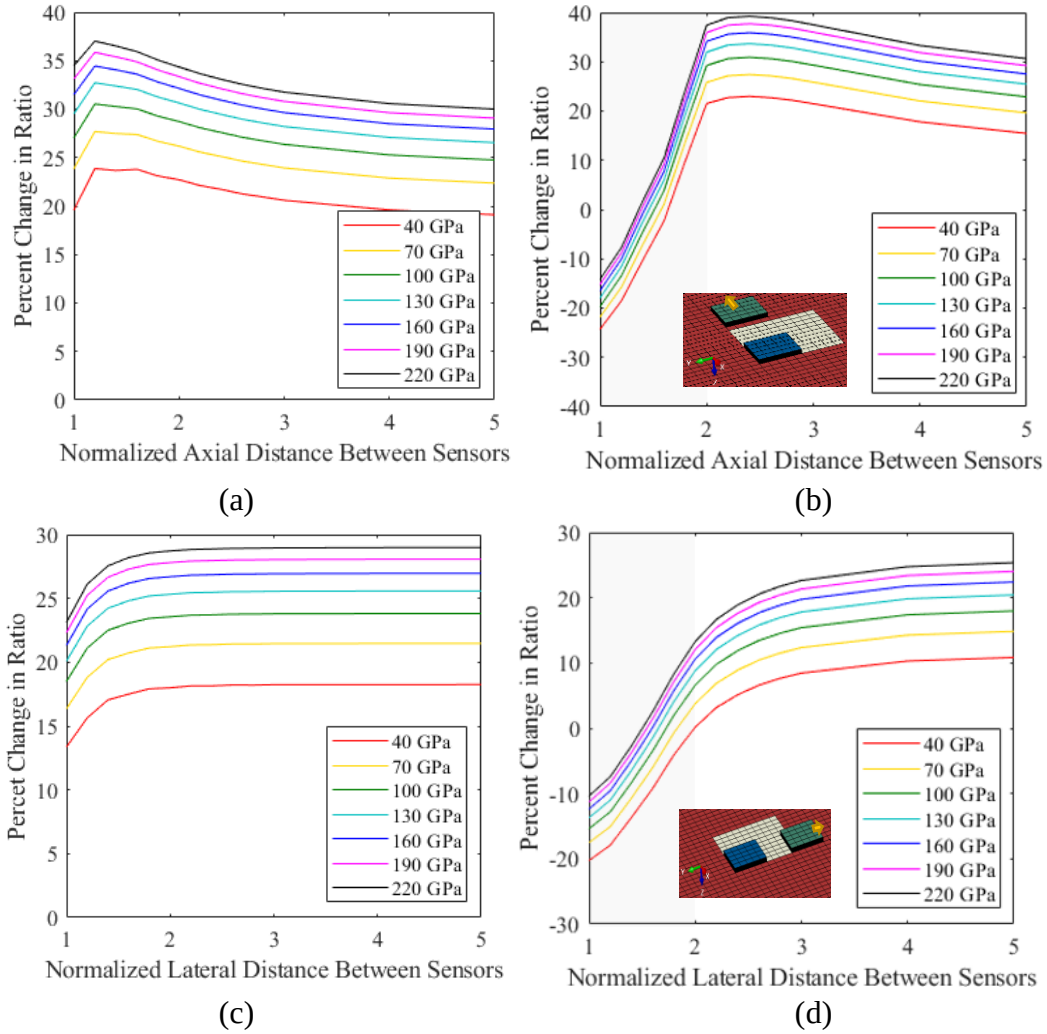

Figure 2-2. Side sided architecture as damage is moved away from the sensor location in the (a) axial direction relative to the loading direction when damage is the same size as sensor, (b) axial direction when damage is twice the size of the sensor, (c) lateral direction relative to the loading direction when damage is the same size as sensor, and (d) lateral direction when damage is twice the size as sensor.

For example, in Figure 2-2b it is seen that the CS ratio shows an initial decrease when both compliant and stiff sensors are within the damaged region. Then, as the compliant sensor moves away from the damaged region, the CS ratio increases. This behavior is observed because the host will have higher strains at the damaged location, and this is where the stiff sensor interacts with the host. The stiff sensor will try to hinder the increased strain due to damage, but these opposing factors are dominated by the increase in host strain due to damage and the CS ratio is seen to rise.

Similarly, the response of the same sided CS sensor was evaluated as the sensor locations were held a constant distance apart and damage was translated from the stiff sensor to the compliant sensor. The percent change in CS ratio versus damage location is shown in Figure 2-3. The light shaded background indicates when either the stiff or compliant sensor is partially on top of the damaged region. The dark shaded background indicates when either the compliant or stiff sensor is fully on top of the damaged region.

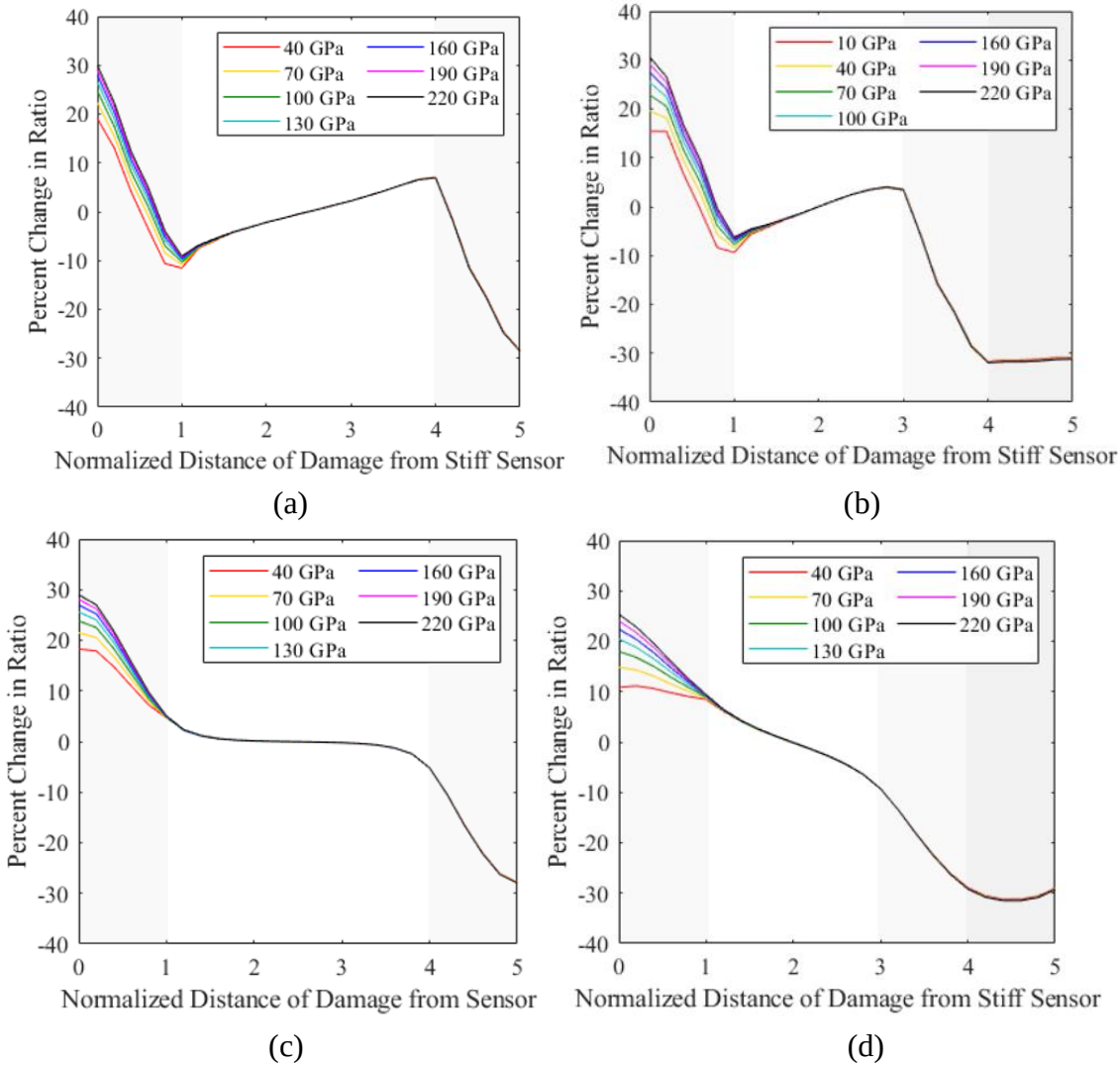

Figure 2-3. Same-sided architecture as sensors are (a) placed apart in the axial direction relative to the loading direction as damage is moved from the stiff to compliant sensor location when damage is the same size as sensor, (b) placed apart in the axial direction when damage is twice the size of the sensor, (c) placed apart in the lateral direction relative to the loading direction as damage is moved from the stiff to compliant sensor location when damage is the same size as sensor, and (d) placed apart in the lateral direction when damage is twice the size of the sensor

This nonmonotonic behavior of the CS sensor in same sided architecture makes determining the magnitude and location of damage difficult. In fact, the same sided architecture could not distinguish a stiffening damage indicator at the compliant sensor location from a softening damage indicator at the stiff sensor location. In order to use the CS sensor as intended (with monotonic performance), the individual sensors need to experience the same host deformations. The opposite sided architecture ensures that the stiff and compliant sensors interact with the same section of the host.

In the second set of simulations, the opposite sided architecture is modeled and the CS sensor is moved away from the damaged section in the axial direction relative to the loading direction. The simulations are repeated when the sensor is moved away from the damaged section in the lateral direction compared to the loading direction. Then both simulations are repeated for the larger damage scenario. The results for each case are shown in Figure 2-4. The darker shaded background indicates the CS sensor fully overlaps the damaged section of the host structure, the lighter shaded background indicates partial overlap, and the white background indicates no overlap.

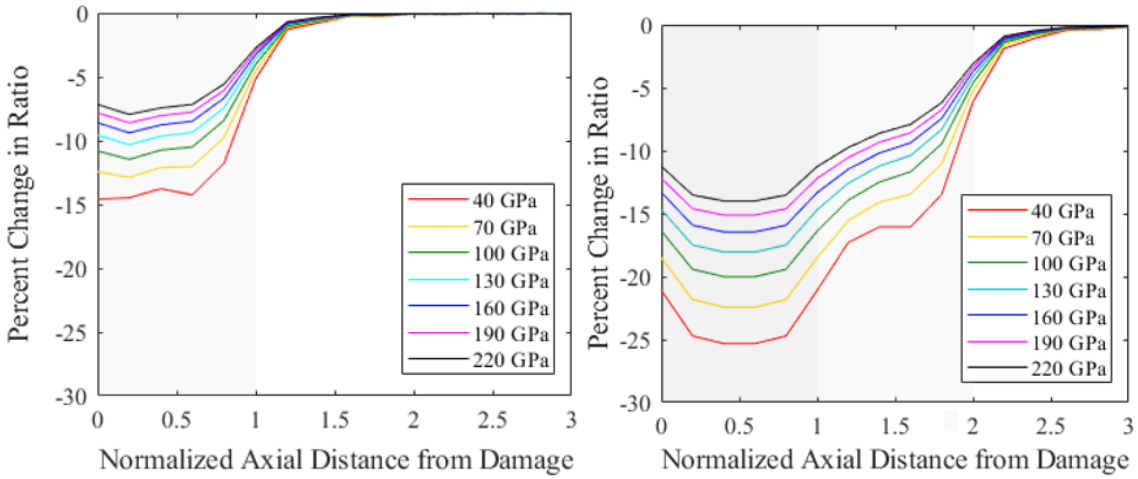

(a) (b)

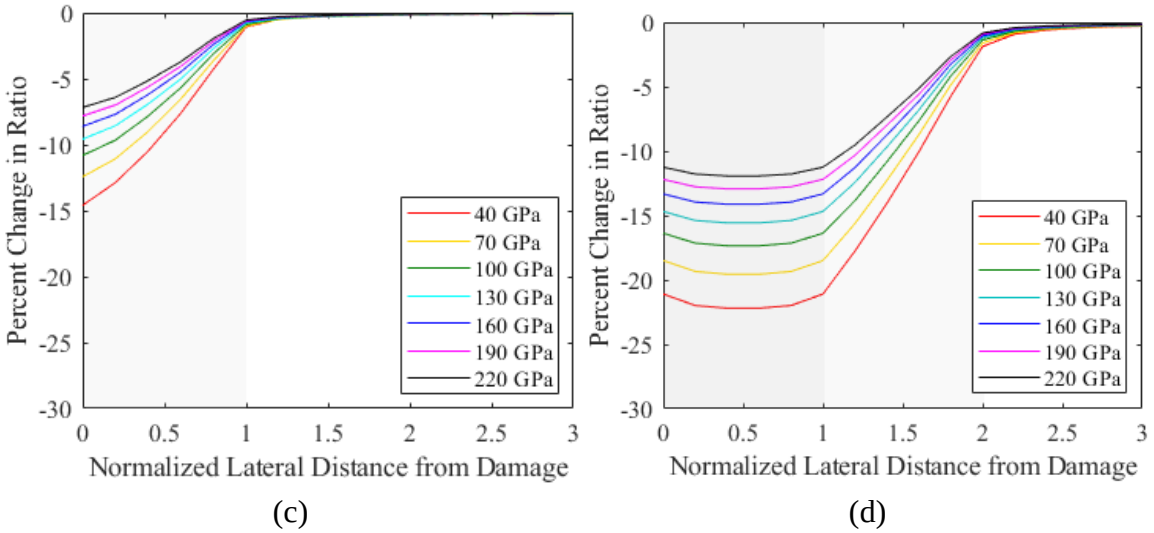

Figure 2-4. Opposite architecture as damage is moved away from the sensor location in the (a) axial direction relative to the loading direction when damage is the same size as sensor, (b) axial direction when damage is twice the size of the sensor, (c) lateral direction when damage is the same size as the sensor, and (d) lateral direction when damage is twice the size of the sensor.

There are three main takeaways from the results in Figure 2-4. First, the lateral and axial performances of the sensor are quite similar. The differences are due to the strain concentrations present at the edges of the sensor normal to the loading direction. Second, the change in CS ratio is largest when the damage is geometrically larger. Since the damaged modulus is the same in both damaged cases, one might expect the change in CS ratio to be the same. However, it should be recalled that the CS ratio is a representation of stiffness, so if the geometric properties of the damage change, then so will the host's stiffness and thus the CS ratio as well. Third, it is seen that the change in CS ratio is largest when the sensor is in contact with the damaged section and transitions to zero as the damage is moved away. When there is no sensor overlap with the damage, the change in CS ratio is nearly zero indicating the sensing footprint of the sensor is strictly constrained to the local region of the sensor.

In application, this means the CS sensor needs to be arrayed with the same dimensions as the minimum required damage tracking size. For example, if damaged zones cannot exceed 1cm, then the CS sensors should be arrayed with 1cm separation. However, the most susceptible sections of a structure are usually known a priori, so the sensors can be intelligently placed to monitor damage without the need for an excessive array.

From the parametric analysis of sensor location, it is evident that the opposite sided architecture of the CS sensor is suited best. Although the same sided architecture offered a larger sensing footprint, the nonmonotonic behavior requires much more post-processing and a priori information to digest and turn the CS sensor reading into a damage estimate. Also, we will see in the next section that the CS sensor has different responses to bending and axial loads and having the opposite configuration will be helpful in identifying bending or axial strains. However, because the sensing footprint of the CS sensor in the opposite sided architecture is strictly local, if damage occurs outside the sensor footprint, it will go undetected. Therefore, the opposite sided architecture can be paired with knowledge of known susceptible locations or can be arrayed to produce better host structure coverage.

2.2. Sensitivity versus Stress State

As alluded to in the previous section, the type of external load applied to the host structure can affect the CS sensor output. When using a single axis CS sensor, there is a different response to the same damage magnitude when the loading direction changes as the CS sensor can only sense strains due to Poisson's effect in the other directions. To

account for this, a multiaxial CS sensor can be used. However, a multiaxial CS sensor is still prone to changes in stress state. For example, when an axial load is present in the host, the individual stiff and compliant sensor share the same sign of strains. On the other hand, if a bending load is present in the host, then the stiff and compliant sensors will have strains of different signs, causing a negative CS ratio. To decouple the effect of load type, a CS sensor array is proposed where the CS sensors in the array have different properties, and thus different sensitivities in different stress states, allowing for the decoupling of stress state from damage.

To summarize, a single uniaxial CS sensor shows independence from load magnitude, but not load direction or state. A single multiaxial CS sensor shows independence from load magnitude and load direction but not load state. And a CS sensor array can show independence from load magnitude, direction, and state.

To better understand the CS sensor behavior in relation to stress state, the CS ratio is plotted as the external load changes from pure axial loading to pure bending loading in Figure 2-5. The scenario of a pristine host and a damaged host with a 20% reduction in modulus are included. The CS ratio is positive when axial loading dominates, is negative when bending dominates, and contains an inflection point when the axial and bending strains have equal but opposite magnitudes. If a structure experiences complex loading states, then this transition in CS ratio can obscure the presence of damage from a single CS sensor.

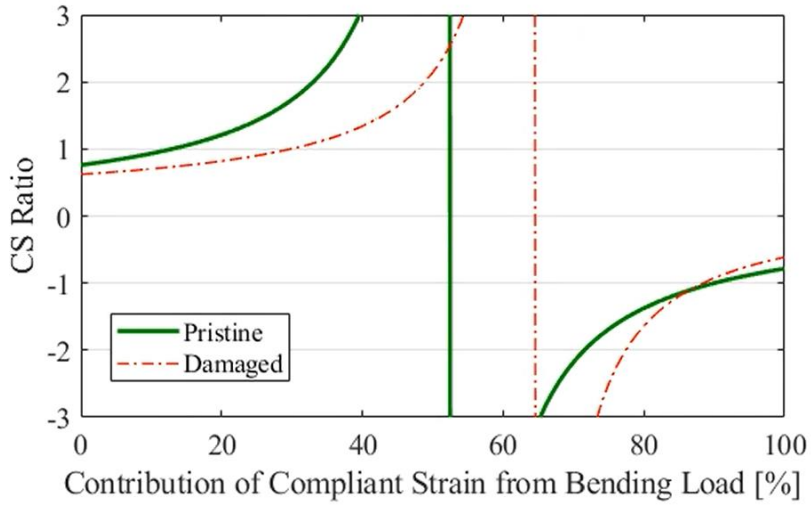

Figure 2-5. CS ratio as the load type changes from bending dominant to axial dominant. A change in CS ratio can either be due to a change in load type or due to damage.

Primarily, there are two areas of poor CS sensor performance in Figure 2-5. The first scenario is when the strains due to axial and bending loads cancel and there is no net strain in the host structure. As this is a passive sensor, without any external load the CS sensor cannot assess the damage state of the host structure. This corresponds to the inflection point around 50%. Although the change in CS ratio is extreme just offset from the inflection point, the strains measured are small and so this is an area of large sensor error. This scenario will always be a concern in passive sensors, though without any external load the structure should not be experiencing degradation. The second scenario corresponding to poor CS sensor performance is when the damaged and pristine CS ratios do not change. This occurs in Figure 2-5 when the lines cross over around 85%. At this point, the additional bending introduced by the stiff sensor due to modulus softening and the additional bending from the external load due to modulus softening are cancelling resulting in zero additional strain. However, unlike the first scenario of poor sensor performance, this scenario is avoidable.

A second CS sensor with different sensitivity than the first CS sensor is added to the CS sensor array. The new CS sensor has proposed different sensitivity due to its different geometry, and thus has different behavior under axial and bending loading states. For example, a thicker CS sensor will have larger obtrusivity under the same host bending load, shifting the inflection point to a scenario where higher bending loads are required. By monitoring both CS sensors simultaneously, we obtain full coverage of all load types.

Figure 2-6 shows that a CS sensor with stiff sensor having twice the thickness of the nominal CS sensor has shifted the cross over point (point of zero change between pristine and damaged ratios) from 85% to 90%. Figure 2-6 plots the percent change in CS ratio due to a 20% reduction in host modulus as the load type changes from pure axial to pure bending loads. Due to the different behavior of the CS sensors within the array, the load state can be decoupled from damage magnitude and excitation magnitude.

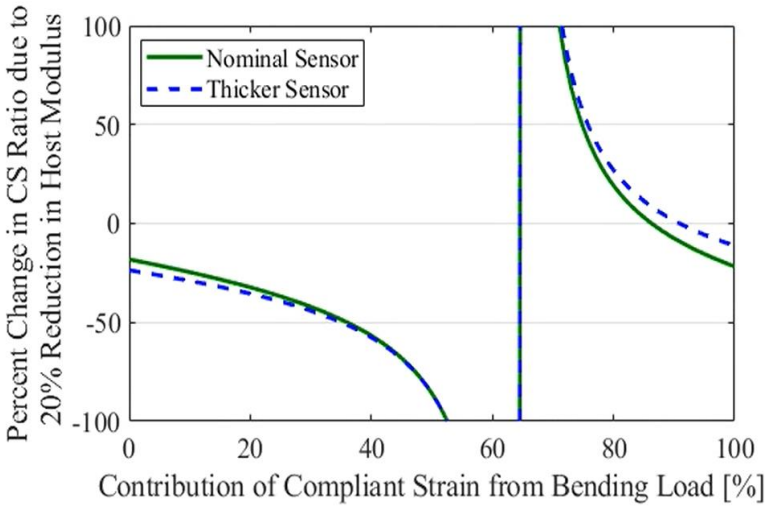

Figure 2-6. CS sensors of different geometries help decouple load state and damage. A CS sensor with thicker stiff sensor shows different behavior depending on the dominant load, thus the load state can be decoupled from damage.

From the stress state analysis, a surface-mounted CS sensor with three multiaxial individual sensors (a compliant, stiff, and thicker stiff sensor) can decouple host stiffness, the external load magnitude, the external load direction, and the external stress state, i.e. the contribution of bending and axial loads. One scenario where the CS sensor cannot detect damage is when the net strain on the host is zero as it is a passive sensor. However, if the net host strain is always zero then no damage is being introduced to the structure.

2.3. Sensitivity versus Modulus and Thickness

The opposite-sided architecture was determined the most sensitive and showed monotonic sensitivity, so the CS sensor's sensitivity was parametrically evaluated in that configuration as the individual sensor moduli and thickness were varied. To speed the parametric evaluation, a quarter symmetric model was generated in Abaqus using 3D brick elements shown in Figure 2-7. Initially, the element size of the model was decreased until the results stabilized. Then the host structure dimensions were increased until the CS sensor showed no change in output ensuring the infinite host assumption is met.

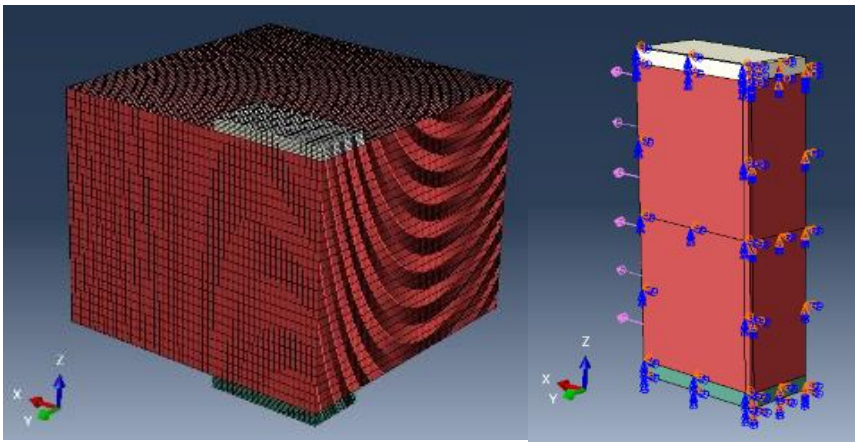

Figure 2-7. FEM of quarter symmetric CS sensor in surface-mounted opposite-sided architecture.

For the first parametric study, the moduli of both the stiff sensor and the host were varied and the sensitivity was gathered from the strains reported in the FEM. Sensitivity is first defined as

$$S = (\varepsilon_C - \varepsilon_S)/\varepsilon_H \quad \textit{Equation 3}$$

where S is sensitivity, ε denotes strain, and the subscripts C, S, and H represent the compliant sensor, stiff sensor, and host, respectively. This definition of sensitivity is the same as in the first reported analysis for CS sensing [1]. From the definition, it is obvious the most different sensor pair possible is desired and is confirmed in Figure 2-8. Figure 2-8 shows the sensitivity of both the embedded configuration as analytically solved and reported in [1] and the new surface-mounted configuration numerically solved. In both cases, as the stiff sensor modulus increases compared to the compliant sensor modulus, the sensitivity increases.

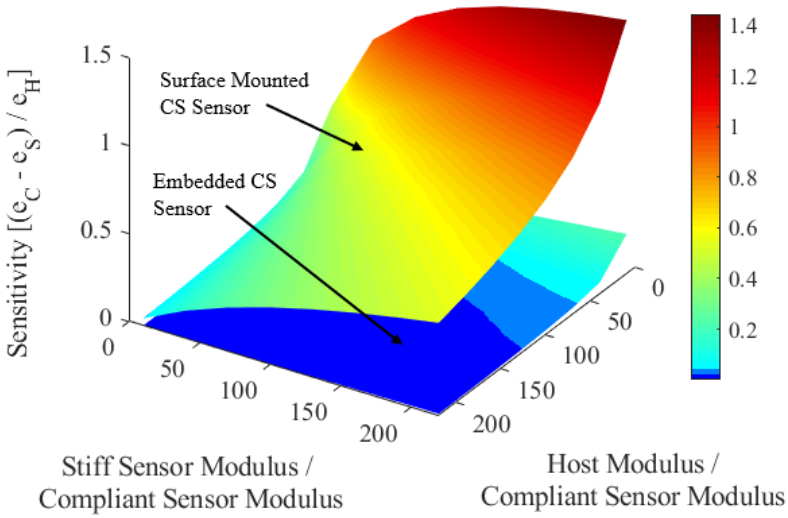

Figure 2-8. Sensitivity of CS sensor as stiff sensor modulus and host modulus are parametrically varied for the surface-mounted numerical solution and embedded analytical solution; sensitivity defined as difference in individual sensor strains divided by far field host strain.

The surface-mounted configuration also shows much greater sensitivity than the embedded configuration. This is because the individual stiff and compliant sensors are no longer independent of each other. The stiff sensor causes a local bending and the compliant sensor, mounted on the opposite side of the host structure, increases its reported strain due to this localized bending. Therefore, the sensitivity increases because the difference between stiff and compliant strains is enhanced. This demonstrates that by surface-mounting the sensor, the sensitivity of the CS sensor can be improved.

Additionally shown in Figure 2-8, as the stiff sensor modulus increases compared to the host modulus, the sensitivity increases, demonstrating the desire for a significantly stiff 'stiff sensor'; however, inutitively this should not be true. In addition to the large stress concentrations caused by a stiff inclusion, if the stiff sensor becomes overly stiff, it will oppose not only the local axial defomration, but the bending deformation of the host as well, ulitmately decreasing sensitivity. Because of this incompatibility, a new defintion of senstivity is determined using the classic definition for a sensor: change in sensor output divided by change in measurand. In the case of the CS sensor, sensitivity is calculated as

$$S = \Delta R/\Delta E \quad \textit{Equation 4}$$

where S is again sensitivity, R is CS ratio, and E is host modulus. The change in CS ratio and host modulus are relative to the original, healthy state of the material.

Figure 2-9 shows the behavior of the new definition of CS sensor sensitivity as stiff sensor modulus and host modulus are varied from 10 GPa to 220 GPa. Due to the new definition of sensitivity, the plot cannot be normalized by the compliant sensor modulus,

so the compliant sensor modulus is fixed at 1 GPa. It is seen that as the stiff sensor becomes too stiff compared to the host modulus, the sensitivity decreases. Again, this drop in sensitivity is due to the opposition to local host bending caused by a stiff sensor which is too stiff.

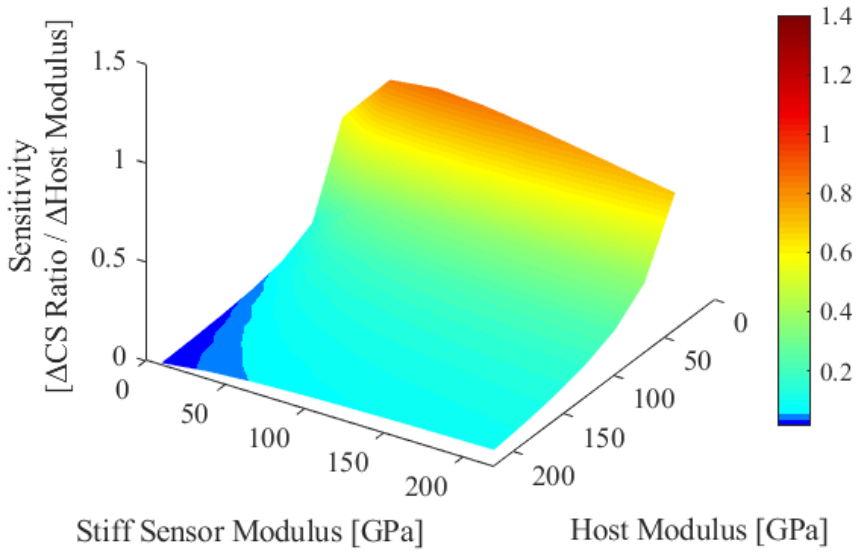

Figure 2-9. Sensitivity of CS sensor as stiff sensor modulus and host modulus are parametrically varied while the compliant sensor modulus is fixed at 1 GPa; sensitivity is defined as change in CS ratio divided by change in host modulus.

To further understand this CS sensor behavior and to create a tool for predicting the transition in sensitivity, the host stiffness is parametrically varied in relation to the stiff sensor stiffness, i.e. thickness is varied in addition to modulus. The CS ratio as a function of host thickness and modulus is shown in Figure 2-10. It is seen that when the stiff sensor stiffness is too large compared to host stiffness, the CS ratio no longer holds as a monotonic index of host modulus. This transition is made obvious in the second surface plot in Figure 2-10, where normalized stiff sensor stiffness (stiff sensor stiffness normalized by four times the host stiffness at every point) is plotted against host modulus and thickness. It is seen that the nonmonotonic transition in CS ratio corresponds to when

the stiff sensor stiffness eclipses the host stiffness, i.e. when normalized stiff sensor stiffness becomes greater than 0.25.

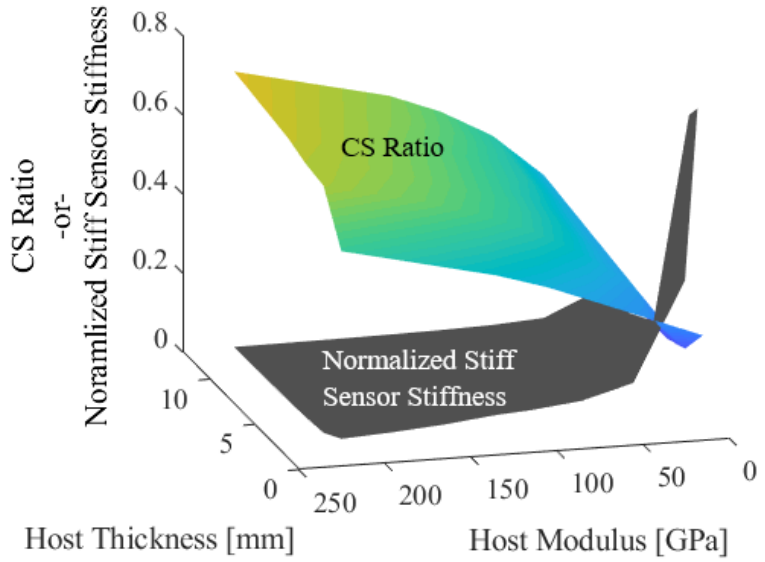

Figure 2-10. CS Ratio shows nonmonotonic behavior as the host stiffness decreases and it is seen that the nonmonotonic behavior begins when the stiff sensor stiffness eclipses the host stiffness.

From this parametric analysis of sensitivity of the CS sensor with respect to individual sensor moduli and thickness, it is apparent surface-mounting the individual stiff and compliant sensors increases the sensitivity of the CS sensor compared to independently embedding the sensor pair. Also, the best sensitivity is achieved when the compliant sensor is as compliant as possible and when the stiff sensor has high modulus but low bending stiffness compared to that of the host modulus and bending stiffness. If the stiff sensor stiffness becomes larger than the host stiffness, then a nonmonotonic behavior is seen and sensitivity is lost. However, if the stiff sensor is too compliant then the sensor does not oppose the host deformation and begins to act like an extensometer or second compliant sensor and again sensitivity is lost. Within the CS sensor scheme, there is an optimal design where maximum sensitivity is achieved. Generating a more specific

design criteria is the focus of future work and can be greatly helped by the development of analytical models, which is discussed in an upcoming section of this dissertation.

2.4. Case Study – Fatiguing/Corroding Pipeline

In this section, the most sensitive multiaxial surface-mounted CS sensor arrangement determined from the above analysis is applied in a numerical case study of a pipeline experiencing fatigue and corrosion. Pipelines are a major staple of the energy industry as well as used to transport water, gas, and sewage in most cities around the world. In service, the pipes are exposed to aggressive environmental stresses including thermal, chemical, and mechanical loads. After continuous exposure, the pipes may experience pitting corrosion and fatigue damage, which can degrade the structural integrity of the pipes and eventually lead to cracking, potentially causing significant economic and environmental losses [28]. In this case study, damage is presented as a loss in modulus along the entire structure: similar to uniform corrosion or fatigue cycling. In seawater corroded steel, the modulus decreased by 20% when the degree of corrosion (a measure of pitting) was 35% [55]. Also, in fatigued high carbon steel, the modulus decreased by 25% after 75k harmonic cycles of strain levels well within the elastic limit [44]. So in this case study, damage is introduced as a 20% reduction in the modulus of a steel pipe.

The pipe geometry is based on ASTM Standard A312, with outer pipe diameter 114.78 mm and pipe wall thickness 4.78 mm. Since placing the sensors on the inside of an in-use pipe is a liability, the same-sided surface-mount architecture is employed. Unlike in the local damage scenarios explored in the earlier section, in the case of a pipe, early damage

before cracking can be considered globally uniform. This means the same-sided architecture can be used to improve the sensing footprint and will behave monotonically, though with lower sensitivity than the opposite-sided configuration. Figure 2-11 shows the CS sensor array surface-mounted on the outside of the pipe. Though the pipe presents a new geometry compared to the earlier analyzed flat plates, the pipe wall can be treated as an infinite flat plate compared to the CS sensor. Then, from the earlier presented plate analysis, it is expected that a stiff sensor with modulus 200 GPa and thickness 0.71 mm will be most sensitive when the host modulus is 200 GPa (the nominal modulus of steel).

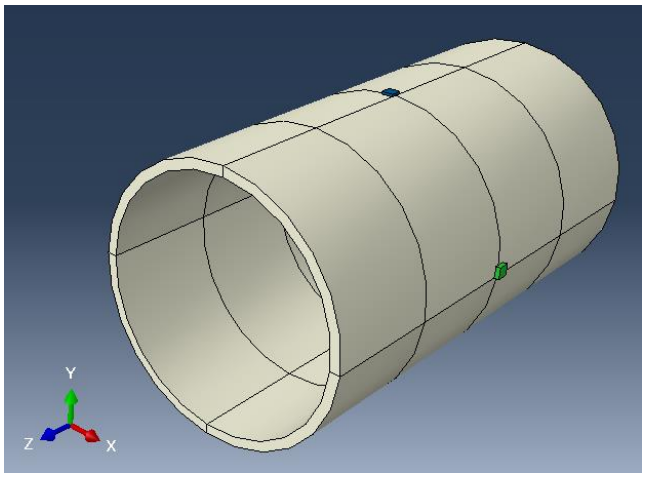

Figure 2-11. FEM of CS sensor surface-mounted on outside of a pipe.

To verify the selected CS sensor thickness provides maximum sensitivity, the sensor thickness was parametrically varied from 0.5 to 0.9 mm. The sensitivity, reported in $S = \Delta R/\Delta E$ Equation 4, is plotted in Figure 2-12 and shows that the maximum sensitivity is achieved at 0.60 mm for radial loads and 0.65 mm for axial loads. The difference between maximum sensitivity of the axial and radial loads in a pipe versus the maximum sensitivity from the flat plate analysis is attributed to the different geometries associated with the pipe wall. It is also seen that the sensitivity is not significantly impacted by the

thickness of the stiff sensor; this is because the host material modulus is already very stiff compared to the sensor modulus.

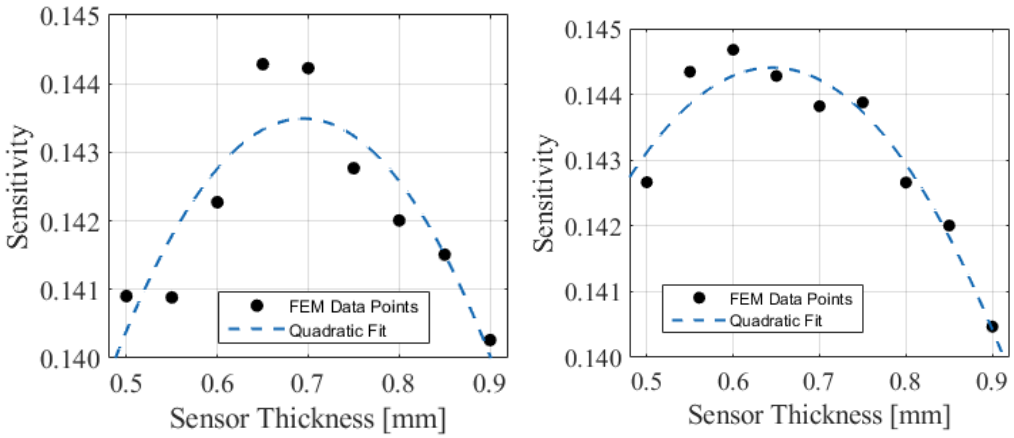

Figure 2-12. CS sensor sensitivity as sensor thickness is varied under (a) axial load and (b) radial load.

Another consideration when choosing sensor thickness is the stress concentration caused by the sensor's inclusion in the system. The increase in stress is linearly affected by the stiff sensor pad thickness but remains under 10% in the range studied. While having some stress concentration is advantageous to ensure failure occurs at the sensor location, it also cannot be exceedingly large in order to maintain the expected life of the system. In this case study, a final sensor thickness of 0.65 mm was chosen as it showed the highest sensitivity and a lower stress concentration of 6.5%.

As discussed earlier, the pipe geometry differs form a flat plate. One such difference is that axial and circumferential strains are expected to dominate versus the axial and bending strains present in the flat plate. In Figure 2-12, the sensitivity was plotted for such axial and radial loads. Unlike for the flat plate where bending and axial strains presented with strains in the same direction, radial and axial two loads present with maximum strains in different directions; axial loads cause primarily axial strains and

radial loads cause primarily circumferential strains. Therefore, by measuring the biaxial strains on the sensor pads, the damage state can be determined independent of load type or magnitude.

Figure 2-13 shows that a 20% reduction in pipe modulus corresponds to a 6% change in CS ratio across the entire load type spectrum depending on which direction of sensor strains is dominate. If axial strains show the highest magnitude, then axial loads are dominating and the solid green line can be used to determine reduction in modulus; likewise, if circumferential strains show highest magnitude, then radial loads are dominating and the dashed blue line can be used to determine reduction in modulus.

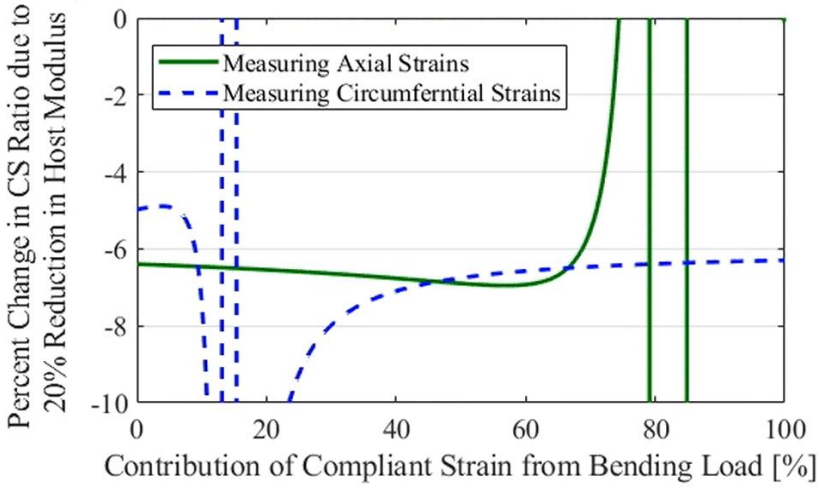

Figure 2-13. Percent change in CS ratio when damage is introduced across the spectrum of different loading scenarios. When axial loads dominate, the sensor behaves well when recording axial strains (solid green line) and when radial loads dominate, the sensor behaves well when recording circumferential strains (dashed blue line).

Unlike for the flat plate, the inflection points present in Figure 2-13 are from Poison's ratio effects, which is why they are located near the ends of the spectrum and not the middle. It is clear the CS sensor is able to identify damage in all types of loading scenarios. To determine the exact contribution of each load type, the ratio of the biaxial

strain magnitudes can be used. Alternatively, a second CS sensor with different geometry can be added. The response is shown in Figure 2-14, where a stiff sensor with longer circumferential footprint shows a much different behavior than the nominal stiff sensor under the same damage and loading conditions. This allows for the easy decoupling of damaged modulus, load state, and load magnitude.

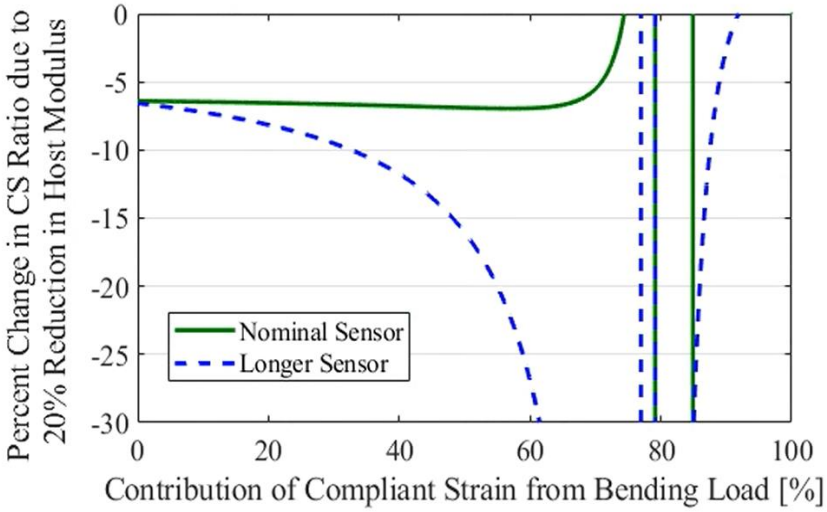

Figure 2-14. CS ratio behavior of two different geometries across spectrum of different loading scenarios. Focusing on the axial strain behavior we can see clear difference in signal depending on load state in the longer CS sensor, thus we can decouple load state from damaged modulus.

2.5. Summary of Parametric Evaluation

In literature, the CS sensor has shown proven experimental results, but the sensor design has varied significantly. Therefore, this section aimed to provide a parametric evaluation of the sensitivity of CS sensor given many different CS sensor designs.

First, the architecture of the surface-mounted CS sensor was parametrically evaluated. The opposite-sided architecture showed higher sensitivity to global damage than the same-sided architecture. Also, the opposite-sided architecture had monotonic behavior to local damage whereas the same-sided architecture had nonmonotonic behavior.

Additionally, the opposite-sided architecture showed much better sensitivity that the embedded design due to the coupling of the individual stiff and compliant sensors. Therefore, the opposite sided architecture is preferable. However, the opposite-sided architecture only shows sensitivity to damage within the geometric footprint of the sensor.

Second, the effect of stress state on the surface-mounted CS sensor performance was parametrically evaluated and it was found that the CS sensor has different performance when the stress state changes. For example, if the loading changes from bending to axial, the CS ratio changes. To decouple the change in external load from change in stiffness due to damage, it was proposed to add a third individual sensor with different geometry to the original CS sensor pair. With an array of three sensors with different stiffnesses, the load magnitude, load state, and damage state of the host modulus can be decoupled.

Third, the CS sensor modulus and thickness was parametrically varied and revealed an optimal design for maximum sensitivity as described by $S = \Delta R/\Delta E$ Equation 4, namely change in sensor output over change in measurand. The maximum sensitivity was found when the compliant sensor was as compliant as possible and stiff sensor had high modulus compared to the host, but not high bending stiffness.

After the parametric evaluation was completed, a virtual case study using the surface-mounted CS sensor to monitor a fatiguing and corroding pipe was presented. Under

different load magnitudes and stress states, i.e. radial or axial loads, the damage to the pipe can accurately be estimated and tracked using the surface-mounted CS sensor.

3. Models for the CS Sensor

Constructing a finite element model (FEM) for every structure can be time consuming and computationally expensive. Therefore, a pin force model and a variational model are developed to provide quick, computationally inexpensive estimates of the host stress-strain state given the CS sensor measured strains.

3.1. Pin Force Model

A simplified, closed-form pin force model is proposed for ease of universal use. The opposite-sided, surface-mounted CS assembly with the pin force model overlaid can be seen in Figure 3-1.

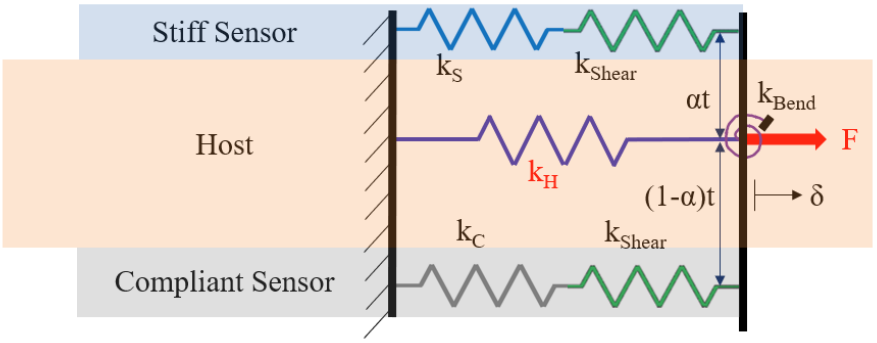

Figure 3-1. Opposite-sided, surface-mounted CS sensor. Overlaid is the pin force model used to obtain a CS nonlinear mapping function from sensor strains to host stress-strain.

The pin force model captures the prominent sensor interactions and deformation mechanics of the assembly. The springs representing the stiff and compliant sensors have

stiffness k_S and k_C, respectively. The host has axial stiffness k_H. Each of these stiffnesses follows the form of

$$k_i = \frac{E_i A_i}{L_i} \quad \textit{Equation 5}$$

where A is the cross-sectional area, L is the length, and i refers to the subscripts s, c, or H for the stiff sensor, compliant sensor, and host, respectively. A bending spring is included in the pin force model as it is known that the asymmetric location of the stiff sensor will cause local warpage. The bending stiffness of the assembly is assumed to be dominated by the host and follows

$$k_{Bend} = \frac{E_H I_H}{L_H}, \quad \textit{Equation 6}$$

where I is the area moment of inertia. Similarly, shear springs are included in the pin force model as it is known that local shear strains will occur due to the inclusion of both sensors. The shear stiffness is defined as

$$k_{Shear} = \frac{E_H L w_H}{2t(1+\nu)} \quad \textit{, Equation 7}$$

where w_H is the width of the host, t is the thickness of the host, and ν is the Poisson's ratio of the host. An unknown axial force, F, is applied to the host causing the structure to stretch with displacement, δ. The variable α is an application specific variable between 0 and 1, which can be tailored to help account for the neutral axis shift caused by the inclusion of the CS sensor.

The collocated stiff and compliant sensors, and the region of the host under their footprint are modeled as parallel springs; this accounts for some of the interaction between the stiff and compliant sensors. The bending spring is placed at the end of the assembly causing

all sensors to react to the same bending angle. The shear stiffness of the host is represented as a spring in series with both the stiff and compliant sensors as the shear contribution from each will be significantly different. The small angle approximation is made so that the deformation of the system can be solved purely in terms of axial displacement. The CS sensor nonlinear mapping function from the pin force model is

$$E_H = \left(\frac{t^2}{I_H} + \frac{2t(1+\upsilon)}{w_H L_1^2}\right)\frac{E_S A_S \alpha R - E_C A_C (1-\alpha)}{1-R}, \quad \textit{Equation 8}$$

where again R is CS ratio of stiff strain to compliant strain. If the compliant sensor modulus is assumed negligible compared to stiff sensor modulus, then $E_H = \left(\frac{t^2}{I_H} + \frac{2t(1+\upsilon)}{w_H L_1^2}\right)$

$$E_H = \left(\left(\frac{t^2}{I_H} + \frac{2t(1+\upsilon)}{w_H L_1^2}\right) A_S \alpha\right) * E_S \frac{R}{1-R}. \quad \textit{Equation 9}$$

The first term in parenthesis in $E_H = \left(\left(\frac{t^2}{I_H} + \frac{2t(1+\upsilon)}{w_H L_1^2}\right) A_S \alpha\right) * E_S R$ 1 − . Equation 9 contains the independent bending and shear deformation contributions calculated from the pin force model. The second half of $E_H = \left(\left(\frac{t^2}{I_H} + \frac{2t(1+\upsilon)}{w_H L_1^2}\right) A_S \alpha\right) * E_S \frac{R}{1-R}$. Equation 9 is reminiscent of the dual-spring term in $k_H = \frac{k_c \varepsilon_c - k_s \varepsilon_s}{\varepsilon_s - \varepsilon_c}$. Equation 2. Based on $S = (\varepsilon_C - \varepsilon_S)/\varepsilon_H$ Equation 3 and $E_H = \left(\left(\frac{t^2}{I_H} + \frac{2t(1+\upsilon)}{w_H L_1^2}\right) A_S \alpha\right) * E_S \frac{R}{1-R}$. Equation 9, a representative relation between the normalized host modulus, E_H/E_S, and the CS ratio, R, for a specific host structure geometry is shown in Figure 3-2. If the host geometry changes, the curve will display different absolute values, but the general trend of the curve will remain the same.

, Equation 8 can be simplified to

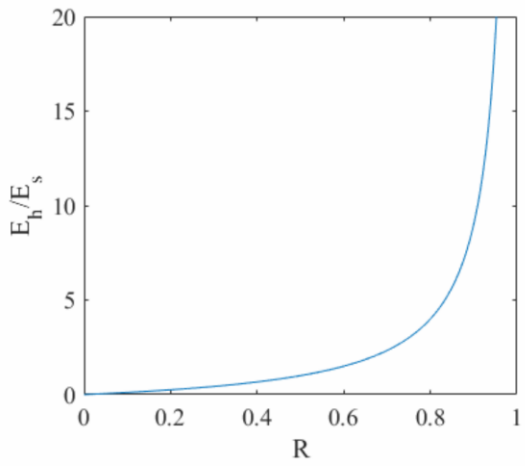

Figure 3-2. CS ratio as a unique index of host modulus. In this specific example, t = 2, v = 0.3, w = 12.5, L = 10, and α = 0.5.

The applied axial force, *F*, cannot be solved directly from the CS ratio. Instead, the solution requires the individual values of the measured strains from the stiff and compliant sensors, ε_s and ε_c. Axial force is calculated from

$$F = E_H A_H(\alpha\varepsilon_C + (1-\alpha)\varepsilon_S) + (E_S A_S \varepsilon_S + E_C A_C \varepsilon_C)\left(1 + \frac{2\alpha t^2(1-\alpha)(1+\upsilon)}{L^2}\right). \quad \textit{Equation 10}$$

The engineering stress in the host structure can be estimated by dividing $F=E_H A_H(\alpha\varepsilon_C + (1-\alpha)\varepsilon_S) + E_S A_S \varepsilon_S + E_C \boldsymbol{AC}\varepsilon C\left(1 + \frac{2\alpha t^2(1-\alpha)(1+\upsilon)}{L^2}\right)$. Equation 10 by the host cross sectional area, A_H.

The simplified deformation field assumed in the host for the pin force model differs from the actual deformation expected in the host in experiment, as shown in Figure 3-3. In particular, the axial displacements in the pin force model are piecewise linear while the nonlinear slope is expected in experiments, especially when shear deformations dominate. There is also a discontinuity in the bending of the host where the footprint of the CS sensor ends. Both of these simplifications are expected to limit the accuracy of the pin force model.

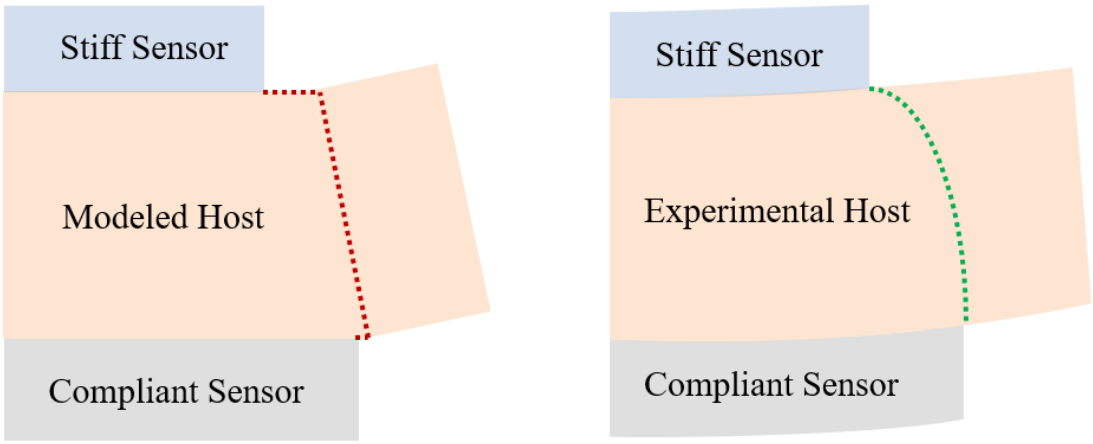

(a) (b)

Figure 3-3. Pin force model estimated deformation (a) versus expected experimental deformation (b).

To verify the pin force model, it was compared to a FEM with the host geometry used in the planned experiments. The FEM, shown in Figure 3-4, is constructed in Abaqus using 3D block elements. The stiff sensor is modeled as a rectangular pad tie-constrained to the host simulating perfect bonding between sensor and host. The strains on top of the sensor pad are averaged and assumed to represent the strains measured by the stiff sensor in experiment. The compliant sensor is assumed to offer negligible resistance to the deformation of the host and thus directly measure the strain on the host structure's surface. The boundary conditions are encastre on end of the host and axial displacements are defined at the other end, mimicking the experiments planned on the mechanical testing system (MTS). The host elastic modulus and host thickness are varied in the FEM to generate a transfer function that relates the host elastic modulus and host thickness to CS ratio.

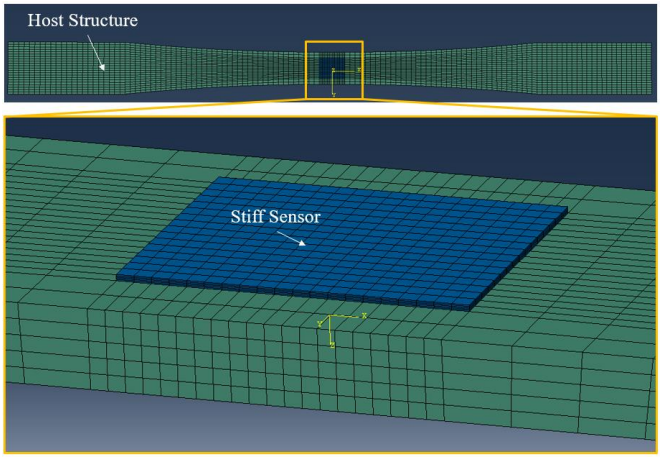

Figure 3-4. Finite element model of CS sensor and host geometry from experiment used to verify the pin force model.

A contour map of the CS nonlinear mapping function from the pin force model is shown in Figure 3-5a. The contour map is plotted against host modulus (10 - 250 GPa) and host thickness (1 - 15 mm) on the horizontal and vertical axes, respectively. A contour map of the percent error in CS ratio between the FEM and pin force model is shown in Figure 3-5b.

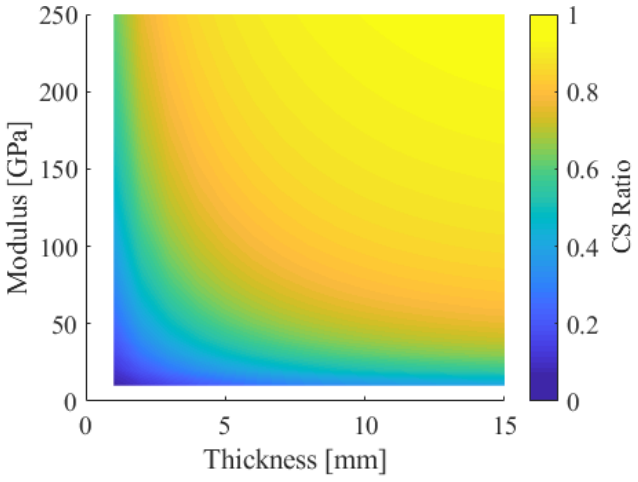

(a)

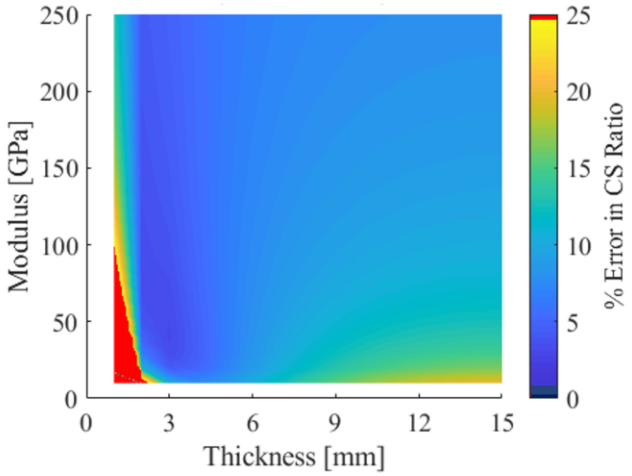

(b)

Figure 3-5. Contour maps when host thickness and host modulus are varied of (a) the CS ratio obtained from the pin force model and (b) percent error of the CS ratio between pin force model and FEM. The stiff sensor has modulus 200 GPa and thickness 0.2mm. α was set equal to 0.33.

The sensitivity of the FOCSS is indicated by the contour gradient in Figure 3-5a; where the colors change rapidly is an area high sensitivity. Expectedly, the sensitivity of the FOCSS increases as the host stiffness decreases (i.e., host modulus and/or thickness decreases). However, this can become an issue when using the FOCSS to detect changes in small host stiffness as small errors in the reported CS ratio can lead to big errors in the predicted host modulus. Conversely, the FOCSS has low sensitivity when the host stiffness is large. In this case, the stiff sensor has modulus 200 GPa and thickness 0.2 mm. When the host becomes significantly stiffer than the stiff sensor (i.e., host modulus >> 200 GPa, thickness >> 0.2mm, or some combination of the two), the sensitivity will be too low to obtain accurate host modulus, which is illustrated by the constant yellow region in Figure 3-5a. To expand the sensitivity range to higher host moduli, a stiffer stiff sensor is required. The current configuration is suitable for measuring aluminum (75 GPa) and copper (110 GPa), whereas steel (200 GPa) may be at the upper limit of detectability. All three metals are included in the planned experiments.

Within the experimental range tested in this work (host thickness 2 mm - 3 mm and host modulus 70 GPa – 200 GPa), the average percent error is less than 4%. Within the total range studied in the FEM, the CS nonlinear mapping function from the pin force model has an average percent error of just under 9%. The error is very large for thin and compliant host structures for three reasons. One, the stiff sensor is too obtrusive and causes large bending such that the small angle approximation no longer holds in the pin force model. Two, the neutral axis has shifted significantly from the center of the host structure, so α is no longer adequate to correct for neutral axis shifting. Three, the pin force model does not account for strain lost through the thickness of the stiff sensor pad due to bending of the host structure. Therefore, the FEM reported CS ratio for any given moduli is seen to always be lower than the pin force model. The error is also seen to increase as the host thickness increases. This is because the dominant host deformation mode transitions from bending to shear and causes the piecewise linear assumption of axial displacements no longer match the nonlinear axial displacements seen in the FEM.

Output from the FEM, the axial displacements of the centerline nodes of the host from compliant to stiff sensor boundaries for two host thicknesses are plotted in solid lines in Figure 3-6. The same axial displacements of the centerline nodes output from the pin force model are plotted in dashed lines in Figure 3-6. The y-axis represents the through thickness location of the node, normalized to the host thickness, such that a location of 0 represents nodes at the compliant sensor location and a location of 1 represents nodes at the stiff sensor location. The x-axis is the axial displacement of each node. For small host

thicknesses – blue lines – bending dominates which is characterized by linear axial displacement. For large host thicknesses – red lines – shear dominates which is characterized by nonlinear axial displacements. It is noted that the portion of host shear strains in series with the compliant sensor is very small. This is expected as the compliant sensor is not stiff enough to resist host deformations. The pin force model may therefore be simplified to include a single shear spring, though that is not included in this work.

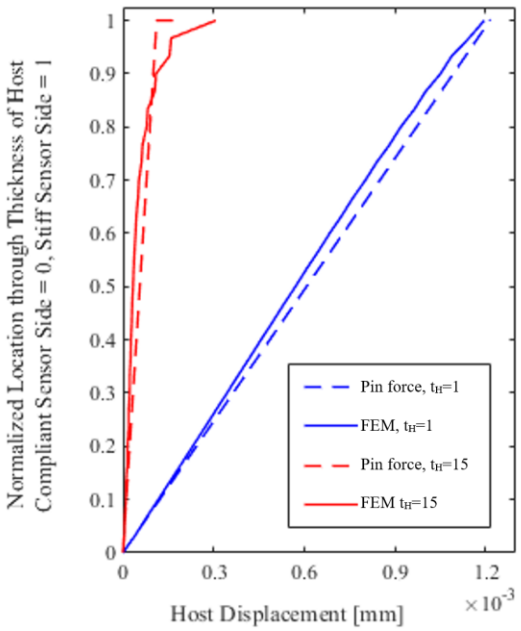

Figure 3-6. Axial displacement of the host plotted through the thickness of the host from compliant sensor to stiff sensor boundaries for two host thicknesses. The thickness is normalized such that both plots begin at 0 (compliant sensor location) and terminate at 1 (stiff sensor location). As the thickness increases, shear deformations begin to dominate evidenced by the nonlinear slope of the axial displacements.

The last step in verifying the accuracy of the pin force model is to recreate a stress-strain curve with evolving host moduli due to plasticity. In the FEM, the host material specified is copper with isotropic hardening and is strained until 0.005 strain. The expected strains from the individual sensors comprising the CS sensor are extracted from the FEM output and input into the pin force model. The estimated stress-strain curve from the modeled CS sensor as well as the stress-strain curve averaged from the host elements in the FEM

are plotted in Figure 3-7. The estimated stress-strain curve from the pin force model matches the FEM stress-strain curve well and captures the evolution of the host modulus as it experiences plastic deformations.

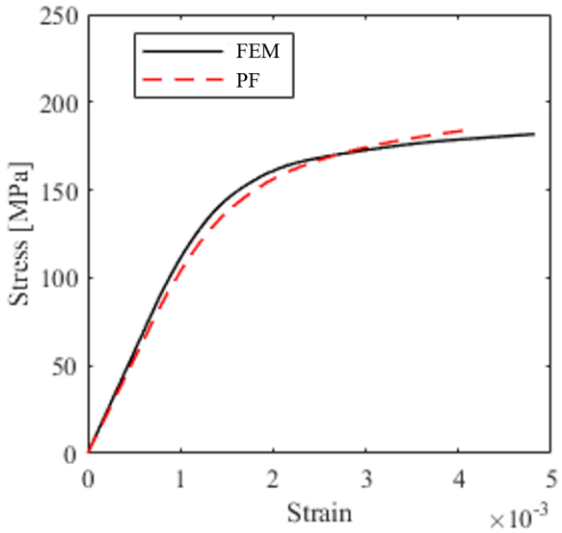

Figure 3-7. Stress-strain curves: the solid line is the stress-strain curve of copper input into the FEM and the dashed line is the stress-strain curve of copper recreated from FEM sensor strains input into the pin force model nonlinear mapping function.

The pin force model can also be used if the external loading is an applied moment. The pin force model with applied moment is shown in Figure 3-8. All variables in the pin force model remain the same as for the axial external load.

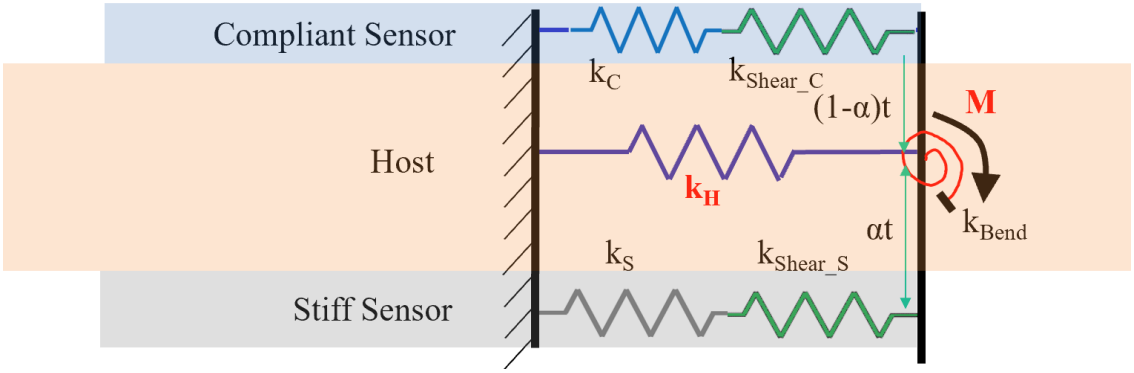

Figure 3-8. Pin force model overlaid on CS sensor and host assembly subject to external moment.

Solving the spring relationship from the pin force model in Figure 3-8 yields the host modulus in terms of the CS ratio and host and sensor geometries as

$$E_h = \frac{(E_c A_c - E_s A_s R)\left(\frac{1}{A_h} + \frac{2t\alpha(1-\alpha)(1+\nu)}{wL^2}\right)}{(1-\alpha)R-\alpha}. \quad \textit{Equation 11}$$

This again provides a monotonic nonlinear mapping function between CS ratio and host modulus. The CS nonlinear mapping function from $E_h = \frac{(E_c A_c - E_s A_s R)\left(\frac{1}{A_h} + \frac{2t\alpha(1-\alpha)(1+\nu)}{wL^2}\right)}{(1-\alpha)R-\alpha}$. Equation 11 is plotted in Figure 3-9. Pin force model nonlinear mapping function, CS ratio vs. host modulus vs. host thickness, showing the CS ratio, host modulus, and thickness parametrically varied. The color of the surface map corresponds to the value of the CS ratio. The gradient of the color, or how quickly the color changes, corresponds to the CS sensor's sensitivity. It is seen that the CS sensor is most sensitive when the stiffness of the host is low, either low modulus or low thickness. This agrees with the previous discussions of CS sensing both with the FEM and pin force model subject to axial load.

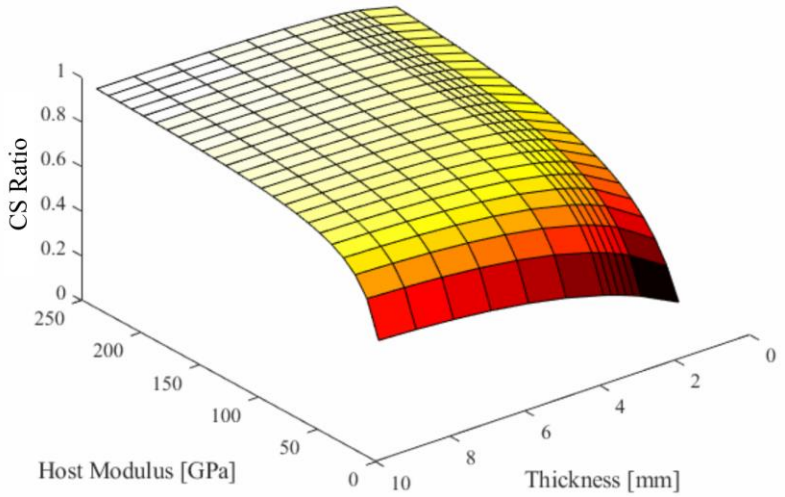

Figure 3-9. Pin force model nonlinear mapping function, CS ratio vs. host modulus vs. host thickness

To verify the pin force model with external moment, it was compared to a FEM with the host geometry expected for use in future experiments of dynamic beam fatigue. The FEM of the host beam (80 x 10 x 2.5 mm), shown in Figure 3-10, is again constructed in Abaqus using 3D block elements. The stiff sensor (10 x 8 x 0.2 mm) is modeled as a rectangular pad tie-constrained to the host imitating perfect bonding between sensor and host. The boundary conditions are encastre conditions on end of the host and a traction is applied at the free end, mimicking the experiments planned on a dynamic shaker table. The strains on top of the sensor pad are averaged and assumed to represent the strains measured by the stiff sensor in experiment. The compliant sensor is assumed to offer negligible resistance to the deformation of the host and is assumed to directly measure the strain on the host structure's surface. These strains are divided and then input into $E_h = \frac{(E_c A_c - E_s A_s R)\left(\frac{1}{A_h} + \frac{2t\alpha(1-\alpha)(1+\nu)}{wL^2}\right)}{(1-\alpha)R-\alpha}$. Equation 11 to estimate the elastic modulus of the host.

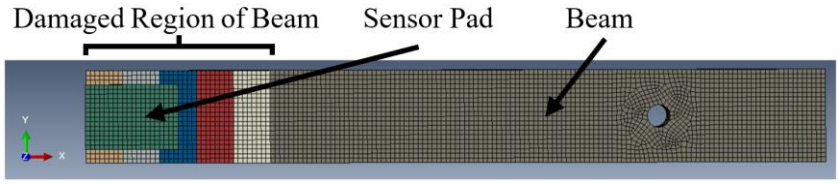

Figure 3-10. FEM of beam with CS sensor mounted on clamped end. The mesh and material properties are displayed.

For simple verification of the modulus estimate, the host thickness was held constant at 2.5 mm and the total host modulus was parametrically varied from 70 - 35 GPa in 7 GPa steps. The estimated modulus from the CS sensor transfer function is plotted versus the FEM defined modulus in Figure 3-11. The estimation from the pin force model always has error < 2.5% compared to the actual host modulus, which demonstrates that the pin

force model can accurately capture the dominant deformation mechanics and accurately predict host modulus under an external moment.

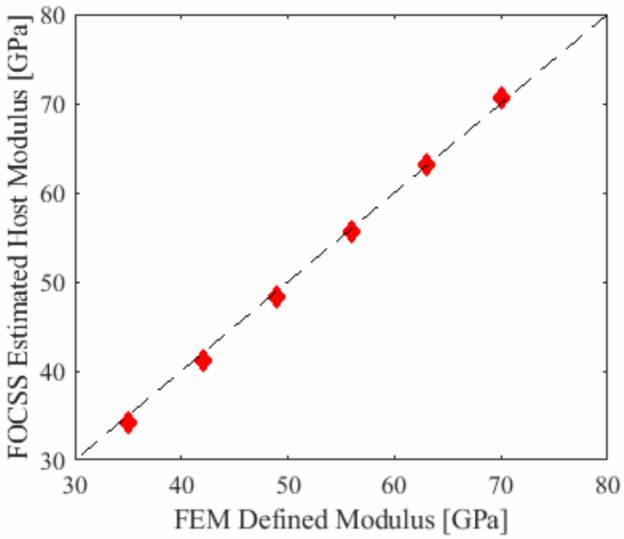

Figure 3-11. CS sensor estimated host modulus versus the host modulus input into the FEM model plotted as red diamonds. The dashed black line shows ideal one-to-one behavior.

To quantify the sensitivity of the CS sensor to fatigue damage, fatigue damage is modeled in the FEM as a decrease in pristine elastic modulus of either 10%, 20%, or 50% in the damaged region of the beam near the base of the cantilever. The length of the damaged section increases in 4mm steps up to 20mm from the clamped end, shown as the colored bands in Figure 3-10. The percent change in CS sensor estimated host modulus for each damage state is plotted as green circles in Figure 3-12 against the percent change in natural frequency. Natural frequency was chosen for comparison because it is also a commonly used damage precursor in SHM and is known to degrade during fatigue. The red diamonds are obtained from scenarios where the entire length of beam has a defined modulus with 10-50% degradation. The dashed black line represents a hypothetical limiting case where elastic modulus loss and natural frequency loss would be equal.

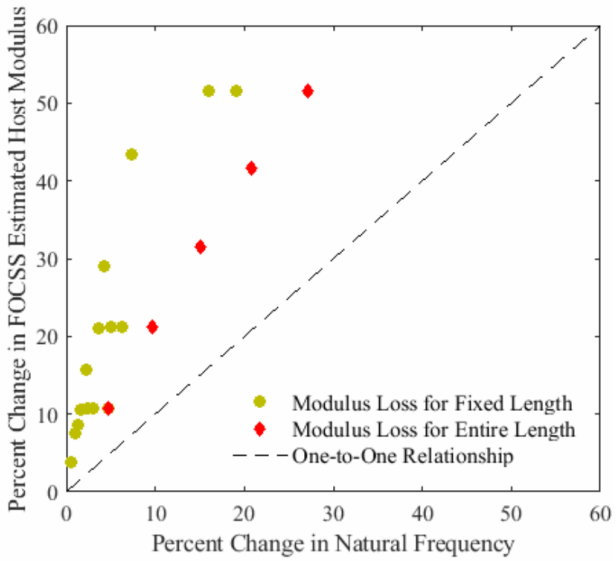

Figure 3-12. Percent change in pin force estimated modulus versus percent change in natural frequency for various damage states. Pin force model estimated elastic modulus is shown to be more sensitive than natural frequency to local damage.

The first takeaway is that the CS sensor estimated host modulus is more sensitive to fatigue damage than the natural frequency. Even in the cases where the entire beam has degraded modulus (red diamonds in Figure 3-12) the CS sensor estimated modulus is approximately twice as sensitive as natural frequency. This is explained easily as natural frequency has a square root dependence on elastic modulus in a uniform cantilever beam, so tracking the elastic modulus directly at a local point is much more sensitive. When the square root relation is considered, the predicted modulus from both the CS sensor and natural frequency are equal when the entire beam length has degraded modulus. However, the sensitivity from the CS sensor is heightened when damage is concentrated at the root of the beam near the sensor pad. For the degraded modulus states of varied length (green circles in Figure 3-12) the sensitivity of the CS sensor is 2.5 to 6 times the sensitivity of the natural frequency.

Note that the CS sensor shows increased sensitivity only when damage is located underneath the footprint of the CS sensor. This is evident in Figure 3-12 as each cluster of green circles levels off at the end of the sensor footprint. Natural frequency, on the other hand, has a more uniform and gradual decay as damage propagates. Fortunately, the CS sensor can measure modulus and natural frequency simultaneously, so once damage propagates through the sensor footprint and natural frequency begins to dominate in sensitivity, the CS sensor can switch to tracking natural frequency.

Even if the natural frequency was unknown, the region of maximum stress is usually known a priori in application – in the case of a cantilever beam, it is known the base of the beam nearest to the clamped region has highest stress – so the CS sensor can be intelligently placed to provide maximum sensitivity to damage as the modulus will always decrease quickest in the highest stress region. Examples of unknown natural frequency include vibrations under forced harmonic excitations or non-uniform broadband excitations as well as quasistatic fatigue.

3.2. Variational Model

The second model proposed for the CS sensor with opposite-sided, surface-mounted configuration is a variational model. It is expected that the variational model will provide a better estimate of the instantaneous host modulus than the pin force model, but comes at the cost of increased computation. Still, the computational cost of the variational model should be lower than the finite element model, so this model may prove a perfect blend of computational price and accuracy.

The variational model was developed with the goal of matching the planned tensile experiments with modified dog bone geometry. However, the structure was simplified to maintain constant geometry and material properties in each section. Also, the symmetry of the host structure was used to simplify the model. The model of the host and CS sensor assembly with three sections is shown in Figure 3-13.

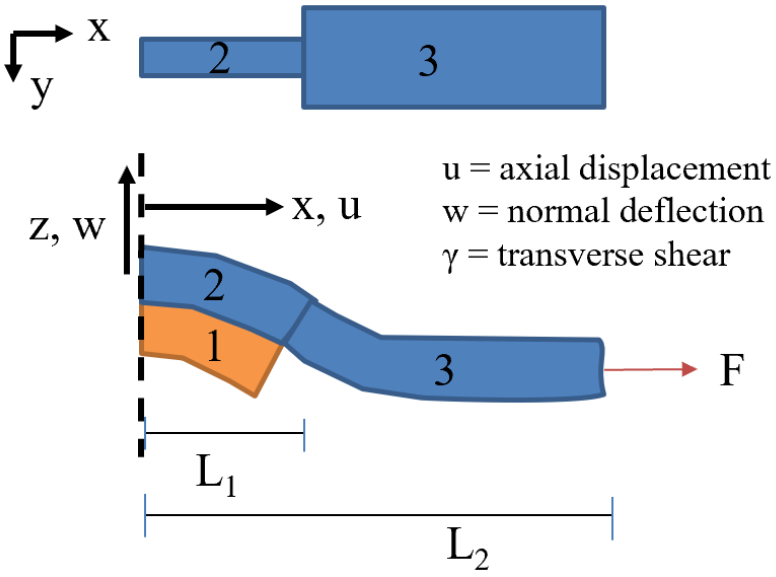

Figure 3-13. Deformed geometry of host structure and CS sensor assembly estimated by the variational model.

Then, individual shape functions were applied to each section. The shape function for displacement, *u*, is linear and has form

$$u_i = a_{i0} + a_{i1}x. \quad \textit{Equation 12}$$

The shape function for deflection, *w*, is cubic and has form

$$w_i = b_{i3}x^3 + b_{i2}x^2 + b_{i1}x + b_{i0}. \quad \textit{Equation 13}$$

It is assumed that the deflection of sections 1 and 2 are equal so only one shape function is used for both w_1 and w_2. The shape function for rotation from shear, γ, is quadratic and has form

$$\gamma_i = c_{i2}x^2 + c_{i1}x + c_{i0}. \text{ Equation 14}$$

In all shape functions, *i* denotes the three sections of the CS sensor and host assembly.

The applied boundary conditions mimic the planned experiments. The boundary conditions with corresponding constraint equations are listed below in Table 1.

@ x = 0	$u_1 = u_2 = 0$, $w_1' = 0$, $\gamma_1 = \gamma_2 = 0$
@ x = L_1	$\gamma_2 = \gamma_3$, $u_2 = u_3$, $w_2 = w_3$, $w'_2 = w'_3$
@ x = L_2	$w_3 = 0$, $w'_3 = 0$, $\gamma_3 = 0$

Table 1. Boundary condition constraints on variational model.

A displacement continuity constraint is also applied at the interface of sections 1 and 2. The constraint equation is

$$u_1 + 0.5t_1(-w_1' + \gamma_1) = u_2 - 0.5t_2(-w_2' + \gamma_2) \text{ Equation 15}$$

and must be satisfied for all values of *x* between 0 and L_1. Thus, this single equation creates two constraint equations (one for each power of x) that need to be satisfied.

The energy of the deformation is split into axial, bending, and shear portions. The axial energy is described by

$$\sum_{i=1}^{3} \int_{L_{oi}}^{L_{fi}} E_i A_i \left(\frac{du_1}{dx}\right)^2 dx, \quad \text{Equation 16}$$

where L_o is the initial x position, L_f is the final x position, E is modulus, A is cross-sectional area, u is displacement, and i denotes the section. The bending energy is described by

$$\sum_{i=1}^{3} \int_{L_{oi}}^{L_{fi}} E_i \boldsymbol{I_i} \left(\frac{d\left(-\frac{dw_1}{dx}+\gamma_1\right)}{dx} \right)^2 dx, \text{ Equation 17}$$

where I is moment of inertia and other variables are same as before. The shear energy is described by

$$\sum_{i=1}^{3} \int_{L_{oi}}^{L_{fi}} G_i A_i \left(\frac{d\gamma_i}{dx} \right)^2 dx, \quad \text{Equation 18}$$

where G is shear modulus and all other variables are the same as before.

If the strains from the stiff and compliant sensors are input as constraints and E_2 and E_3 are treated as unknown variables, then the system of equations becomes nonlinear. Therefore, E_2 and E_3 are treated as knowns and the solution cycles through possible values of E_2 and E_3 until the estimated stiff and compliant strains match what is measured by the CS sensor. The stiff and compliant sensor strains, ε_s and ε_c, respectively are described by

$$\varepsilon_s|_{x=0} = u_1' - (-w_1'' + \gamma_1')\frac{t_1}{2} \quad \text{Equation 19}$$

and

$$\varepsilon_c|_{x=0} = u_2' + (-w_1'' + \gamma_2')\frac{t_2}{2}. \quad \text{Equation 20}$$

If the CS sensor strains are no longer used as constraints, then an external excitation needs to be applied. This is done by adding an arbitrary axial force to the free end. The work done by the force, F, is described by

$F_{ext} u_3|_{x=L_2}$. *Equation 21*

Adding an arbitrary force works in this model because the model is constrained to the elastic regime of material properties. So as *F* is increased, the strains estimated by the stiff and compliant sensors simply linearly increase. Also, as the materials are constrained to the elastic regime, it is assumed the modulus of the host will be equal in all sections, thus E_2 is equal to E_3. In this way, the variational model provides a transfer function from host modulus to CS ratio. After developing the transfer function, it can be used in reverse, such that the CS ratio can estimate the host modulus. Then, to determine the external force, the strain magnitude is linearly related to force magnitude.

To verify the variational model, the CS sensor strains generated from the FEM are input into the variational transfer function and the estimated host modulus output. The percent error between the variational estimated host modulus and the actual host modulus input into the FEM is shown in Figure 3-14. The error from the variational model is roughly constant at 20%. When the host structure gets very thin, then the error is seen to drastically increase.

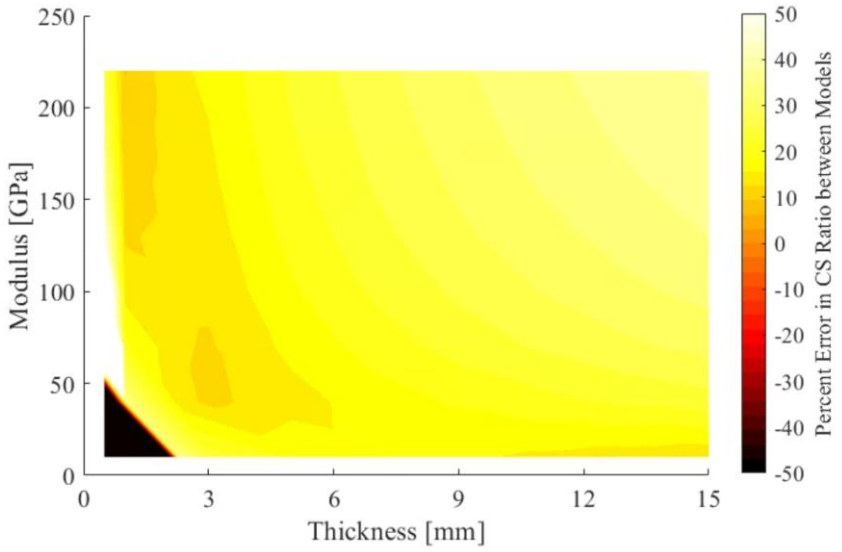

Figure 3-14. Percent error in variational model estimated host modulus from CS ratio versus input FEM host modulus and output CS sensor strains.

The pin force model displays much better accuracy than the variational model. This is due to the tailorable term, α, in the pin force model that accounts for some of the shift of the neutral axis. In the variational model, the neutral axis is held constant. Future work should focus on incorporating the neutral axis shift into the variational model. Still, as the error from the model is roughly constant, the current variational approach can be utilized to accurately predict changes in host modulus.

For further verification of the variational model, the shape functions along the top and bottom length of the host are compared to the shape functions generated by the FEM. The shape functions are shown in Figure 3-15. The estimated displacement of the host structure from the variational model underpredicts the displacement specified by the FEM. This is due to the reduced modulus estimated by the variational model. Similarly, the estimated deflection from the variational model is lower than the deflection specified by FEM.

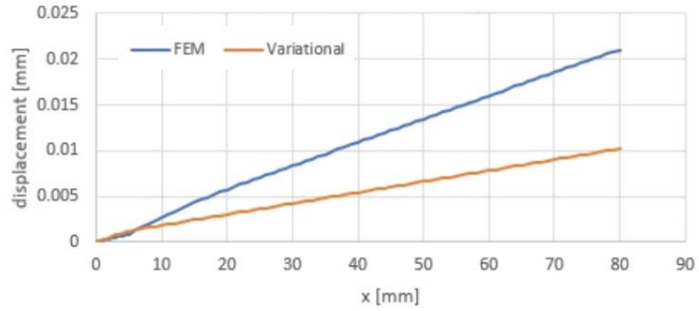

(a)

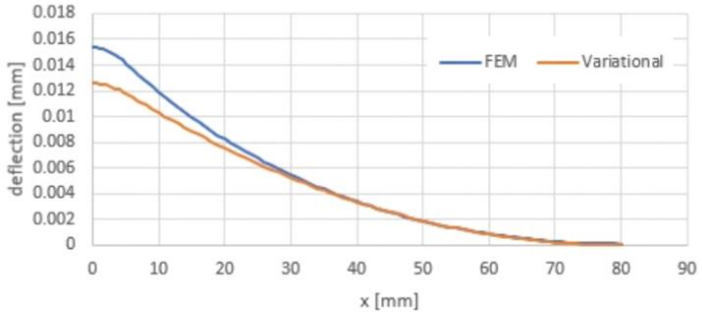

(b)

Figure 3-15. Shape functions estimated by the variational model compared to the shape functions specified by the FEM for (a) displacement and (b) deflection along the length of the host.

Lastly, the displacement of the host through its thickness at L_1 is plotted in Figure 3-16. Again, the through thickness displacement estimated from the variational model underpredicts the true displacements specified by FEM. Also, the variational model does not display any nonlinearity in the displacements. When minimizing the energy of the system, the higher order terms in deflection and shear rotation become zero. This is subject to further study.

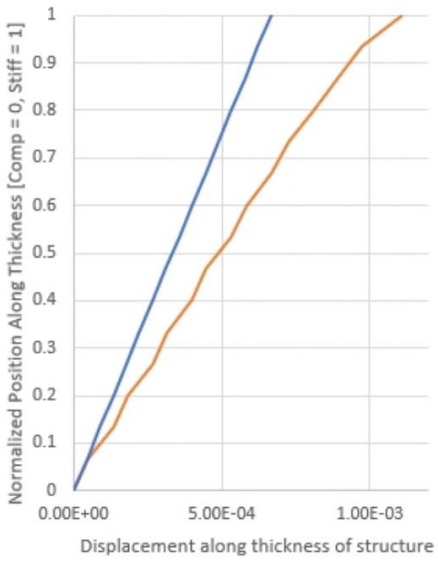

Figure 3-16. Through thickness displacements of the host at $x=L_1$ as reported by the FEM (orange) and as estimated from the variational model (blue). The host thickness is 2.29mm and modulus is 70 GPa.

3.3. Summary of Modeling

The FEM is the most accurate model and therefore was used in the parametric design study presented in Chapter 2; however it is computationally expensive and time consuming. In this chapter, Chapter 3, two analytic models were developed to supplement the FEM.

The first model is a pin force model which provides a closed form solution of host modulus given the CS sensor ratio. The pin force model also contains an application specific tailorable term, α, that reduces the error between pin force model and FEM. When α is tailored, the pin force model can generate reasonable approximations of host modulus, with an error under 4% in the range of this study's planned experiments. The second model is a variational model, which proved less accurate than the tailored pin force model. It is expected that with further improvement, namely incorporating the shift

in neutral axis into the variational model, the variational model can offer better accuracy than the pin force model. However, that is subject to future work and not included in this study.

In Chapter 4, which details experiments with the CS sensor, the pin force model is used to convert the CS sensor strains to the stress-strain state of the host structure.

4. Experimental Validation

In this chapter, the opposite-sided, surface-mounted CS sensor is used to monitor the full stress-strain history of a host structure subject to monotonic and cyclic tensile loading. Past experiments with a CS sensor have been limited to mostly elastic modulus measurement; one report has CS sensing of plastic deformations in aluminum, however only nondimensionalized values were reported.

As stated previously, the resistive copper foil strain gauges are paired with fiber optic sensors because of their well-documented benefits in application. Currently all testing is benchtop testing, but once the CS sensors are taken to industry, it may prove convenient to already have included fiber optic sensing elements.

4.1. Sensor Fabrication

To fabricate the ‘traditional’ CS sensor, the stiff sensor is constructed by bonding a steel shim patch (dimensions 10 x 8 x 0.2 mm) directly to the host structure. Then a resistive copper foil is bonded to the steel patch. The compliant sensor is constructed by bonding

the resistive copper foil directly to the host structure. To fabricate the fiber optic CS sensor, the stiff sensor is again constructed by bonding a steel shim directly to the host structure. Then a fiber Bragg grating (FBG) is bonded to the steel patch. The compliant sensor is constructed by bonding a Fabry-Perot interferometer (FPI) directly to the host structure. The FPI is fabricated "in-house" by aligning two optical fiber end faces within a 3D printed polymer tube, schematically shown in Figure 4-1. The 3D print polymer, IP-S, has a nominal stiffness 3 GPa [76] and is printed using a Nanoscribe© printer.

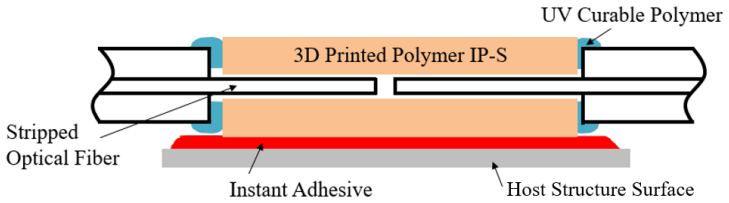

Figure 4-1. Schematic of "in-house" fabricated FPI including 3D printed capillary.

In both CS sensors, the steel patch offers dual utility: (i) it augments the mechanical stiffnesses of the stiff sensor and (ii) it provides a consistent bonding platform between tests. When manually gluing the FBGs directly to the structure, bond layer inconsistencies can greatly alter the stiffnesses of the individual sensors, thus compromising accuracy and repeatability of the CS sensor. The steel shim patch is bonded to the three metals using different bonding agents. In the aluminum coupons, the steel pad is glued to the host via DP460NS© adhesive. In the copper coupons, the steel pad is soldered to the host with SAC305 solder. In the steel coupons, the steel pad is spot welded to the host structure. These bonds are shown in Figure 4-2. Traditional copper foil gauges were placed next to the fiber optic sensors on the same pad to verify the fiber optic sensor performance.

Figure 4-2. Stiff sensor of the CS sensor bonded to (a) aluminum with glue, (b) copper with SAC305 solder, and (c) steel with spot welds. On each stiff sensor pad is an FBG on the right and resistive copper foil strain gauge on the left.

The CS sensor is surface mounted on reverse sides of testing coupons with modified dog bone geometry. The modified dog bone geometry is chosen to ensure that failure site of each coupon is localized near the CS sensor

location, while also maintaining primarily uniaxial strain fields.

(a)

(b)

Figure 4-3a shows a copper coupon from the front where the stiff sensor is bonded.
(a)

(b)

Figure 4-3b shows a copper coupon from the back where the compliant sensor is bonded.

(a)

(b)

Figure 4-3. Traditional and fiber optic CS sensor surface-mounted on a copper coupon with modified dog-bone geometry. (a) front view showing stiff sensor and (b) back view showing compliant sensor.

In all tests, the coupons are loaded with a force controlled mechanical testing system (MTS). The MTS provides measures of end displacement and applied load for verification of the CS sensor output. The resistive copper foil gauges are recorded with a National Instruments© SCXI-1520 data acquisition system featuring strain gauge conditioning. To record the strain from each fiber optic sensor, the optical spectrum of each fiber optic sensor was measured alternatingly with an optical spectrum analyzer. This method output an intensity versus wavelength array for each fiber optic sensor

approximately every second. Then, from the spectra, the strain is calculated in post-processing. Strain from the FBG, ε_s, in microstrain is calculated by measuring the wavelength shift of the spectrum peak via

$$\varepsilon_s = 1200\left(\lambda^i - \lambda^1\right), \textit{ Equation 22}$$

where λ specifies the wavelength of maximum intensity in nanometers and the superscript, *i*, indicates the time. Strain from the FPI, ε_c, is calculated using 1-peak tracing, which assigns a constant slope from an original two peak tracing method, then tracks a single peak as it shifts in the spectrum [77]. Strain from the FPI, ε_c, in microstrain is calculated from

$$\varepsilon_c = 333.3\ m\left(\lambda_1^i - \lambda_1^1\right), \textit{ Equation 23}$$

here λ specifies the wavelengths in nanometers of local intensity peaks, the subscript indicates the wavelength being tracked, and the superscript, *i*, indicates time. The slope, *m*, is calculated from the first spectrum using two peak tracing [78] via

$$m = \frac{\lambda_2^1}{2000\left(\lambda_2^1 - \lambda_1^1\right)}. \textit{ Equation 24}$$

In this work, the spectral arrays are post-processed after test completion to yield CS sensor strain measurements. However, real-time dynamic measurement is possible with a more sophisticated optical interrogator [79].

4.2. Monotonic Tensile Tests

In monotonic tensile testing, the coupons are loaded in an MTS with a constant loading rate of 10 N/s until the compliant sensor records ~0.005 strain, the maximum strain measurable by the National Instruments© data acquisition system. The test matrix

includes two tests with each material: aluminum, copper, and steel. One test has both fiber optic and traditional copper foil strain gauges. The second test has only the traditional copper foil gauges. Therefore, for each material three measurements from CS sensing are generated: two from traditional CS sensors and one from the CS sensor.

Smoothing was performed on the strain data obtained from all sensors to reduce noise. Within the elastic range of each material, a linear fit was applied to the strains. Then, at the onset of plasticity, a two-term exponential curve was used to fit to the strain data. Smoothing is necessary. In the loading experiments, the initial strains were quite low, resulting in large errors in the ratios measured at the beginning of the test. Additionally, the errors in sensor response could be amplified by the CS nonlinear mapping function throughout the duration of the test. In both cases, smoothing can help reduce the errors. The current smoothing process is successful because the load history on the host structure is known. In a real-world application, when the loading history is unknown, the smoothing must use a more generic method.

The smoothed strain responses are used to obtain the CS ratio, which is plotted in Figure 4-4. The stress-strain curve generated with the MTS load cell and compliant sensor strain is also plotted. Recall from $E_H = \left(\left(\frac{t^2}{I_H} + \frac{2t(1+\upsilon)}{w_H L_1^2}\right) A_S \alpha\right) * E_S \frac{R}{1-R}$. Equation 9 that the ratio between the stiff and compliant sensor strains has a monotonic relation to the instantaneous tangent modulus. Therefore, the CS ratio is expected to be constant in the elastic regime (constant slope in host stress-strain curve) and then decrease as the host experiences plasticity (decreasing slope in host stress-strain curve).

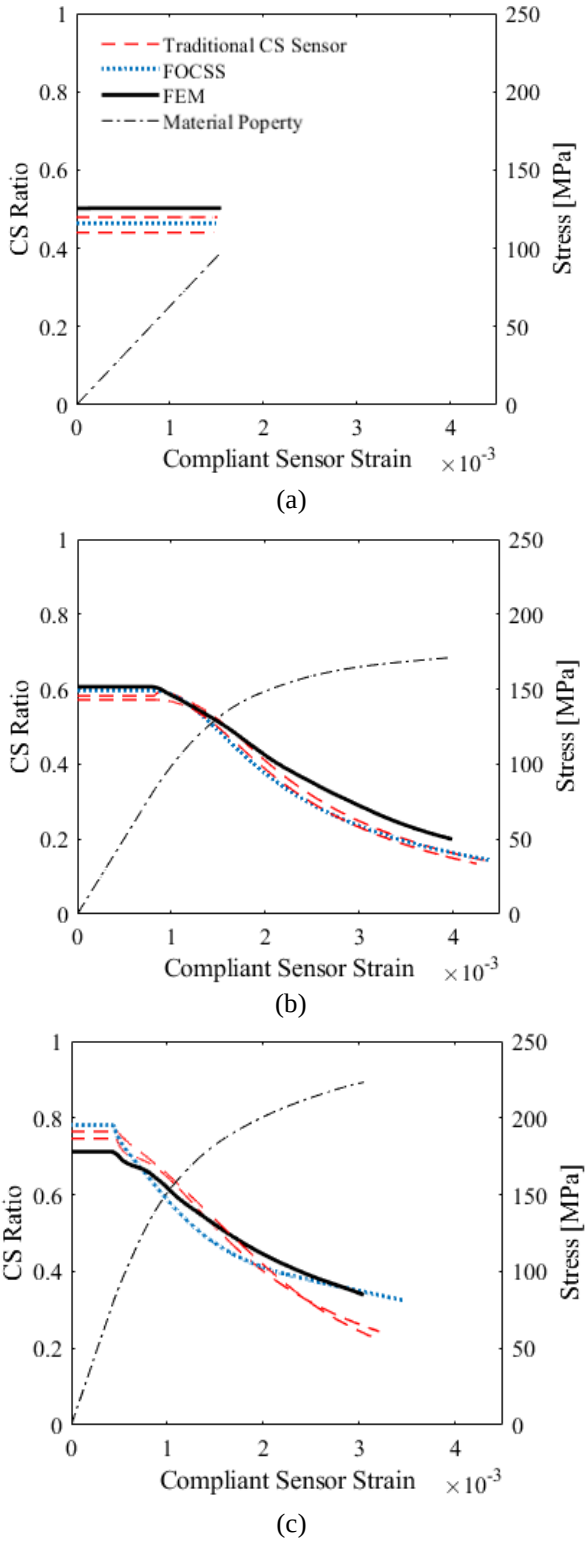

Figure 4-4. The CS ratio versus the compliant sensor strain (left y-axis) and the MTS stress versus the compliant sensor strain (right y-axis) obtained for three types of test coupons: (a) aluminum, (b) copper, and (c) steel. The solid black line represents the FEM predicted CS ratio, the two dashed red lines represent the traditional copper foil strain gauge CS sensor response in two tests, the dotted blue line represents the FOCSS response in one test, and the dash dotted black line represents the stress-strain curve obtained from the MTS (right y-axis).

In Figure 4-4, since the aluminum coupon does not reach plasticity, only the initial portion of the test is included. Also, because no plasticity is experienced the CS ratio remains flat denoting constant tangent modulus. In Figure 4-4b and Figure 4-4c, the copper and steel coupons experience plasticity and the CS ratio is seen to drop as the tangent modulus decreases. Furthermore, it should be noted that the CS ratio is lowest for aluminum and highest for steel, which is consistent with the known material stiffness properties of each material.

These results indicate that the CS ratio can be used as a quickly obtained single measure of the health of the structure, which promises its future application in PHM machine learning algorithms. Additionally, consistency between sensor designs and applications is no longer required as the normalized change in CS ratio can itself provide useful information about the health of the host structure; instead of generating absolute values of host modulus from the CS ratio, which can be affected by CS sensor fabrication inconsistencies and bonding defects, one can simply acknowledge that damage is accumulating as the CS ratio decreases. However, further work is necessary to generate a threshold value for critical damage accumulation given percent change in CS ratio.

The CS ratio is next converted to host modulus using the pin force model. For now, the term, α, in the pin force model is held constant at 0.33, which was determined to render the best performance in elastic modulus prediction. In future work, this term can be iteratively updated as the instantaneous modulus of the host changes. For example, the initial value of α can be set as 0.5, which can be used to predict a host modulus based on

the lumped element spring model. As the host deformation progresses, the new neutral axis location (value of α) can be determined, and the process can be repeated until α does not change.

In Figure 4-5, the predicted moduli are compared with the actual moduli for the various CS sensors tested. The predicted modulus matches well for the aluminum and copper metals. The predicted steel modulus exhibits larger variance and more mismatch with the true host modulus value than the predicted moduli for aluminum and copper. This is because the steel modulus is in the upper threshold of the sensing range for this particular surface-mounted CS sensor design, resulting in large errors in the CS sensor output.

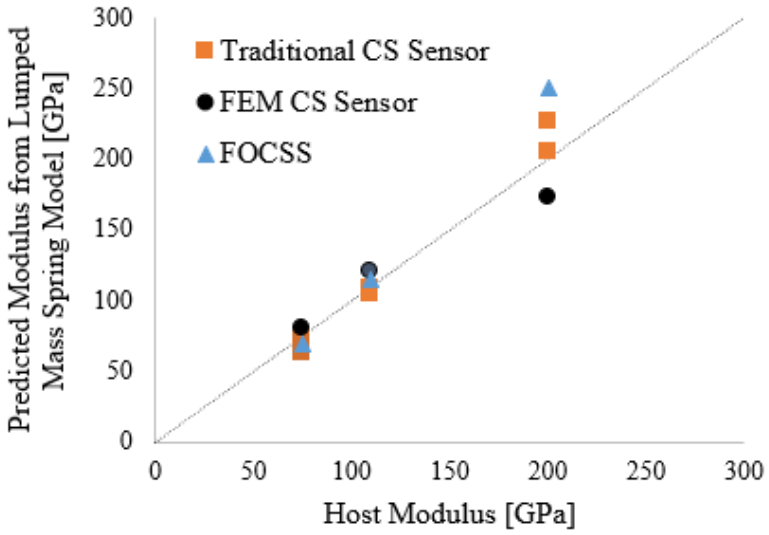

Figure 4-5. The predicted moduli of each metal from the lumped element spring model with various source inputs. The orange squares represent the results predicted with the lumped element spring model with input strains reported by CS sensor with traditional copper foil strain gauges. The blue triangles represent the results predicted with the lumped element spring model with input strains reported by the FOCSS. The dashed horizontal line corresponds with the stiffness of the stiff sensor in the CS sensor pair; the stiffness of the stiff sensor determines the threshold of accurate host modulus prediction, which corresponds with the dashed vertical line.

The next measure of the CS sensor performance is recreating the stress-strain curve of the metals under test. The traditional CS sensor strains and fiber optic CS sensor strains are

input into the pin force model nonlinear mapping function to generate the stress-strain curves. Again, the term, α, is held constant. Figure 4-6 plots the recreated stress-strain curve from each CS sensor as well as the independently measured host stress-strain curve from the MTS. Good agreement is seen in all three tests, with R^2 greater than 0.98.

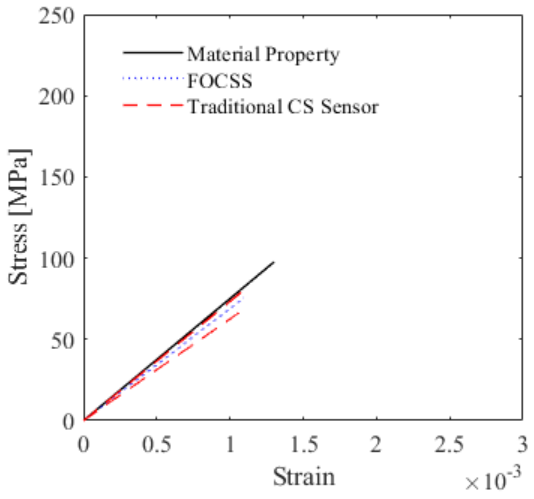

(a)

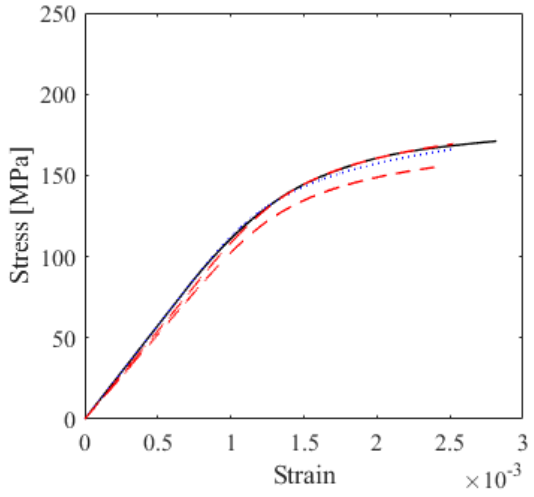

(b)

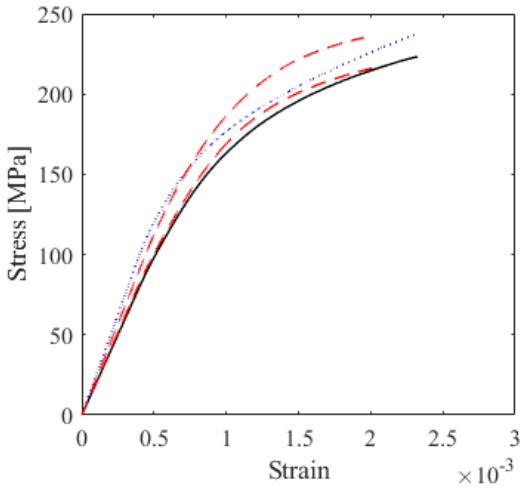

(c)

Figure 4-6. The recreated stress-strain curves (colored lines) from inputting experimental data into the nonlinear mapping function compared with the independently measured host stress-strain curve (solid black curve) for three different materials: (a) aluminum, (b) copper, and (c) steel. Red dashed lines and blue dotted lines represent results obtained with the CS sensors with traditional copper foil strain gauges and the FOCSS, respectively.

Both the CS sensor and traditional CS sensor exhibit good performance in predicting the stress-strain curve. Note that a much better fit can be achieved by tailoring α in the CS nonlinear mapping function to the specific applications. Considering the different bonding used for each host material as well as the thickness variations of the dog bone coupons, a tailored α may render a better fit. However, this is deemed unnecessary in this work, evidenced by the current high-quality results.

4.3. Cyclic Tensile Tests

Fatigue damage is introduced to eight AISI 1010 steel beams via force-controlled cyclic tensile loading performed with a mechanical testing system (MTS). The steel beams have the modified dog bone geometry seen in

(a)

(b)

Figure 4-3 where the width is tapered along the length becoming shortest in the middle. The CS sensors are surface mounted in the narrowest region. The tapered geometry was used to ensure the failure site was near the CS sensor while also maintaining primarily uniaxial loads. Three beams are fatigued at 84% of σ_{ult} (the ultimate strength of the steel), three beams are fatigued at 87% of σ_{ult}, and two beams are fatigued at 90% of σ_{ult}. All tests are completed with a loading rate of 10 Hz and R = 0.05, ensuring the loads remain tensile. The resistive copper foil strain gauges are used in all eight tests. The fiber optic strain gauges are used concurrently with the resistive copper foil strain gauges in three of

the eight tests – one test at 84% of σ_{ult} and two tests at 87% of σ_{ult}. This information is represented in the test matrix in Table 2.

Specimen #	Max Load [% σ_{ult}]	Fiber Optic Sensor [Y/N]	Cycle CS sensor is surface mounted
1	84	No	0
2	84	No	0
3	84	Yes	1
4	87	No	0
5	87	Yes	1
6	87	Yes	1
7	90	No	0
8	90	No	1

Table 2. Test matrix denoting specimen number, load level, and whether fiber optic sensors were used. All tests were completed using an MTS with loading rate 10Hz and R=0.05.

Tests involving the fiber optic strain gauges include a cycle with a much slower loading rate at predetermined intervals. These slow cycles allow for the collection of the fiber optic strain data, which with the current data acquisition system can only be recorded at 1Hz. Quicker data acquisition units are under development [79] but were not used in this study. In test 3, the slow cycle was performed every 10k cycles. In tests 5 and 6, the slow cycle was performed every 2k cycles. The loading rate of the slow cycle was 0.1 kN/s which equates to cycles of approximately 160s and 170s in the respective tests.

Also in Table 2, the far-right column denotes when the CS sensor was attached to the host structure. In four of the tests, the CS sensor was attached before any plastic strains were accumulated. In the other four tests, the CS sensor was attached after the first cycle was completed where significant plastic strains accumulate. The reasoning for this was to determine how the CS sensor would react in different applications. Attaching the CS sensor at the beginning of the test represents an application where it is considered in the

design phase of the structural build and will gather health estimates throughout the life of a structure. When attached at the beginning of the test, the CS sensor will have to accommodate the large plastic strains and be resilient enough to survive longer than the host structure. Attaching the CS after completion of the first cycle represents attaching the CS sensor retroactively to a host structure under investigation. Here the CS sensor should easily outlast the host structure, but may prove less sensitive as it will not see the initial damage accumulation.

Representative strains measured by the resistive foil strain gauges comprising the individual compliant and stiff sensors are shown in Figure 4-7a. As expected, the strains measured by the compliant sensor are larger than the strains measured by the stiff sensor. Also, the strains fluctuate at the loading rate of 10 Hz. To visualize the strains throughout the test, the maximum and minimum strain values during a 10-cycle window are determined and plotted in Figure 4-7b.

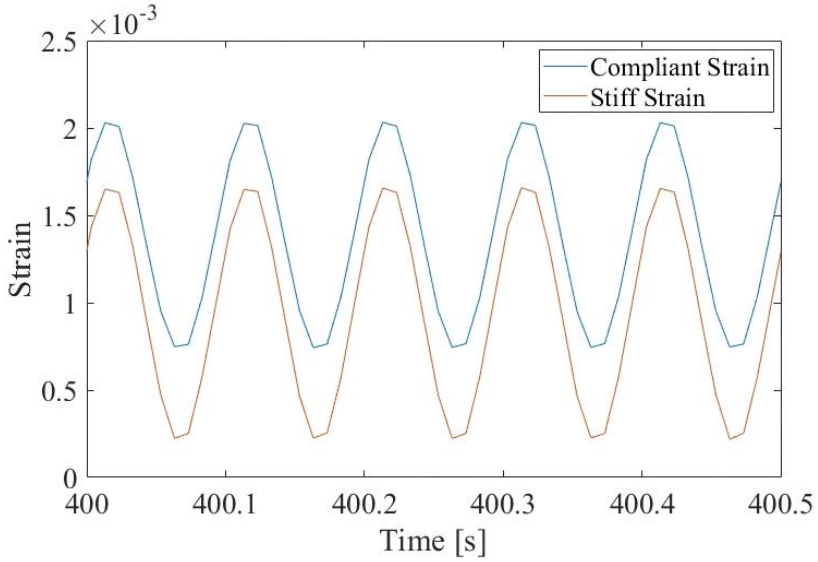

(a)

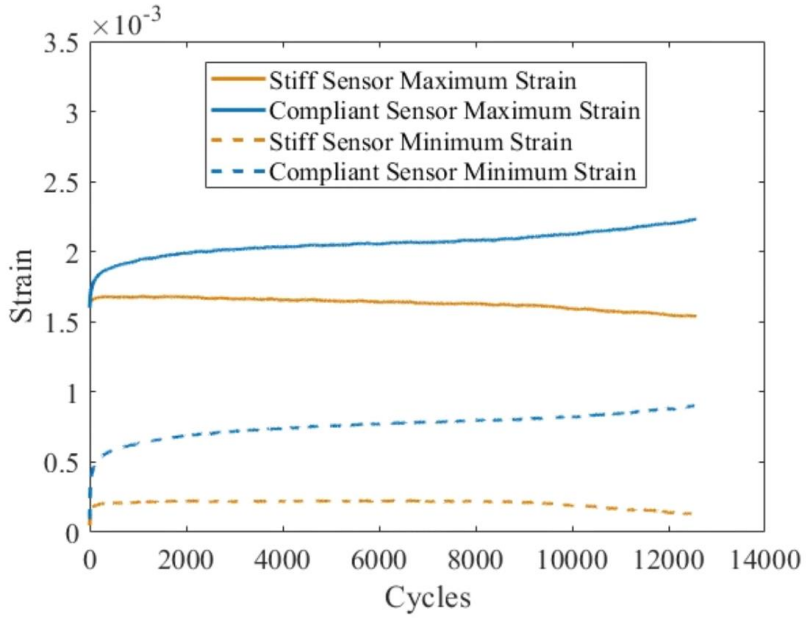

(b)

Figure 4-7. The individual CS sensors' strains during a representative fatigue test. (a) a sample of the compliant and stiff sensor strain history and (b) the full-time history of the 10-cycle window maximum compliant and stiff strains.

Figure 4-8 shows the 10-cycle window maximums and minimums of the end displacement and applied force reported from the load frame sensors. Recall that in CS sensing, the compliant sensor acts like an extensometer and the stiff sensor acts like a load cell. Comparing Figure 4-7b to Figure 4-8, it is evident that when the end displacement grows rapidly, so does the compliant sensor strain. Also at this point, it is evident the stiff sensor strain decreases whereas the load remains constant. The dissimilar behavior between the stiff sensor and force occurs because the stiff sensor is placed in parallel with the host whereas a typical load cell in a mechanical test system is placed in series with the host. When converting the individual CS sensor strains to the stress-strain state of the host, the effect of the placement of the stiff sensor is accounted for in the pin-force model, so the dissimilar behavior between stiff sensor and load is not concerning.

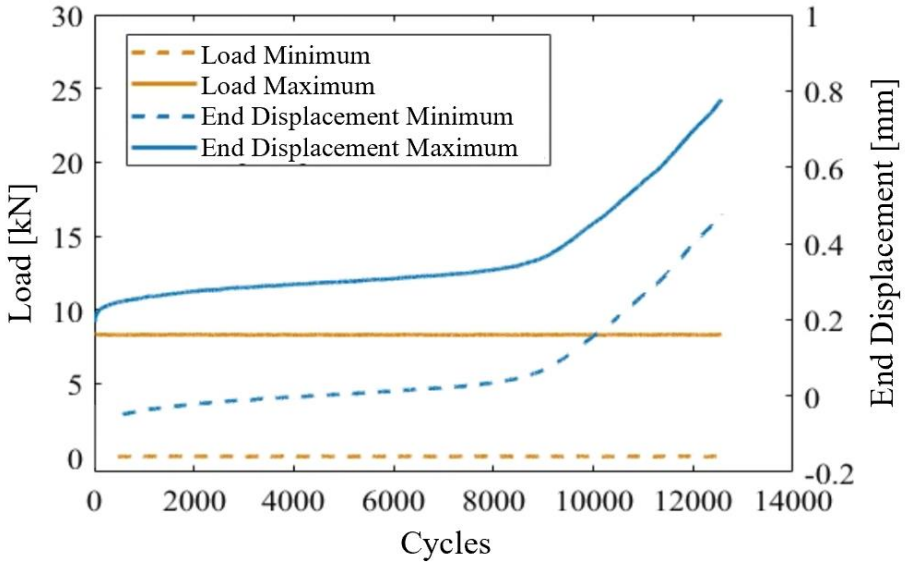

Figure 4-8. The full-time history of the 10-cycle window maximum MTS reported grip displacement and applied force during a representative fatigue test.

Steel accumulates damage in a ductile fashion, evidenced by the large end displacements seen in Figure 4-8, before any cracks are observed in the structure. The large plastic zones in a steel beam after removal from the load frame can be seen in Figure 4-9. Even though the narrowest section of the beam is where the CS sensor is mounted, the ductile failure sites are witnessed on either end of the CS sensor. The location of the failure sites is due to the local strengthening provided by the stiff sensor, i.e. the spot-welded steel patch.

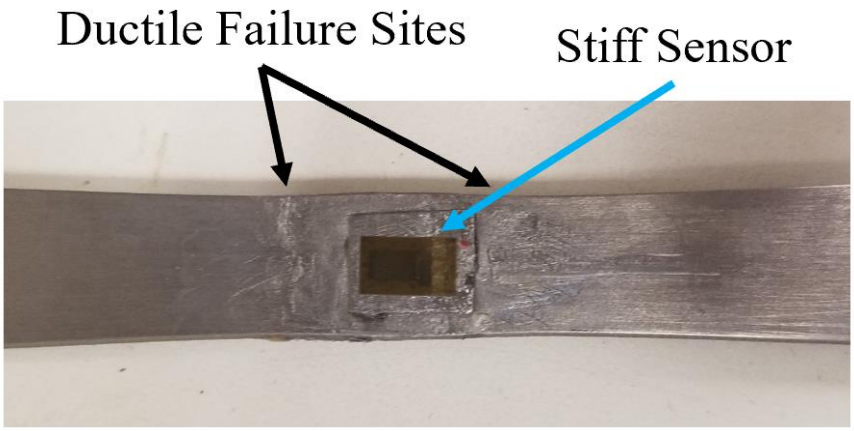

Figure 4-9. Failed coupon after removal from MTS. Clear necking is seen on either end of the CS sensor.

Because of this ductile damage accumulation, an automated criterion for the damage onset (CDO) is generated to specify when the steel had transitioned from a healthy state (supporting the applied load with small plastic strain accumulation) to an unhealthy state (supporting the load but with large plastic strain accumulating).

As schematically shown in Figure 4-10 the CDO is based on the departure of the maximum end displacement from a linear fit determined during the steady state region of the test. The solid blue line in Figure 4-10 is the maximum end displacement measured directly by the test frame. The solid black line is the linear fit generated using end displacement data in the initial steady state region. The green normal distribution was computed from the same data as the linear fit. The inset in Figure 4-10shows the variability in the maximum end displacement data. Then, the dashed black line represents the projected linear fit as the test continues. The CDO is triggered when the maximum end displacement exceeds two standard deviations from the expected value provided by the linear fit. The vertical red line partially hidden by the inset in Figure 4-10 indicates when the CDO is triggered.

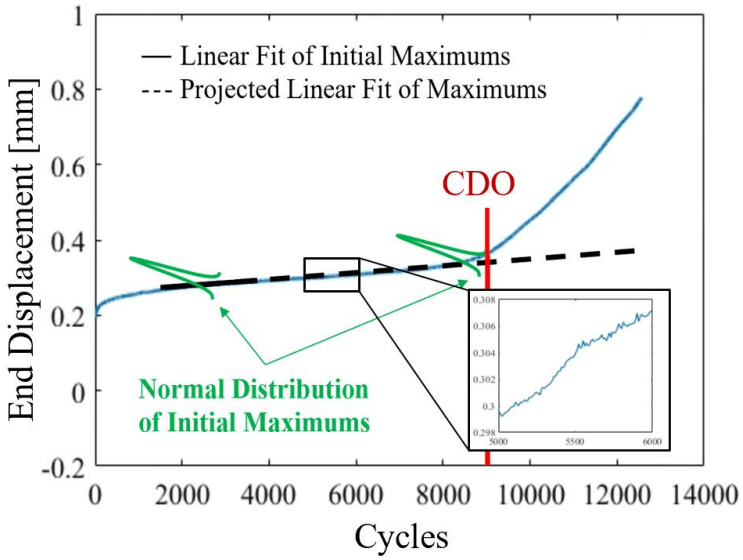

Figure 4-10. Displacement criterion for damage onset (CDO) in AISI 1010 steel. CDO specified when the plastic strain accumulation rate dramatically increases.

To check the CDO, the cycle at which the CDO is triggered is plotted against the nominal engineering stress amplitude for all eight tests in Figure 4-11. Fatigue data inherently has significant stochastic variability, and this is reflected with an early failure during one test loaded at 84% of σ_{ult}. However, the trend of the data agrees well and can be reasonably fit with a power-law model of the form

$$\Delta\sigma = \sigma_f'(2N_f)^c \text{ , Equation 25}$$

where $\Delta\sigma$ is the cyclic strain amplitude, N_f is the number of cycles to failure at the applied strain amplitude, and σ_f' and c are model constants unique to each material and fit with empirical data. A least squares fit provides values for σ_f' and c of 332.7 and -0.0154, respectively, with an R^2 of 0.90. Traditional stress amplitude versus number of cycles to fracture curves are also well fit with a power-law model, which indicates the CDO used in this study is acceptable and consistent across the eight tests.

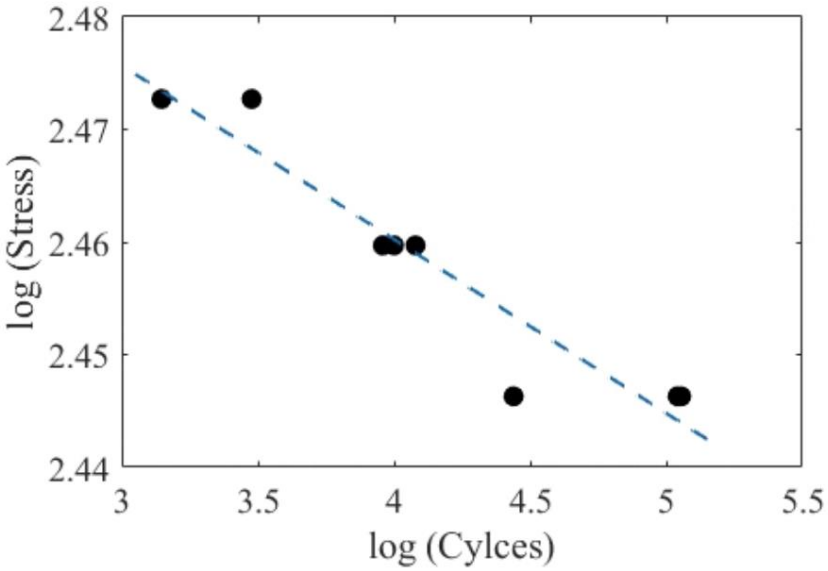

Figure 4-11. S-N curve for AISI 1015 steel using the discussed CDO and FEM generated strains at the failure site.

The results from the CS sensors are split into two categories. First the CS sensor ratio is evaluated for monitoring fatigue damage when loading is at 10Hz. This evaluation will only include the 'traditional' resistive copper foil CS sensors. Then, the CS sensor is evaluated for full hysteresis recreation during the slow cycles within three tests. This evaluation will include both the 'traditional' and fiber optic CS sensors.

4.3.1. 10Hz loading – Resistive copper foil CS sensor only

Recall that in CS sensing, the ratio of stiff to compliant sensor strains, R, has a direct relation to host stiffness. Therefore, the trend of R contains direct information about a structure's state of health. This structural health monitoring technique is especially appealing due to the low computational cost associated with tracking a single data input.

In order to smooth the measure of *R*, a fast Fourier transform (FFT) of the raw strain data from the stiff and compliant sensors is taken every 10 cycles. The amplitudes of the stiff

and complaint strain FFTs at 10 Hz (corresponding to the loading frequency) are divided to generate the CS ratio, *R*. The MTS stiffness index is generated similarly, though instead of compliant and stiff strains, it uses the end displacement and applied force measured by the load frame. The change in CS ratio is plotted with the change in stiffness for a representative test in Figure 4-12. The cycles have been normalized by the CDO such that life consumed is equal to unity at the time the CDO is triggered.

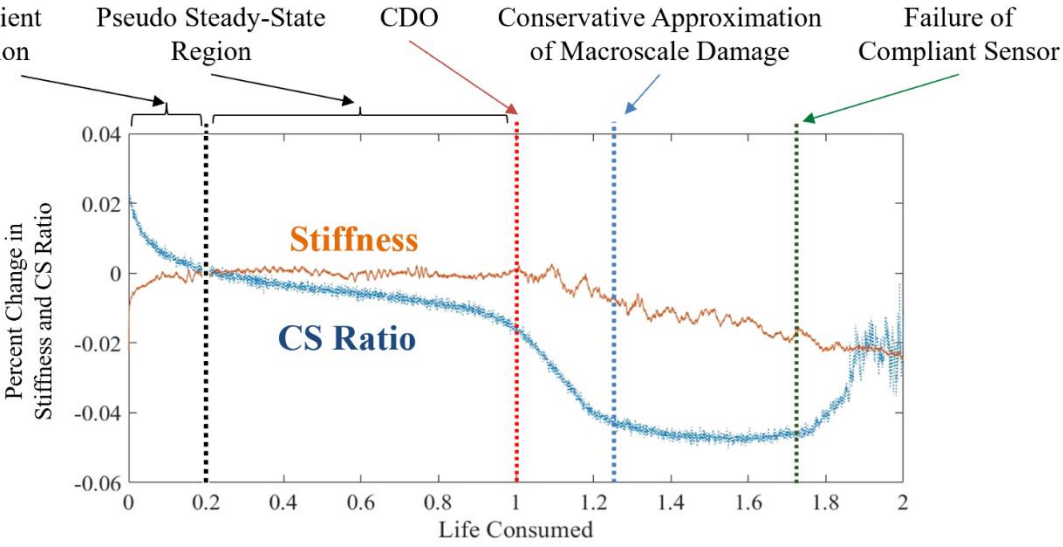

o and MTS stiffness with time during a representative fatigue test. At the time of ductile failure, both decrease significantly denoting a loss of stiffness.

The initial portion of the test, from 0 to 0.2 life consumed, is considered a transient region as the stiffness and CS ratio both rapidly trend towards a steady-state behavior. The transient initial region is common in fatigue loading behavior and will not be discussed for the rest of the study [80]. After the transient phase, the stiffness stabilizes and a 'pseudo steady-state' region is observed. Within the 'pseudo steady-state' region, the CS ratio constantly decreases. The decrease in CS ratio is due to the CS sensor itself

accumulating damage in the spotwelds and therefore measuring lower strain with the stiff sensor as the test progresses.

At the time the CDO is triggered, both the stiffness and CS ratio display a discernable decrease. The CS ratio decreases more than the stiffness, which is due to the local gauge-zone of the CS ratio versus the averaged global response provided by the load cell and end displacement reported by the load frame. Then, once the failure zone localizes away from the CS sensor, the CS ratio plateaus whereas the stiffness continues to decrease. The difference in behavior between CS ratio and stiffness is again due to the local measuring footprint of the CS sensor versus the average response provided by the MTS. At the time at which the CS ratio plateaus, no observable macroscale damage is present in the host structure, i.e. no cracks are witnessed; however because the failure site has localized away from the CS sensor, the CS sensor is no longer sensitive to further damage accumulation. Thus, the point at which the CS ratio plateaus is considered a conservative estimate of the onset of macroscale damage. In all tests, the earliest coalescing of the failure site away from the CS sensor occurred at 1.25 consumed life, shown in Figure 4-12, so 1.25 consumed life is chosen as the conservative estimate of macroscale damage.

As the test continues, the CS ratio increases around 1.7 consumed life as shown in Figure 4-12. The increase in CS ratio is due to failure of the compliant strain gauge. The copper trace is beginning to develop cracks producing incorrect strain measurements. However, by this point the CS sensor has survived almost twice the number of cycles needed to trigger the CDO, showcasing its durability.

The region of interest in the representative response of the CS sensor occurs from 0.2 consumed life (after the transient region is complete) to 1.25 consumed life (the conservative estimate of macroscale damage). Figure 4-13 plots the percent change of the post-processed (a) stiffness and (b) CS ratio within the region of interest for all eight tests. Post-processing of the CS sensor data and stiffness measured by the load frame consisted of two steps: calibration and smoothing.

Individual calibration is required in all tests because the damage accumulation rate of the CS sensor itself within the 'pseudo steady-state' region varied significantly due to the differences in their spotweld strength. This variability was especially evident in CS sensors attached at cycle 0 which experienced large plastic deformations in the first cycle, significantly damaging the spotwelds. To calibrate the data, the CS sensor damage accumulation rate is assumed constant and determined with a linear fit of the CS ratio data between 0.2 and 0.8 life consumed. Then, the CS sensor damage accumulation rate is subtracted from the CS ratio response to produce the calibrated CS ratio response. The same method is applied to the stiffness measured by the load frame to account for the effect of the CS sensor fatigue on the measured stiffness of the host structure.

To smooth the data, a Kalman filter is applied. Kalman filters use prior measurements to estimate a system's variability and then generate the system's true state. Kalman filters are a proven robust method to decrease noise. After applying the filter to the calibrated data, the post-processing is complete.

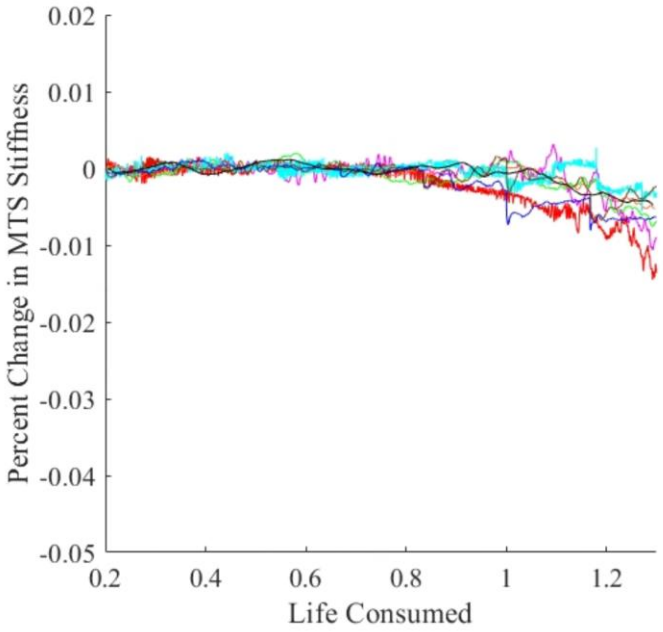

(a)

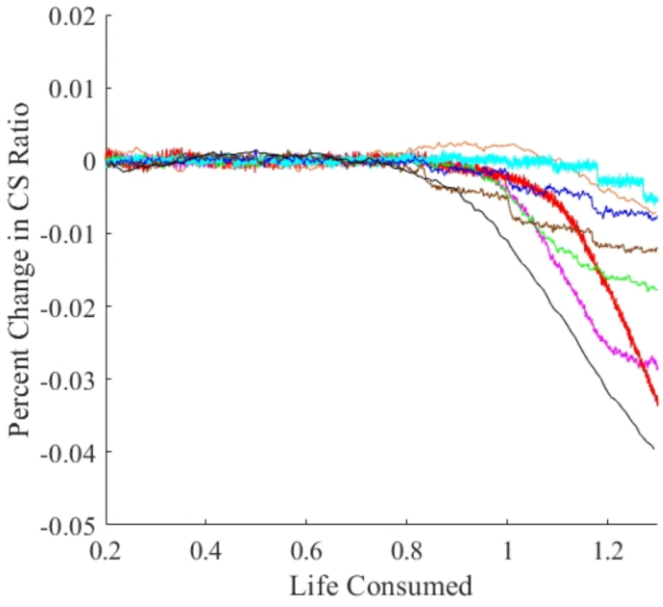

(b)

Figure 4-13. Percent change in (a) stiffness and (b) CS ratio after calibrating and smoothing the raw data.

The CS ratio shows good agreement with stiffness. When the CDO is triggered (when the life consumed is equal to unity) both the stiffness and CS ratio decrease. In tests where the CS sensor is mounted at cycle 0, the CS ratio is most sensitive and survives

throughout the test, showcasing the CS sensor's resilience; even when the CS sensor itself is accumulating damage, it can still accurately predict the onset of damage accumulation in steel. In tests where the CS sensor is mounted at cycle 1, the CS ratio is less sensitive, but still able to detect the onset of damage, showcasing the CS sensor's ability to be used retroactively to monitor the health of existing structures. However, the sensitivity of the CS sensor varies widely test-to-test, so an individualized, automated damage onset criterion should be used to determine the exact onset of damage measured by the CS sensor. To perform the automation, two machine learning algorithms are employed – anomaly detection and neural net classification.

An anomaly was specified when five consecutive post-processed data points exceeded 3 standard deviations from the original mean of the data. Both standard deviation and mean were computed from the data between 0.2 and 0.3 consumed life. The predicted time of damage onset can be seen in Table 3. The average time of damage onset predicted by the anomaly detection algorithm was 0.996 and the standard deviation was 0.113 consumed life. This is well before the conservative estimate of macroscale damage which occurs at 1.25 consumed life.

Specimen #	Damage Onset Predicted with Anomaly Detection
1	0.96
2	1.00
3	1.18
4	0.95
5	1.00
6	0.84
7	1.16
8	0.88
Average	0.996
Standard Dev	0.113

Table 3. Predicted damage onset using anomaly detection with CS ratio.

Neural net classification was used in a similar fashion to anomaly detection. The neural net input was *n* consecutive calibrated and smoothed measurements of the CS ratio at time *T*. The output from the neural net was either 'healthy' or 'faulty.' The hidden layers in the neural net include a 50 node fully connected layer, a batch normalization layer, a rectified linear unit layer, and a soft max layer, as schematically shown in Figure 4-14. A randomly selected 50% of the data from all tests was used to train the neural net and the remaining 50% of the data was used to test the neural net.

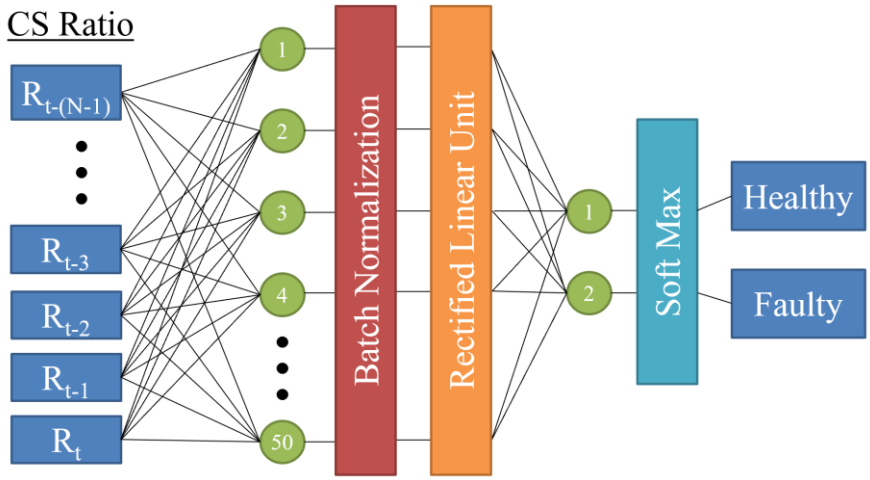

Figure 4-14. Neural net schematic for classification of CS sensor data.

The first step in finding the optimal neural net was determining the vector size, *n*, of consecutive measures of CS ratio to input which resulted in the greatest accuracy. The accuracy of the neural net as n is varied from 1 to 20 is shown in Figure 4-15. It is apparent that once *n* exceeds 3, the accuracy of the neural net saturates.

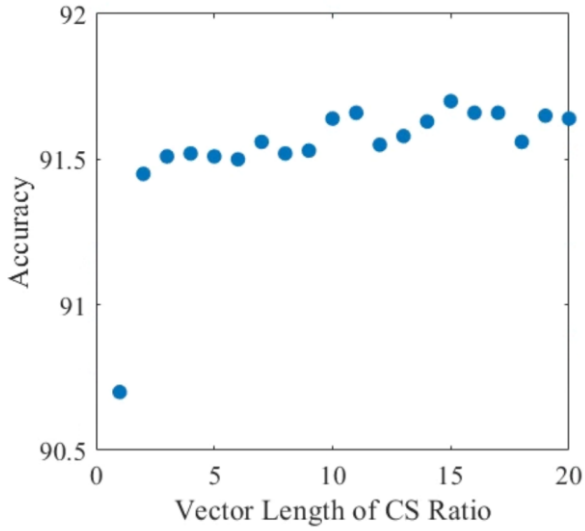

Figure 4-15. Accuracy of the neural net as N, the number of consecutive CS ratio measurements used as inputs, is varied from 1 to 50. The accuracy plateaus when N = 3.

For validation, the neural net when *n=3* was applied to each of the eight individual tests. The confusion matrix for each of the eight tests is shown in Table 4. The accuracy in all tests is greater than 83%. In five of the eight tests, the neural net has a sensitivity of 100%; this means the neural net never predicted a healthy state when the structure was truly damaged, which is desirable to ensure safety but may waste useful life of the structure.

Test 1		
	Predicted Healthy	Predicted Damaged
Truly Healthy	2065	134

Truly Damaged	0	824
Test 2		
	Predicted Healthy	Predicted Damaged
Truly Healthy	8885	194
Truly Damaged	70	3334

Test 3		
	Predicted Healthy	Predicted Damaged
Truly Healthy	8815	0
Truly Damaged	2020	1285

Test 4		
	Predicted Healthy	Predicted Damaged
Truly Healthy	674	53
Truly Damaged	0	272

Test 5		
	Predicted Healthy	Predicted Damaged
Truly Healthy	941	18
Truly Damaged	0	359

Test 6		
	Predicted Healthy	Predicted Damaged
Truly Healthy	758	201
Truly Damaged	0	359

Test 7		
	Predicted Healthy	Predicted Damaged
Truly Healthy	239	0
Truly Damaged	39	50

Test 8		
	Predicted Healthy	Predicted Damaged
Truly Healthy	81	30
Truly Damaged	0	41

Table 4. Confusion matrix of neural net applied to eight individual fatigue tests.

The time at which the neural net predicts damage onset was set to three consecutive predictions of a 'faulty' state. The time at which the neural net predicts the onset of damage for each test is shown in Table 5. The average predicted failure time from the neural net with the CS ratio as input is 0.954 and the standard deviation is 0.100. Compared to the anomaly detection algorithm, the neural net offers some improvement, namely, the predicted time of damage onset by the neural net occurs before the predicted time of damage onset by the anomaly detection algorithm. Also, the standard deviation of the predicted times of damage onset is lower with the neural net. Additionally, the neural net has the ability to easily incorporate data from other sensors, which may prove appealing in many industrial applications.

Specimen #	Damage Onset Predicted with Neural Net Classification
1	0.95
2	0.94
3	1.18
4	0.95
5	1.00
6	0.84
7	1.15
8	0.84
Average	0.954
Standard Dev	0.100

Table 5. Neural net predicted damage onset times.

To quantify the benefit of the advanced warning provided by the CS sensor, the number of loading cycles between the damage onset predicted by the CS sensor and the conservative estimate of macroscale damage is calculated via

$$N_{adv} = (t_{macro} - t_{CDO}) * N_{acc} * AF \quad \textit{Equation 26}$$

where N_{adv} is the number of loading cycles after the CS sensor detects damage needed to cause macroscale damage, t_{macro} is the conservative estimate of macroscale damage (1.25), t_{CDO} is the average consumed life when the CS sensor predicts the onset of damage, N_{acc} is the number of cycles to truly trigger the CDO, and *AF* is the acceleration factor. The acceleration factor is included because the steel used in the intended applications will experience much lower stress levels than the steel used in the accelerated lab fatigue tests. The acceleration factor is calculated via

$$AF = \frac{N_{use}}{N_{acc}} = \frac{\left(\frac{1}{332.7}\Delta\sigma_{use}\right)^{\frac{1}{-0.0154}}}{\left(\frac{1}{332.7}\Delta\sigma_{acc}\right)^{\frac{1}{-0.0154}}} = \left(\frac{\Delta\sigma_{acc}}{\Delta\sigma_{use}}\right)^{64.8} \quad \textit{Equation 27}$$

where the subscripts *use* and *acc* denote the use application and accelerated test values, respectively, and the constants from the fit in Figure 4-11 have been applied. Assuming an application stress of 80% of σ_{ult}, the acceleration factor is equal to 230.

Using Equations 26 and 27, for a use application where the external load is 80% of σ_{ult}, the damage onset detected by the CS sensor with anomaly detection occurs 60k cycles before the conservative estimate of macroscale damage. Under the same use conditions, the damage onset detected by the CS sensor with neural net classification occurs 70k cycles before the conservative estimate of macroscale damage. Evidenced by these advanced warnings, it is evident that the CS sensor, a passive, *in-situ*, small size, and computationally inexpensive sensor, is able to detect microstructural damage events which can greatly improve life-cycle sustainment logistics.

Future work pairing machine learning algorithms with the CS sensor should include more sophisticated machine learning techniques. Currently, both machine learning algorithms

offer a single data point for remaining useful cycles. However, a trending value of stiffness which updates the remaining useful cycles as damage accumulates should offer better prognostic variability.

4.3.2. Slow Loading – Resistive copper foil and fiber optic CS sensors

As stated previously, to measure the CS ratio from the fiber optic sensors, a loading cycle was completed at much lower loading rates at set intervals. The compliant and stiff strains measured by the fiber optic sensors are compared to the strains measured by the resistive copper foil gauges in Figure 4-16a and Figure 4-16b, respectively. The time scales in Figure 4-16 do not represent the time of the entire test, but just the time accumulated during the slow loading cycles.

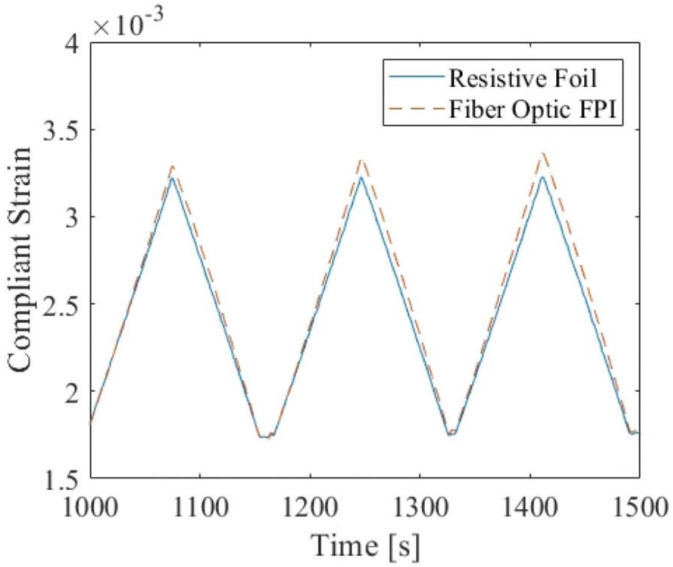

(a)

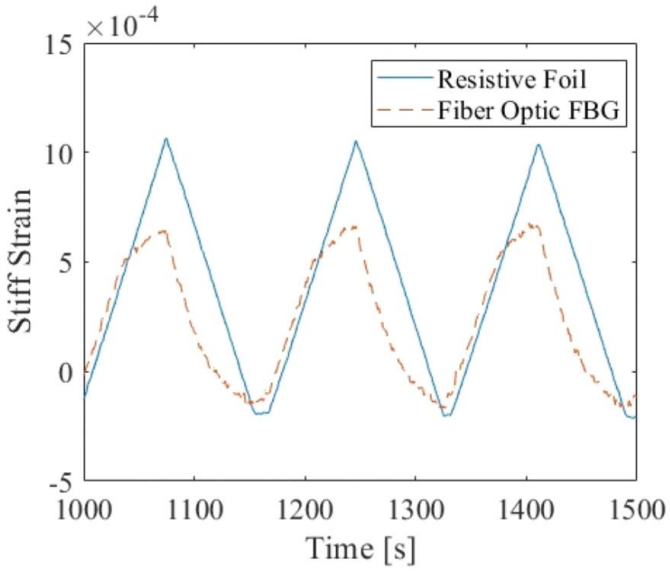

(b)

Figure 4-16. Fiber optic strain gauges compared to resistive copper foil gauges in test 3. (a) compliant sensor's FPI and (b) stiff sensor's FBG.

The resistive foil gauge and FPI (which is used as the compliant sensor) display nearly identical behavior. The resistive gauge and the FBG on the steel shim (which is used as the stiff sensor) display a notable difference. The difference is due to large shear lag in the compliant adhesive layer used to attach the stiff FBG to the stiff steel shim, In Tests 5 and 6, where the fiber optic sensors are tested at 87% of σ_{ult}, the large adhesive shear lag confounds the behavior of the stiff sensor. Therefore, only the results from Test 3, shown in Figure 4-16, will be analyzed for the fiber optic sensor.

The normalized response of the fiber optic CS ratio, resistive foil CS ratio, and stiffness for Test 3 are plotted in Figure 4-17. All measurements follow the same behavior as before, with each holding relatively constant during the 'pseudo steady-state' region and then decreasing notably when the CDO is triggered, which for Test 3 occurred at 110k cycles.

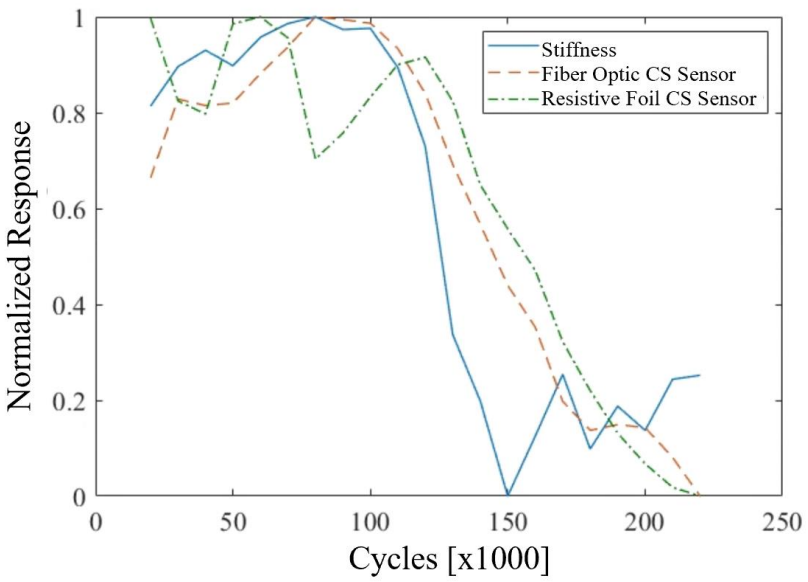

Figure 4-17. The normalized response of the fiber optic CS ratio, resistive copper foil CS ratio, and MTS stiffness as number of cycles increases.

In addition to simple stiffness tracking, the CS sensor can also provide hysteresis measurements since host stress and strain histories can be fully extracted from the stiff and compliant sensor strain histories. In the fast loading at 10Hz, the data is too sparse to reconstruct the stress-strain curve. However, in the slower loading cycles, enough data points are collected to reconstruct the stress-strain curve.

The reconstructed stress-strain curves for Test 3 are shown in Figure 4-18. The mismatch between the fiber optic CS sensor reconstructed stress-strain curve and the stress-strain curve reported by the load cell is large and is attributed to the shear lag in the stiff sensor as well as the sparse collection of data points. The resistive foil CS sensor shows better performance, with consistent stress and strain magnitudes which match those measured by the load frame, but still does not fully reflect the stress-strain curve measured by the load frame when the load reverses from extension to compression. The reconstructed

stress-strain curve from the resistive foil CS sensor shows a vertical decrease in stress and constant strain when the load reverses whereas the true stress-strain behavior reported by the load frame shows a constant stress and an increase in strain when the load reverses. The trend of the reconstructed stress-strain curve by the CS sensor is due to the left hand Reiman sum algorithm used by the CS sensor. When the tangent modulus is zero, no matter what external force is measured, the extension of the structure will always be estimated as zero. The estimation of zero strain is one limitation of the pin-force model not elucidated in earlier publications and is a focus of future work.

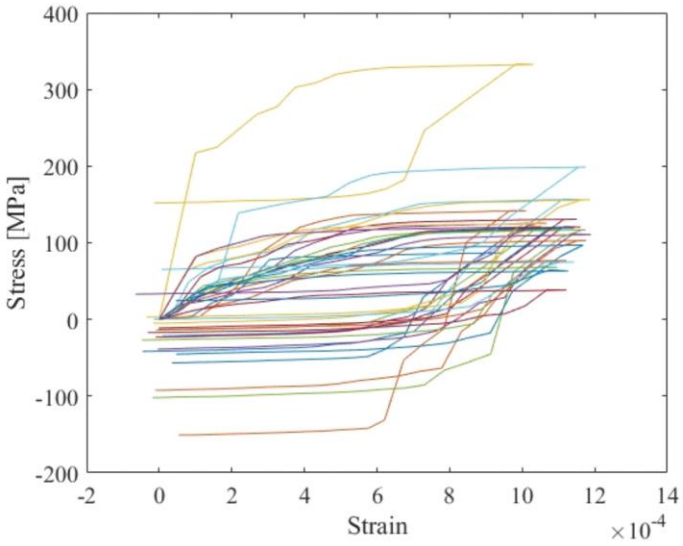

(a)

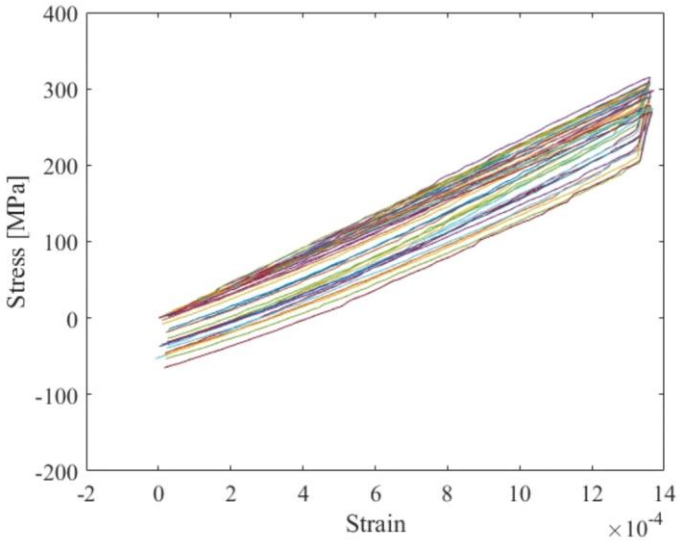

(b)

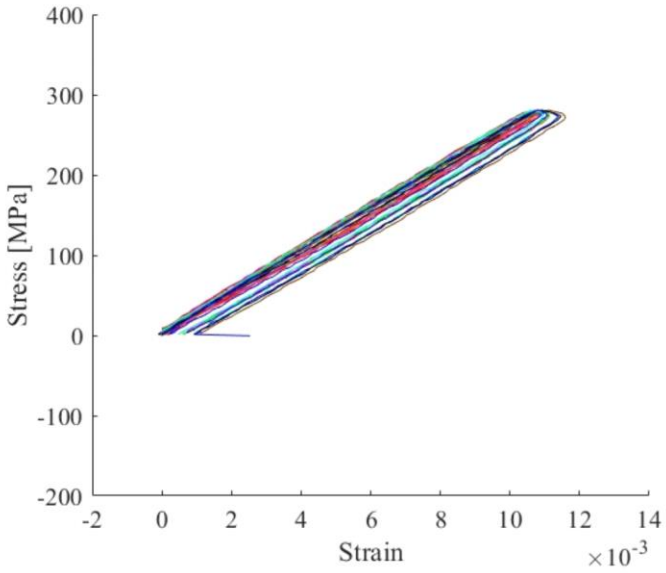

(c)

Figure 4-18. Recreated stress-strain curve from (a) fiber optic CS sensor and (b) resistive foil CS sensor. (c) the stress-strain curve as reported by the load frame.

Even considering the error when the load reverses, the recreated stress-strain curves show a softening of the modulus when the CDO is triggered and the correct general hysteresis trend. To validate the claim of accurate qualitative stress-strain reconstruction by the resistive foil CS sensor, a left-handed Riemann sum is employed to calculate the plastic work density. The plastic work density measured by the resistive foil CS sensor for Test 3

(loaded at 84% of σ_{ult}) has poor qualitative trend. This is assumed to be due to the noise from the CS sensor masking the relatively small plastic work density accumulated in each cycle.

In contrast, the plastic work density measured by the resistive foil CS sensor for Tests 5 and 6 (at 87% of σ_{ult}) have good qualitative trend. The plastic work densities within each slow loading cycle measured by both the resistive foil CS sensor and the load frame for Tests 5 and 6 are plotted in

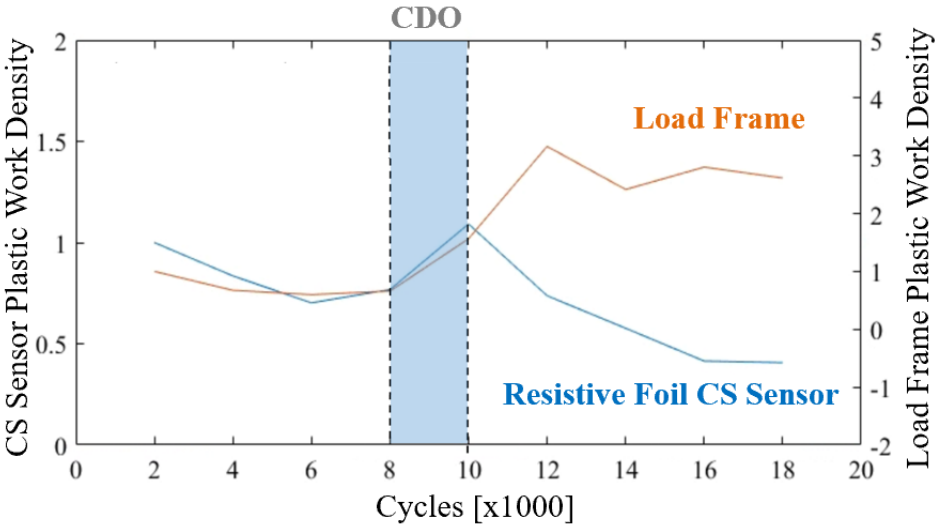

(a)

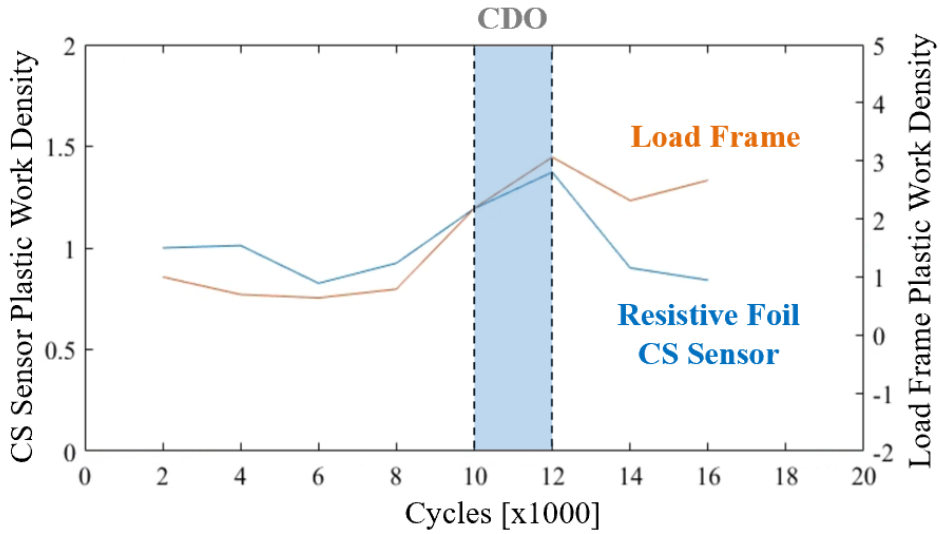

(b)

Figure 4-19. The resistive foil CS sensor mirrors the MTS behavior until the onset of damage occurs; the damage onset occurs within the blue region bounded with dashed black lines. Then as the failure site concentrates away from the CS sensor, the CS sensor shows a decrease in plastic work density whereas the plastic work density measured by the load frame plateaus. The decrease in plastic work density measured by the CS sensor is due to the local measuring footprint of the CS sensor versus the global average provided by the load frame. The good qualitative match between the CS sensor and load frame in Tests 5 and 6 show the efficacy of such an approach to track damage; however, care must be taken to reduce noise from the CS sensor as much as possible when tracking smaller damage events.

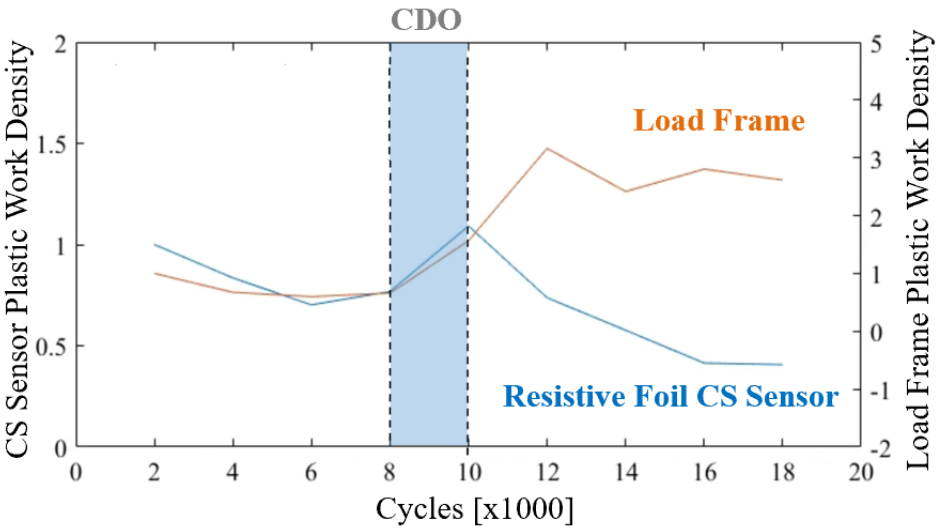

(a)

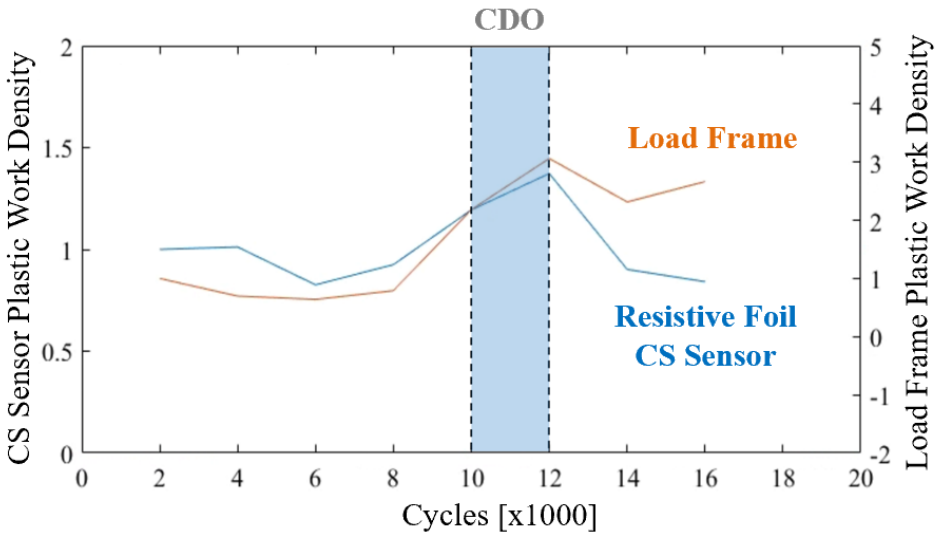

(b)

Figure 4-19. Comparison between the plastic work density estimated by the resistive foil CS sensor and load frame for (a) test 5 and (b) test 6. From the failure criterion, failure occurs at the end of the blue region, but because the slow cycle contains a large portion of damage, it can hide the actual failure time from the algorithm. So true failure occurs somewhere within the blue region.

Regarding the advanced warning provided by the CS sensor, the obtrusivity of the CS sensor needs to be discussed. When adding a steel patch to a host structure, stress concentrations are introduced which can radically decrease the life of the host structure. The stress concentration caused by the steel patch in this experiment was evaluated using finite element analysis. A 3D brick model of the structure was constructed in Abaqus and is shown in Figure 4-20. At the load levels supplied in experiment (8-8.5kN) the stress concentration causes an increase in axial stress of approximately 60 MPa. The maximum axial stress is plotted versus displacement in

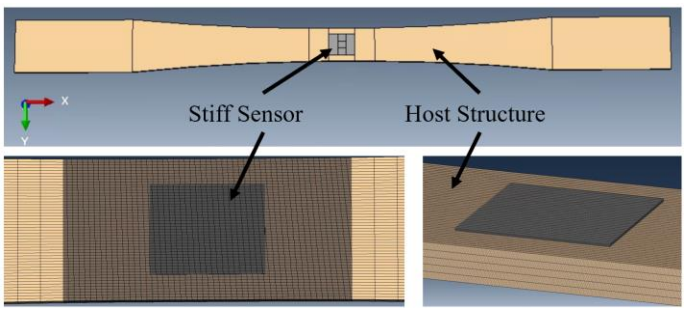

Figure 4-20. Finite element model of stee beam with CS sensor.

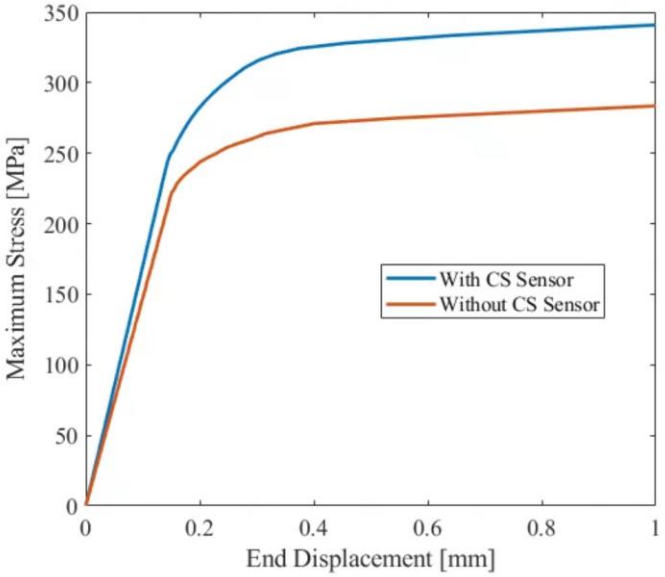

Figure 4-21. Maximum axial stress versus displacement for a steel beam with and without the CS sensor. The stress concentration caused by the CS sensor results in an increase of 60 MPa in maximum stress.

The maximum stress levels determined from the finite element analysis are used to calculate the expected fracture life of the steel beam given the S-N curve model constants found in [81]. The external load (axial force) versus the cycle at which the CS sensor detects damage is plotted in Figure 4-22. Also plotted is the external load versus expected time to fracture with and without the inclusion of the CS sensor. The damage detection from the CS sensor occurs well before the expected catastrophic failure for the steel beam; however, the inclusion of the CS sensor does cause a reduction in life of the steel.

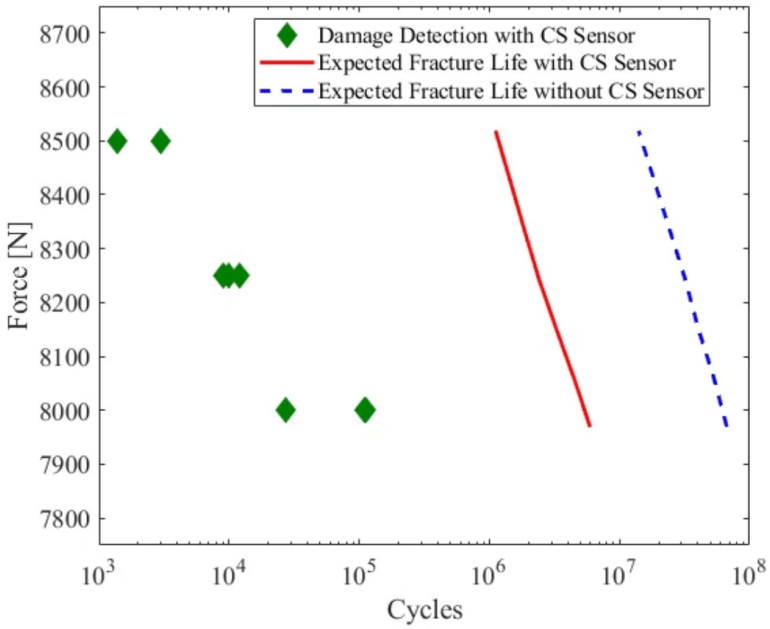

Figure 4-22. External load (force) versus cycle at which CS sensor detects damage is plotted in green diamonds. External load versus expected life with CS sensor is plotted in the solid red line. External load versus expected life without the CS sensor is plotted in dashed blue line. The inclusion of the CS sensor causes a reduction in overall life of the structure, but produces an early warning of damage detection

The trade-off between loss of life and advanced damage warning is a consistent struggle when designing damage detection sensors. Fortunately, in the case of the CS sensor, there is ample opportunity to consider this in the design phase. For example, to increase the life of the structure, the obtrusivity of CS sensor can be decreased; however, this will decrease the sensitivity of the CS sensor thus the damage warning will be generated later in life. Future work should focus on techniques like impedance matching to decrease the obtrusivity of the CS sensor while maintaining sufficient CS sensor sensitivity.

4.4. Summary of Experiments

Two surface-mounted CS sensors have been fabricated. The ‘traditional’ CS sensor consists of a resistive copper foil gauge on a steel patch as the stiff sensor and a resistive

copper foil patch on the host as the compliant sensor. The fiber optic conjugate stress sensor consists of a fiber Bragg grating sensor (FBG) on a steel pad acting as the stiff sensor and a Fabry-Perot interferometer (FPI) acting as the compliant sensor. Each CS sensor is surface-mounted on reverse sides of the host structure, a metal with modified dog bone geometry.

In monotonic tensile tests, the CS ratio (stiff sensor strain divided by compliant sensor strain) was reported and shown to have monotonic relation to tangent host modulus. The CS ratio was lowest for aluminum (75 GPa) and largest for steel (200 GPa). Also, the CS ratio was constant in the elastic regime and decreased when the host experienced plasticity. The CS ratio can act as an independent measure of host modulus and may prove useful in many PHM techniques. The pin force model was then used to convert the CS ratio to the stress-strain state of the host. In the monotonic tests of aluminum, copper, and steel, the CS sensors paired with the pin force performed well in measuring the elastic modulus of the material under test. The error in the steel measurement was larger, but that is expected as steel is in the upper limit of the CS sensor detection range. The fully reconstructed stress-strain curve of each material also showed good fit. Again, the steel stress-strain curve showed greater error, but it is expected. To monitor steel more accurately, a stiffer stiff sensor is needed in the CS sensor.

In cyclic tensile tests, the conjugate stress (CS) sensor has been used to monitor fatigue damage in cyclically loaded steel beams. The stiffnesses measured by both versions of the CS sensor during the fatigue tests mirror the stiffness reported by independent sensors

on the load frame. Using an anomaly detection method proposed in this study, the CS sensor predicts damage onset when 99.6% of the life of the steel beam has been consumed. Using a neural net to classify failure, the CS sensor predicts damage onset when 95.4% of the life of the steel beam has been consumed. 100% consumed life corresponds to the onset of damage as defined by a criterion for damage onset (CDO), which is defined when the plastic strain accumulation of the host experienced a drastic rate change indicating a plastic strain localization. At 100% consumed life, no macroscale damage is observed.

In order to quantify the advanced warning provided by the CS sensor versus macroscale damage trackers, the remaining useful life before a conservative estimate of macroscale damage occurred was converted to remaining cycles with the aid of an acceleration factor. For a use stress of 80% of σult for steel, the CS sensor provides an anomaly detection warning at least 60k cycles before macroscale damage occurs and a neural net classification warning at least 70k cycles before macroscale damage. Aided by the advanced warning provided by the CS sensor, repair logistics can be better optimized to save costs. Additionally, with the in-situ, real-time monitoring provided by the CS sensor paired with good individual prognostics, safety factors in design can be reduced saving costs as well.

The full hysteresis information of the host, in addition to stiffness, can be determined from the CS sensor. The fiber optic sensors displayed severe shear lag in the compliant adhesive layer, so the generated hysteresis plots were not useful. The resistive foil CS

sensor showed appropriate hysteresis information, accumulating large plastic strains with each cycle. The damage site eventually localized away from the CS sensor, resulting in a decrease of the plastic work density accumulation reported by the CS sensor. The hysteresis information was too noisy to predict failure on its own. However, future work will concentrate on denoising the hysteresis measured by the CS sensor, so failure predictions can be generated.

Future work must also address the stress concentration caused by the inclusion of the CS sensor in the host structure. In this work, the stress concentration is expected to result in a 32.6 million cycle reduction of life while simultaneously offering 2.6 million cycles of advanced warning.

5. Summary and Conclusions

5.1. Summary

Degradation of the mechanical stress-strain behavior of a material is a known damage precursor in many prominent failure mechanisms, i.e. overstress, fatigue, creep, and corrosion. The mechanical stress-strain behavior can be characterized by the tangent stiffness, yield strength, strain hardening parameters, strain energy density, and/or plastic work density. If accurately tracked, the advanced warning provided by changes in these parameters can greatly benefit structural and prognostic health monitoring techniques. The conjugate stress (CS) sensor has been shown to be an ideal candidate to monitor such parameters, especially the instantaneous tangent stiffness degradation because it is a passive, sensitive, small, and in-situ sensor able to determine the instantaneous stress-strain state of the host. However, there had been few published experimental results using

a CS sensor. Additionally, the modeling approaches of the sensor had varied widely; different architectures had been studied independently and all previously reported CS sensors had been developed with a specific loading condition in mind.

The Chapter 2 of this study, a finite element model (FEM) parametric evaluation of the CS sensor is provided to better understand the consequences of the design options and to develop generic guidelines on best design options for different application scenarios. The location of the individual CS sensors is parametrically varied to create guidelines for optimal implementation. Then, the performance of the CS sensor in a range of stress states is documented. Next, the CS sensor's thickness and material properties are parametrically varied to create guidelines for optimal design given the thickness and material properties of the host structure.

In Chapter 3 of this study, two analytic models of the CS sensor are developed – a pin-force model and a variational model – to supplement the detailed FEM because constructing a FEM for every application can prove time consuming and computationally expensive and therefore is not feasible for real-time post-processing of the CS sensor data. These models show much promise in correctly estimating the host modulus given the geometric properties of the structures and strains measured by the sensors. In this study, the pin force model was used for assessment of host material mechanical properties from the experimentally measured CS sensor strains because of its computational simplicity, speed, and acceptable accuracy.

In Chapter 4, the CS sensor was experimentally validated by demonstrating its capability to detect continuous reduction of tangent modulus due to plasticity and due to progressive fatigue damage. In experiments, two types of strain sensing elements are used: (i) commercial resistive copper foil strain sensors and (ii) fiber optic strain sensors, specifically Fabry-Perot interferometers and fiber Bragg Gating sensors, specially adapted for this study. Fiber optic sensors were chosen as they offer many benefits for transitioning the sensor from laboratory demonstration to real-world application.

5.2. Contributions

The existing understanding of the conjugate stress (CS) sensor design features has been enhanced through parametric analysis of surface-mounted CS sensors. The design features examined here include the locations, thickness, and moduli of the individual sensing elements in the CS sensor as well as the external stress state. Also, the experimental validation of the CS sensor was advanced through monotonic and cyclic tensile tests. Two versions of the CS sensor accurately predicted the onset of stiffness degradation due to plasticity and fatigue. Finally, two new models of the CS sensor mechanics – a closed-form analytic pin force model and a simple, rapid variational model – were developed to supplement the fully detailed FEM models of the CS sensor because constructing a FEM for every application can be computationally costly and too time-consuming to serve as an effective tool for real-time extraction of host health from streaming sensor data.

The main contributions are as follows:

1. The most comprehensive finite element parametric evaluation to date, of the surface-mounted CS sensor's sensitivity given the CS sensor architecture (location of individual sensor elements), external load state, and host thickness and modulus:
    - Sensitivity was redefined to reflect the sensing application of the CS sensor, which revealed a cap for stiff sensor stiffness.
    - Allowing coupling of the stress field of the stiff and compliant sensors demonstrated that the sensitivity is higher than was believed in prior simpler studies in the literature.
    - This should aid application guidance.
2. Two new rapid models are developed for a surface-mounted CS sensor with sensors on opposite surfaces of a host structure:
    - The analytic pin force model accurately captures the prominent deformation mechanics of the CS sensor and provides a closed form solution for host modulus given the host geometry and strains measured by the CS sensor.
    - The variational model has the potential to increase the accuracy of the pin force model without a significant increase in computation burden, but requires further work to achieve sufficiently higher accuracy at a reasonable computational cost.
    - Not only do these models decrease computational cost, they also aid in understanding the underlying physics in the CS sensor.

3. The most detailed experimental validation to date of the CS sensor using resistive copper foil and fiber optic strain sensing elements, under monotonic and cyclic tensile tests.
    - The CS sensor accurately predicted the elastic modulus of three isotropic metals – aluminum, copper, and steel.
    - The CS sensor accurately predicted the current stress-strain state of copper and steel as they experience plastic deformations.
    - The CS sensor accurately predicted progressive stiffness degradation in isotropic steel bars as a function of cyclic fatigue damage. Two machine learning approaches were used to aid in this failure detection – anomaly detection algorithms and neural net classification.
    - The resistive copper foil CS sensor estimated the cyclic degradation of the stress-strain hysteresis of the fatigued steel with limited accuracy.

5.3. Limitations of Current Work and Scope for Future Work

- The bonding method for attaching the CS sensor elements to the host structure has its own load-induced degradation, which confounds the monitoring of host health degradation. Future studies need to determine a consistent and robust bonding method of the CS sensor, in order to minimize variance between CS sensors and to enable better health predictions.
- Real-time, fast acquisition of streaming sensor output and real-time post-processing of the data to infer current host health remain a challenge. Future

work should focus on pairing a real-time, reliable data processing unit with secure data transfer with the CS sensor for real-time health monitoring.

- Further continuation of experimental validation with heterogenous materials.
- Further continuation of experimental validation with dynamic fatigue tests are important as the CS sensor may show greater sensitivity to nonlinear changes experienced in large-amplitude dynamics.
- Further continuation of experimental validation with corrosion testing; corrosion is a prominent failure mechanism in which stiffness degradation is a known damage precursor and preliminary work in this study indicates that the CS sensor concept may provide interesting capabilities for monitoring host heath in corrosion environments.
- The simplified, rapid, variational model developed in this study for CS sensor mechanics has shown early promise as a companion to the CS sensor for real-time health-monitoring but needs further work to achieve acceptable accuracy at acceptable computational cost.
- The current obtrusivity of the CS sensor is large, with the known trade-off of lower obtrusivity relating to lower sensitivity. Methods such as impedance matching or intelligently arraying the CS sensor to reduce the obtrusivity needs to be studied.

6. References

[1] M. Majeed and A. Dasgupta, "Multifunctional Dual-Stiffness Sensor for In-Situ Real-Time Stiffness and Energy Density Measures," in *AIAA Structures,*

Structural Dynamics, and Materials Conference, Denver, 2002.

[2] M. Mejeed, "MULTIFUNCTIONAL DUAL-STIFFNESS SENSOR FOR IN- SITU REAL-TIME STIFFNESS AND ENERGY-DENSITY MEASUREMENTS," 2001.

[3] K. Wakha, M. Majeed, A. Dasgupta and D. Pines, "Dual-Stiffness Sensor for Damage Detection, Localization, adn Prognostics," *AIAA Journal,* vol. 43, no. 8, pp. 1663-1674, 2005.

[4] S. Gokanakonda, M. Ghantasala and D. Kujawski, "Fatigue sensor for structural health monitoring: design, fabrication, and experimental testing of prototype sensor," *Structural Control and Health Monitoring,* vol. 23, pp. 237-251, 2011.

[5] S. Gokanakonda, "Fabrication, Testing and Analysis of a Fatigue Sensor for Strucutral Health Monitoring," Western Michigan University, Dissertation, 2014.

[6] B. H. M. P. Wijesinghe, S. A. Zacharie, K. D. Mish and J. D. Baldwin, "Design and Development of In Situ Fatigue Sensors for Structural Health Monitoring of Highway Bridges," *Journal of Bridge Engineering,* vol. 18, no. 4, pp. 297-307, 2011.

[7] Y. Xia, X. Lei, P. Wang, G. Liu and L. Sun, "Long-term performance monitoirng and assessment of concrete beam bridges using neutral axis indicator," *Structural Control and Health Monitoring,* vol. 27, 2020.

[8] M. Saleh, R. Kempers and G. Melenka, "3D Printed continous wire polymer compoistes strain sensors for structural health monitoring," *Smart Materials and Structures,* vol. 28, 2019.

[9] A. Barlian, W. Park, J. Mallon Jr, A. Rastegar and B. Pruitt, "Review: Semiconductor Piezoresistane for microsystems," in *IEEE Institute of Electrical and Electronics Engineers*, 2009.

[10] J.-R. Lee, H. Tsuda and N. Toyama, "Impact wave and damage detections using a strain-free fiber Bragg grating ultrasonic receiver," *NDT&E International,* vol. 40, pp. 85-93, 2007.

[11] H. Tsuda, J.-R. Lee and J. Takatsubo, "Investigation of fatigue crack in stainless steel using a mobile fiber Bragg grating ultrasonic sensor," *Optical fiber technology,* vol. 13, pp. 209-214, 2007.

[12] V. Giurgiutiu, Structural Health Monitoring with Piezoelectric Wafer Active Sensors, Elsevier, 2014.

[13] A. Mal, F. Ricci, H. Samajder and H. Baid, "NDE of composite strucures using ultrasonic guided waves," in *Health Monitoring of Strucutra and Biological Systems,* 2013.

[14] Y. Zou, L. Tong and G. Steven, "Vibration-Based Model-Dependent Damage (Delamination) Indentification and Health Monitoring for Composite Sructures - A Review," *Journal of Sound and VIbration,* 2000.

[15] X. Zhao, H. Gao, G. Zhang, B. Ayhan, F. Yan, C. Kwan and J. Rose, "Active health monitoring of an aircraft wing with embedded piezoelectric sensor/actuator network: 1. Defect detection, ocalization and growth monitoring," *Smart Materials and Structures,* 2007.

[16] V. Giurgiutiu, A. Zagrai and J. Bao, "Piezoelectric wafer embedded active sensors for aging aircraft strucutral health monitoring," *Structural Health Monitoring,* 2002.

[17] B. Wisner, K. Mazur, V. Perumal, K. Baxevanakis, L. An, G. Feng and A. Kontsos, "Acoustic emission signal processing framework to indentify fracture in aluminum alloys," *Engineering Fracture Mechanics,* 2018.

[18] P. Vanniamparambil, U. Guclu and A. Kontsos, "Indenification of Crack Iniation in Aluminum Alloys using Acoustic Emission," *Experimental Mechanics,* 2015.

[19] B. Wisner and A. Kontsos, "Invesitgation of particle fracture during fatigue of aluminum 2024," *International Journal of Fatigue,* 2018.

[20] D. Aggelis, E. Kordatos and T. Matikas, "Acoustic emission for fatigue damage characterization in metal plates," *Mechanics Research Communications,* 2011.

[21] Y. Tian, Y. Shen, D. Rao and W. Xu, "Metmaterial improved nonlinear ultrasomincs for faitgue damage detection," *Smart Materials and Structures,* vol. 28, 2019.

[22] J. Sirohi and I. Chopra, "Fundamental Understanding of Piezoelectric Strain Sensors," *Jounral od Intelligent Material Systems and Structures,* 2000.

[23] C. Zhu, Y. Chen, Y. Zhuang, Y. Du, R. Gerald II, Y. Tang and J. Huang, "An optical interferometric triaxial dispalcement sensor for stuructral health monitring: characterization of sliding and debonding for a delamination process," *IEEE Sensors,* 2017.

[24] G. Light, H. Kwun, S. Kim and R. Spinks, "Magnetostrictive sensor for active health monitoring in structures," in *Smart nondestructive evaluation for health monitoring of strucutral and biological systems*, 2002.

[25] E. Saidha, G. N. Naik and S. Gopalkrishnan, "An experimental investigatino of a smart laminated composite beam with a amagnetostrictive patch for health monitoring applications," *Structural Health Monitoring,* 2003.

[26] A. Coscetta, A. Minardo, L. Olivares, M. Mirabile, M. Longo, M. Damiano and L. Zeni, "Wind Turbine Blade Monitoring with Brillouin-Based Fiber-

Optic Sensors," *Hindawi,* 2017.

[27] S. Minakuchi, Y. Okabe and N. Takeda, "Barely visible impact damage detection for composite sandwich strucures by optical fiber based distributed strain measurement," *Smart Materials and Structures,* 2009.

[28] L. Wong, S. Rathnayaka, W. Chiu and J. Kodikara, "Utilising hydraulic transient excitation for fatigue crack monitoring of a cast ion pipeline using optical distributed sensing," *Structural Control and Health Monitoring,* 2018.

[29] K. Lim, L. Wong, W. K. Chiu and J. Kodikara, "Distributed fiber optic sensors for monitoring pressure and stiffness changes in out-of-round piepes," *Strucutral Control and Health Monitoring,* vol. 23, no. 2, pp. 303-314, 2015.

[30] R. Sante, "Fibre Optic Sensors for Strucutral Health Monitoring of Aircraft Composite Structures: Recent Advances and Applications," *IEEE Sensors,* 2015.

[31] Z. Shao, Q. Rong, F. Chen and X. Qiao, "High-spatial-resolution ultrasonic sensor using a micro suspened-core fiber," *Optics Express,* 2018.

[32] Z. Gong, X. Chen, Y. Yang, Z. Zhoa, H. Zou and Q. Yu, "High-sensitivity fabry-perot interferometric acoustic sensor for low frequency acoustic pressure detections," *Journal of Lightwave Technology,* vol. 35, no. 24, 2017.

[33] M. Domingues, C. Rodriguez, J. Martins, C. Tavares, C. Marques, N. Alberto, P. Andre and P. Antunes, "Cost-effective optical fiber pressure sensor based on intrinsic fabry-perot interferomtric micro-cavities," *Optical Fiber Technology,* 2018.

[34] J. Leng and A. Asundi, "Real-time cure monitoring of smart composite materials using extrinsic Fabry-Perot interferometer and fiber Bragg grating sensors," *Smart Materials and Structures,* 2002.

[35] T. Liu, M. Wu, Y. Rao, D. Jackson and G. Fernando, "A multiplexed optical fibre-based extrinsi fabry-perot sensor system for in-situ strain monitoring in composites," *Smart Materials and Structures,* 1998.

[36] R. Oliveira, C. Ramos and A. Marques, "Health Monitoring of composite strucutres by embedded FBG and interferomtric Fabry-Perot sensors," *Computer and Strucures,* 2008.

[37] D. Kim, B. Koo, C. Kim and C. Hong, "Damage detection of composite strucures using a stabilized extrinsic Fabry-Perot interferometric sensor system," *Smart Materials and Structures,* 2004.

[38] G. Zhao, S. Li, H. Hu, Y. Zhong and K. Li, "Impact localization on composite laminated using fiber Bragg grating sensors and a novel technique

based on strain amplituce," *Optical Fiber Technology,* 2018.

[39] H. Tsuda, "Ultrasound and damage detection in CFRP using fiber Bragg grating sensors," *Composites Science and Technology,* 2006.

[40] E. Kocaman, E. Akay, C. Yilmaz, H. Turkmen, I. Misirlioglu, A. Suleman and M. Yildiz, "Monitoring the Damage State of Fiber Reinforced Composites Using an FBG Network for Failure Prediction," *Materials,* 2017.

[41] C. Petrie, N. Sridharan, M. Subreamanian, A. Hehr, M. Norfolk and J. Sheridan, "Embedded metallized optical fibers for high temperature applications," *Smart Materials and Structures,* vol. 28, 2019.

[42] G. Fusiek, T. Rubert, P. Niewczas, J. McAlorum and M. Perry, "Preliminary Characterization of metal-packaged fiber Bragg gratings under fatigue loading," 2017.

[43] G. Bunger, S. Henley, C. Glass, J. Rogers, M. Webster, K. Farinholt, F. Friedersdorf, M. Pepi, A. Ghoshal and S. Datta, "Decomposition Method to Detect Fatigue Damage Precursors in Thin Components through Nonlinear Ultrasonic with Collinear Mixing Contributions," *Journal of Nondestructive Evaluation, Diagnostics, and Prognostics of Engineering Systems,* vol. 3, May 2020.

[44] E. Habtour, D. Cole, J. Riddick, V. Weiss, M. Roberson, R. Sridharan and A. Dasgupta, "Detection of fatigue damage precursor using a nonlinear vibration approach," *Structural Control and Health Monitoring,* vol. 23, pp. 1442-1463, 2016.

[45] D. Cole, E. Habtour, T. Sano, S. Fudger, S. Grendahl and A. Dasgupta, "Local Mechanical Behavior of Steel Exposed to Nonlinear Harmonic Oscillation," *Experimental Mechanics,* vol. 57, pp. 1027-1035, 2017.

[46] T. Henry, D. Cole, C. Kube, S. Fudger, R. Haynes, J.-E. Mogonye and V. Weiss, "Evaluation of Early Fatigue Signatures in Lightweight Aluminum Alloy 7075," *Experimental Mechanics,* vol. 60, pp. 205-216, 2020.

[47] A. Deshpande, Q. Jiang and A. Dasgupta, "Effect of Microscale Heterogeneities and Stress State on the Mechanical Behavior of Solder Joints," in *ITHERM,* Orlando, Florida, 2020.

[48] G. Freihofer, A. Schulzgen and S. Raghavan, "Damage mapping with a degrading elastic modulus using piezospectroscopic coatings," *NDT&E International,* vol. 75, pp. 65-71, 2015.

[49] F. L. d. Scalea, X. Zhu, M. Capriotti, A. Laing, S. Mariani and S. Sternini, "Passive Extraction of Dynamic Transfer Function from Arbitrary Ambient Excitations: Application to High-Speed Rail Inspection from Wheel-Generated Waves," *Journal of Nondestructive Evaluation, Diagnostics, and*

Prognostics of Engineering Systems, vol. 1, 2018.

[50] W. Xu, Z. Su, J. Liu, M. Cao and W. Ostachowicz, "Singular energy component for identification of initial delamination in CFRP laminates through piezoelectric actuation and non-contact measurement," *Smart Materials and Structures,* vol. 29, 2020.

[51] K. Erazo, D. Sen, S. Nagarajaiah and L. Sun, "Vibration-based structural health monitoring under changing environmental conditions using Kalman filtering," *Mechanical Systems and Signal Processing,* vol. 117, pp. 1-15, 2019.

[52] S. Lajarin, C. Nikhare and P. Marcondes, "Dependence of plastic strain and microstructure on elastic modulus reduction in advanced high-strength steels," *Journal of the Brazilian Society of Mechanical Sciences and Engineering,* vol. 40, 2018.

[53] S. Spearing, P. Beaumont and P. Smith, "Fatigue damage mechanics of composite materials part IV: prediction of post-fatigue stiffness," *Composites Science and Technology,* 1992.

[54] G. Singh, D. Kumar and P. Mohite, "Damage modelling of epoxy material under uniaxial tension based on micromechanics and experimental analysis," *Archive of Applied Mechanics,* 2015.

[55] Y. Garbatov, C. Soares, J. Parunov and J. Kodvanj, "Tensile strength assessment of corroded small scale specimens," *Corrosion Science,* 2014.

[56] S. Eldeen, Y. Garbatov and C. Soares, "Effect of corrosion degradation on ultimate strength of steel box girders," *Corrosion Engineering Science and Technology,* 2012.

[57] A. Rajabipour and R. Melchers, "A numerical study of damage caused by combined pitting corrosion and axial stress in steel pipes," *Corrosion Science,* 2013.

[58] H. Song, Z. Bai, H. Zhang, Y. Niu and S. Leen, "Effect of pre-corrosion on damage evolution and crack propagation in aluminum alloy 7050-T7651," *Fatigue and Fracture of Engineering Materials and Structures,* vol. 41, pp. 2376-2390, 2018.

[59] T. Suzuki, H. Mahfuz and M. Takanashi, "A new stiffness degradation model for fatigue life prediction of GFRPs under random loading," *International Journal of Fatigue,* vol. 119, pp. 220-228, 2019.

[60] F. Wu and W. Yao, "A fatigue damage model of composite materials," *International Journal of Fatigue,* vol. 32, pp. 134-138, 2010.

[61] S. Shiri, M. Yazdani and M. Pourgol-Mohammad, "A fatigue damage accumulation model based on stiffness degradation of composite materials,"

Materials & Design, vol. 88, pp. 1290-1295, 2015.

[62] A. El Mahi, J. Berthelot and J. Brillaud, "Siffness reduction and energy release rate of cross-ply lainates during fatigue tests," *Compostie Structures,* 1995.

[63] N. Laws and G. Dvorak, "Progressive Transverse Cracking in Composite Laminates," *Jounral of Composite Materials,* 1988.

[64] J. Yang, D. Jones, S. Yang and A. Meskini, "A stiffness degradation model for graphite/epoxy laminates," *Journal of Composite Materials,* 1990.

[65] M. Raisch, M. R. D. Genovese, N. Zaccheroni, S. B. Schmidt, M. L. Focarete, M. Sommer and C. Gualandi, "Highly Sensitive, Anisotropic, and Reversible Stress/Strain-Sensors from Mechanochromic Nanofiber Composites," *Advanced Materials,* vol. 30, no. 39, 2018.

[66] H. Han and J. Kim, "Active muscle stiffness sensor based on piezoelectric resonance for musclecontraction estimation," *Sensors and Actuators A: Physical,* vol. 194, p. 212– 219, 2013.

[67] P. Peng, A. Sezen, R. Rajamani and A. Erdman, "Novel MEMS stiffness sensor for force and elasticity measurements," *Sensors and Actuators A: physical,* 2010.

[68] S. Najarian, J. Dargahi and X. Zheng, "A novel method in measuring the stiffness of sensed objects with applications for biomedical robotic systems," *THe international journal of medical robotics and computer assisted surgery,* 2006.

[69] S. Moromugi, Y. Koujina, S. Ariki, A. Okamoto, T. Tanaka, M. Feng and T. Ishimatsu, "Muscle stiffness sensor to control an assistance deivce for the disabled," *Artificial Life Robotics,* 2004.

[70] N. Bandari, R. Ahmadi, A. Hooshiar, J. Dargahi and M. Packirisamy, "Hybrid piezoresistive-optical tactile sensor for simultaneous measurement of tissure sitffness and detection of tissue in robot-assited minimally invasie surgery," *Journal of Biomedical Optics,* 2017.

[71] R. Sanderson, A. Curatolo, P. Wijesinghe, L. Chin and B. F. Kennedy, "Finger-mounted quantitative micro-elastography," *Biomedical Optics Express,* vol. 10, no. 4, pp. 1760-1773, 2019.

[72] J. Eshleby, "The determination of teh elastic field of an ellipsoidal inclusion and related problems," 1957.

[73] P. Withers, W. Stobbs and O. Pederson, "The application of teh Eshelby method of internal stress determination to short fibre metal matrix composites," *Acta Metallurgica,* 1989.

[74] J. Kordell, A. Dasgupta and M. Yu, "A Fiber Optic Conjugate Stress Sesnor

for Instantaneous Tangnent Modulus Detection Targeting PHM Applications," *Smart Materials and Structures,* 2021.

[75] J. Kordell, M. Yu and A. Dasgupta, "A Fiber Optic Conjugate-Stress Sensor for Prognostic Health Management of Fatigue," in *SMASIS*, Irvine, CA, 2020.

[76] F. e. al., "Three-dimensional mechanical metamaterial with a twist," *Science,* 2017.

[77] H. Bae, D. Yun, H. Liu, D. Olson and M. Yu, "Hybrid Miniature Fabry-Perot Sensor with Dual Optical Caviites for Simultaneous Pressure and Temperature Measurements," *Journal of Lightwave Technology,* vol. 32, no. 8, 2014.

[78] Post, Han and Ifju, *High Sensitivity Moire,* 1994.

[79] W. Kit, K. Hyuntae, W. An, K. Kenneth, D. James and Y. Maio, "High-speed interrogation of multiplexed fiber Bragg grating sensors for monitoring dynamic strain responses during a flexible plate impact on a water surface," *Smart Materials and Structures,* vol. 29, 2020.

[80] F. Vucko, C. Bosch and D. Delafosse, "Effects of Cyclic Plastic Strain on Hydrogen Environment Assisted Cracking in High-Strength Steel," Ecole Nationale Supérieure des Mines, 2012.

[81] H. A. El Maraghy and J. N. Siddall, "Finite Fatigue Life Distribution of SAE 1008 Subjected to Various Load-Time Histories," *Journal of Engineering Materials and Technology,* vol. 102, 1980.

[82] M. Mjeed and A. Dasgupta, "Multifunctional Dual-Stiffness Sensor for In-Situ Real-Time Stiffness and Energy-Density Measurements," in *Structures, Structural Dynamics, and Materials Conference*, Denver, Colorado, 2002.

[83] Y. Garbatov, C. Soares, J. Parunov and J. Kodvanj, "Tensile strength assessment of corroded small scale specimen," *Corrosion Science,* vol. 85, pp. 296-303, 2014.